

Fig. 2.1: The NPUAP staging guideline illustrations of the various stages / severities of pressure ulcers. © National Pressure Ulcer Advisory Panel, used with permission.

tendon or muscle are not exposed. Slough may be present but does not obscure the depth of tissue loss. *May* include undermining and tunnelling.

Stage IV

Full thickness tissue loss with exposed bone, tendon or muscle. Slough or eschar may be present on some parts of the wound bed. Often include

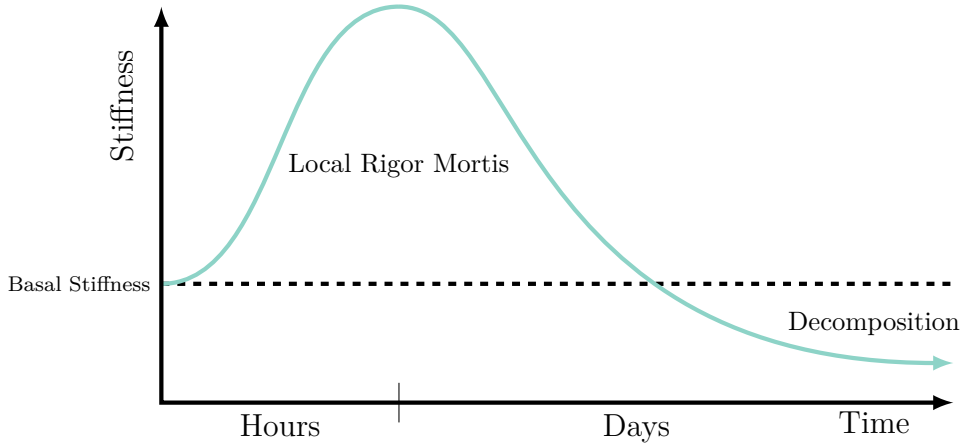


Fig. 2.2: Schematic representation of the time course of tissue stiffness changes in a deep tissue injury site. The estimate for the time-course for local rigor mortis was obtained from animal model studies [60] and the estimate for the time-course for tissue decomposition was obtained from the forensic literature [59]. (Adapted from Gefen 2009 [17], used with permission.)

the years, each relating to different mechanisms, though all relating to mechanical stress of the tissue, either through vessel occlusion or direct cellular strain. The truth is most likely a combination of these effects, with cell deformation dominating the damage on shorter time scales with increased applied pressure and vessel occlusion type injuries dominating on longer time scales [4]. In order to further investigate the etiology of PU and DTI, a combination of experimental and numerical studies has been suggested to provide better fundamental knowledge besides existing clinical experience [8]. There is also significant evidence in the literature that suggests that the current NPUAP definitions of PU and DTI are insufficient and not based on scientific evidence and that updating the clinical definitions to better reflect what exists in the literature is crucial to increasing the success of diagnosis and treatment of PU and DTI [17], [29].

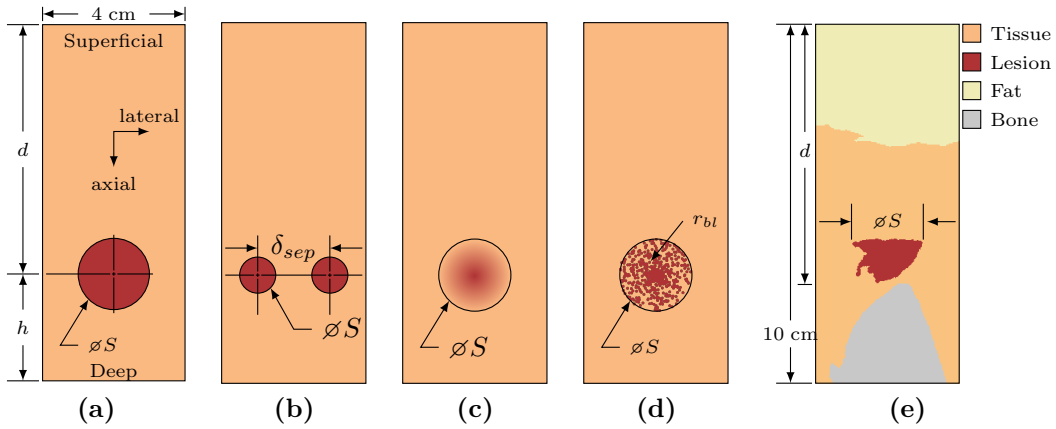


Fig. 3.1: Model geometry showing the investigated lesions embedded in a 4 cm wide soft tissue domain. Axial and lateral directions mimic that of a typical ultrasound transducer placed along the top boundary of the domain. The simplest case of a circular lesion embedded in a soft tissue domain located superior to hard underlying bone is shown in (a). In order to investigate the interference caused by closely-located lesions, the case shown in (b) was investigated. Because of the relatively unknown and variable geometric properties of deep tissue injury lesions, cases (c) and (d) were investigated where the lesion edges were blurred and the lesion was actually a large collection of small lesions, respectively. Finally, to investigate detection sensitivity in a realistic setting, case (e) was investigated where an MRI-acquired deep tissue injury was overlaid on a slice from the Visible Human Project such that the injury lesion was located immediately superior to an ischial tuberosity.

Simulated ultrasound images were acquired through the convolution of a point spread function with a normally distributed background map of scattering centres [127]. These images were then combined with a finite-element deformation model of the strained tissue to generate both pre- and post- compression images of the lesions and surrounding tissue. These images were fed into a tissue strain estimation algorithm to determine the detection sensitivity of the technique. Finally, the technique was validated against a physical phantom model using a subset of the simulated cases.

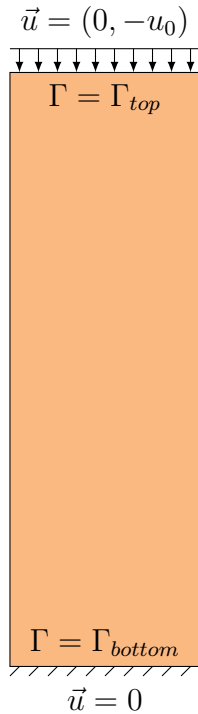


Fig. 3.3: Boundary conditions used in the finite-element calculations of soft tissue deformation.

estimations for the full range of parameter values of the simulated lesions. The algorithm consists of sweeping the image domain with a series of overlapping regions of interest (ROI). ROI are compared between pre- and post-compression images, with ROI in the post- compression images being axially scaled and translated and laterally translated versions of the same ROI in the pre-compression images.

Qualitatively, the noise and computation time of the resulting elastograms were found to be minimum when using an axial ROI size of approximately 10 times the ultrasound wavelength. Axial ROI overlap was held at 99 % to produce elastograms with minimal noise, even though this introduced significant increases in computation time. Due to the extreme anisotropic nature of ultrasound signals, lateral ROI size was kept to 5 signal widths with lateral

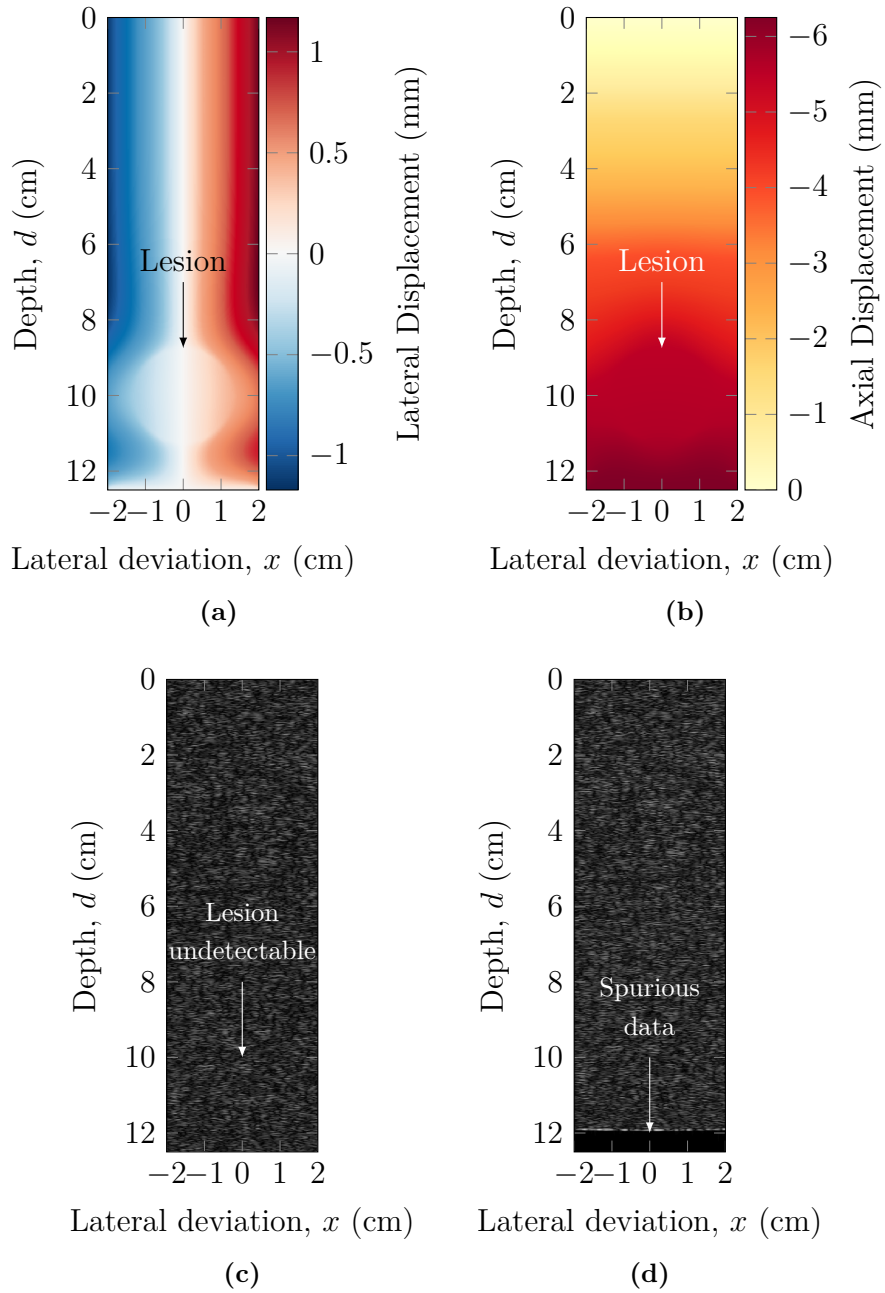


Fig. 3.4: Finite-element model results for the case when $d = 10\text{ cm}$, $\phi S = 2.5\text{ cm}$, $\varepsilon_{rel} = 3.20$, and $f = 4\text{ MHz}$ showing (a) the lateral displacement field and (b) the axial displacement field induced by compressive strain applied to the top of the boundary, (c) a generated b-mode image of the pre-compressed tissue domain, and (d) a generated b-mode image of the post-compressed tissue domain. The included lesion is not visible in (c) and (d) as its acoustic properties were no different than surrounding tissues. An anechoic region is visible along the bottom of the domain in (d) which represents tissue outside of the domain visible in (c).

boney prominences, this is unlikely to be the case. It is hypothesized that this variable strain field may be due to the large deformations present along the superior surface of the domain.

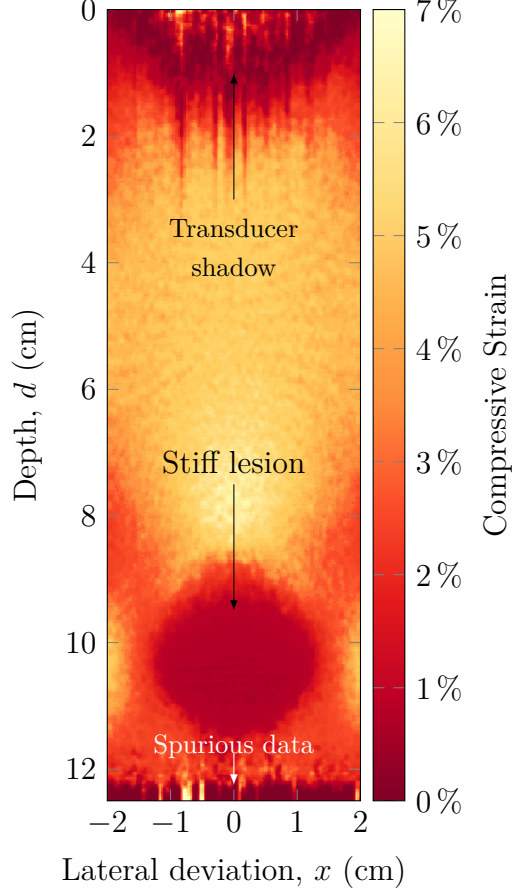


Fig. 3.5: Sample strain elastogram showing estimated strain values for $d = 10$ cm, $\phi S = 2.5$ cm, $\varepsilon_{rel} = 3.20$, $f = 4$ MHz. While undetectable on a single b-mode image, the elastogram clearly shows a low-strain (stiff) lesion located approximately 10 cm from the surface.

3.3.3 Numerical Characterizations

In order to determine the sensitivity of using quasi-static ultrasound elastography to detect deep tissue injuries, elastograms such as the example that was calculated in Section 3.3.2 were calculated for the full range of parameters

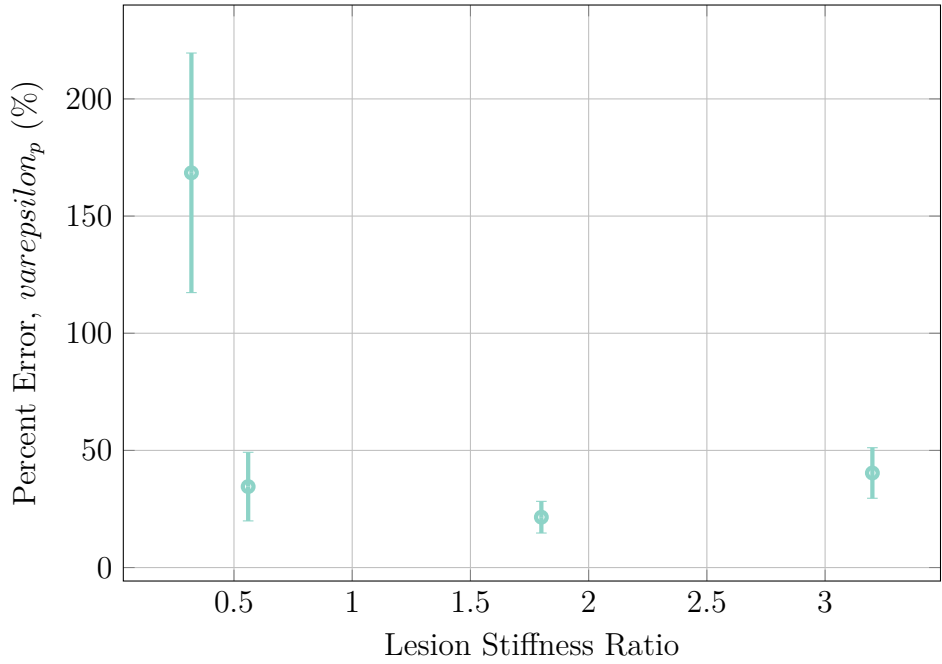


Fig. 3.6: Detection ability as it is related to true lesion stiffness ratio. For all but small lesion stiffness ratios (very unstiff lesions), results are linear and predictable. For small lesion stiffness ratios (0.32), the lesion becomes severely misrepresented. This is likely due to the algorithm “losing track” of scattering centres for the relatively large displacements induced in the significantly less stiff tissue.

$$\varepsilon_p = \left| \frac{Y_i - \hat{Y}_i}{\hat{Y}_i} \right| \times 100 \% \quad (3.6)$$

In order to broadly investigate the critical parameter-values of the investigated models, each parameter was normalized to its investigated range and the error resulting over these ranges is given in Figs. 3.7 and 3.8.

In Fig. 3.7, it is clear to see that the most sensitive error-inducing situations occur when either the lesion is very small or if large strains are used to deform the tissue. Similarly, it is expected that if the lesion depth were increased much further, significant errors would arise with increasing depth. Logically, this may be explained due to the decreasing magnitude of displacement with increasing depth—at a certain point, the magnitude of displacement

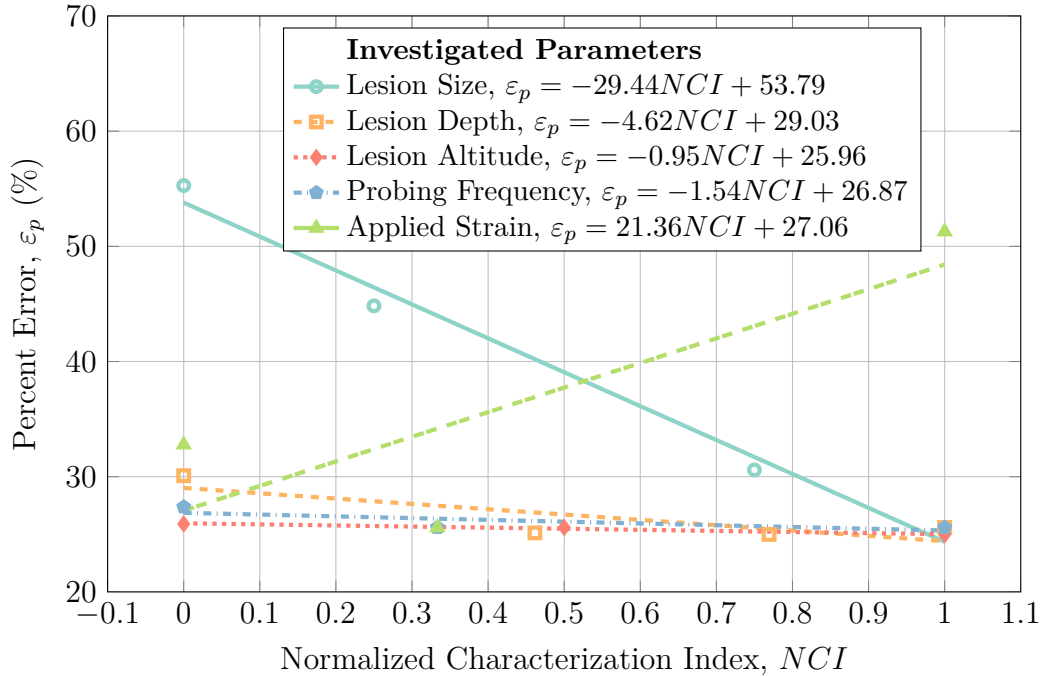


Fig. 3.7: Error characterization for range of studied parameters for the simple model of a spherical lesion embedded within soft tissue as seen in Fig. 3.1a. Each parameter has been normalized to the range studied so overly-sensitive regions may be readily distinguished. Lines represent linear regressions of the data points.

of scattering centres will be on par with the measurement noise, and the lesion will cease to be detectable.

From Fig. 3.8 it can be seen that small lesions in the Visible Human-MRI model as well as co-located lesions with large separation distances produce greater measurement errors. Conversely, lesion depth in the Visible Human-MRI model; lesion density and individual lesion size in the clustered lesion model; and boundary blur radius in the blurred-edges model do not seem to affect the measurement error significantly. Of note is the relatively large amount of static error present in the boundary blur radius model which is hypothesized to be due to lesser mean tissue stiffness in the investigated region than expected.

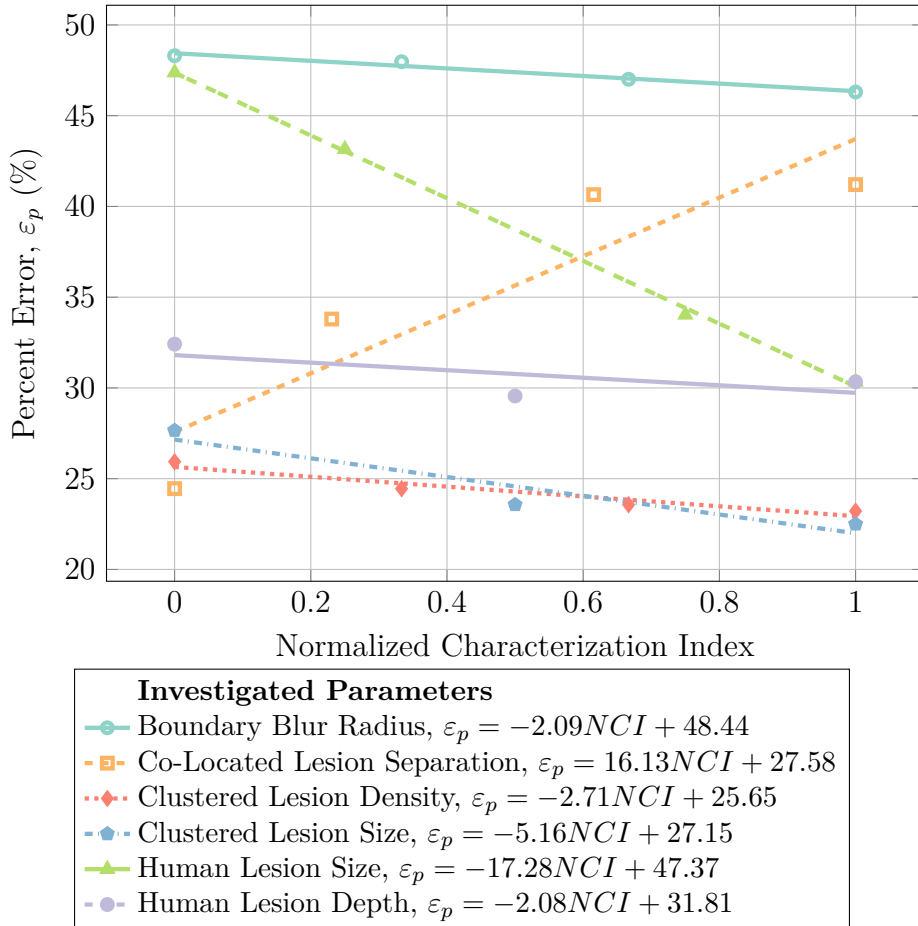


Fig. 3.8: Error characterization for range of studied parameters for the co-located lesions, blurred boundary lesions, clustered lesions, and visible human lesion models as seen in Figs. 3.1b – 3.1e. Each parameter has been normalized to the range studied so overly-sensitive regions may be readily distinguished. Lines represent linear regressions of the data.

Fig. 3.9 shows the relationship between lesion size and detection sensitivity for lesions at a depth of 10 cm in a model depth of 12.5 cm interrogated at 4 MHz with 5 % applied strain. Specifically, Fig. 3.9 shows the decreasing detection sensitivity with decreasing lesion size with the best detection sensitivity being with the largest investigated lesions with a diameter of 2.5 cm. On the opposite end, the detection sensitivity of lesions at or below 0.5 cm in diameter is questionable. Although data is lacking on the true size of forma-

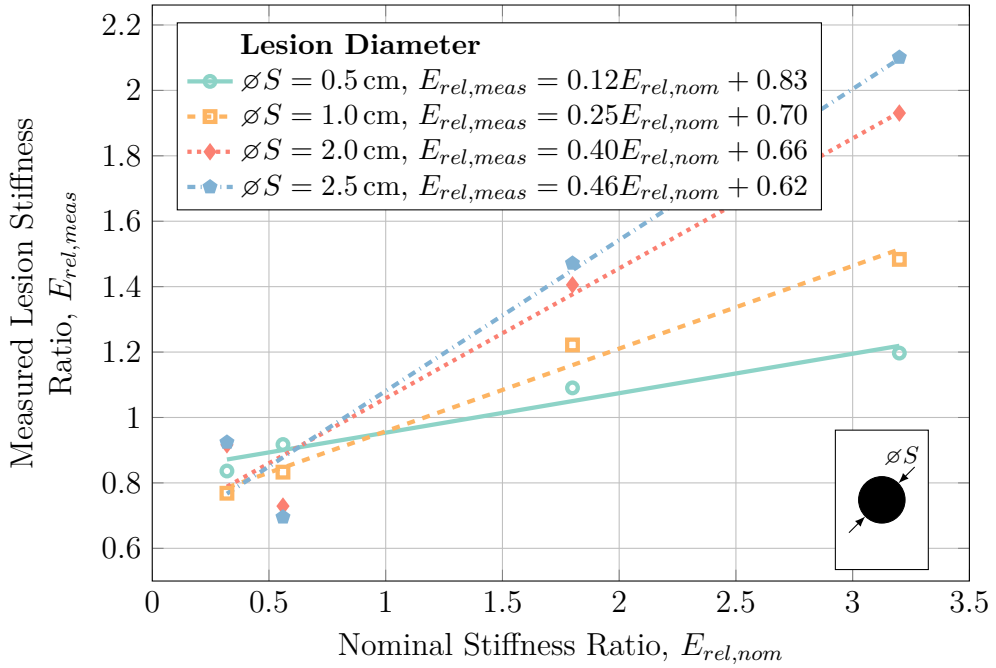


Fig. 3.9: Lesion size characterization at a depth of 10 cm with a 4 MHz ultrasound probing frequency showing increasing detection sensitivity of the lesion with increasing lesion size. Detection sensitivity is less than ideal for all cases, with the best case being for lesions approximately 2.5 cm in diameter. Lines represent linear regressions to the data.

tive DTI, MRI results indicate that untreated DTI are on the scale of multiple centimetres [67]. Thus, the ability to detect lesions of at least 1 cm in diameter should prove to be adequate to both detect and monitor DTI.

In order to investigate the effect of lesion depth on the detection sensitivity, measured strain ratios for circular lesions with a diameter of 2.5 cm located at various depths were interrogated with a 4 MHz probing frequency, and strained by 5 %. The results of this investigation are seen in Fig. 3.10.

In Fig. 3.10, it can be seen that there was little interplay between detection sensitivity and measured strain ratios at the various depths examined for all but the case of very unstiff (unstiff) lesions (with a stiffness ratio of 0.32). At such low stiffness ratios, the excessive tissue deformation interrupts the

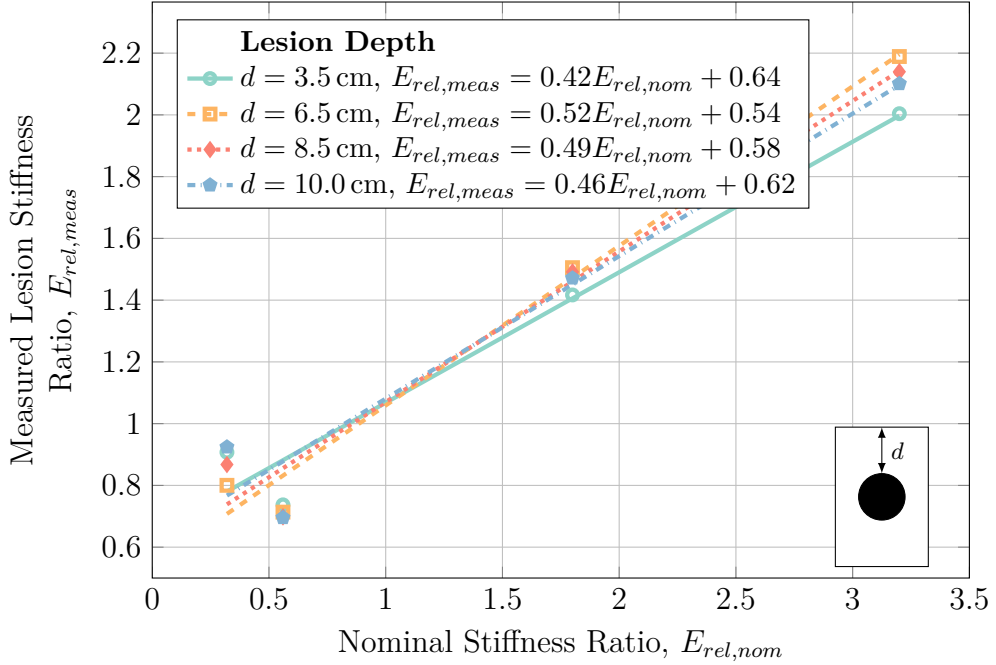


Fig. 3.10: Lesion depth characterization at a lesion diameter of 2.5 cm with a 4 MHz ultrasound probing frequency generally showing general independence of detection sensitivity on lesion depth in the tissue. Lines represent linear regressions of the data.

tissue strain estimation algorithm's ability to adequately track the induced displacements in the lesion.

Since the strain field caused by compressive forces near an extremely rigid structure embedded within a relatively unstiff domain will be significantly heterogeneous, the effect of lesion altitude above the underlying stiff bone was examined with the hypothesis that if the lesion were too close to the hard bone, it would be masked by the strain field caused by the bone's existence. A 2.5 cm diameter lesion was interrogated with a 4 MHz probing frequency and 5 % applied strain. The results of this characterization are given in Fig. 3.11.

In Fig. 3.11, it can be seen that the lesion altitude above the underlying bone had very little effect on the detection sensitivity. Although larger strain fields may be generated near the bone, it is hypothesized that the larger fields

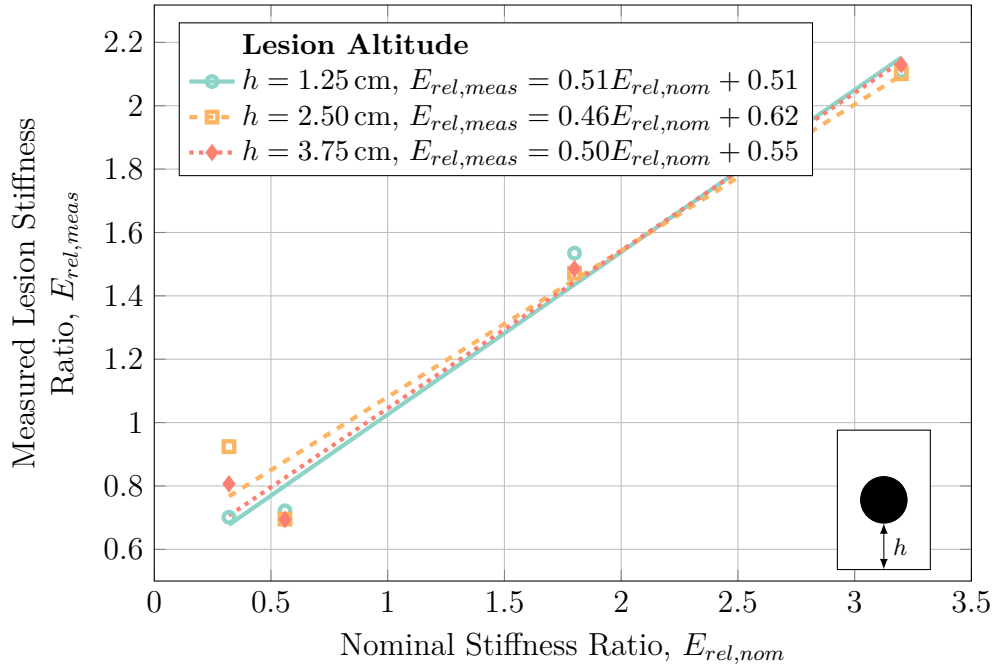


Fig. 3.11: Effect of lesion altitude above the underlying bone. Aside from erroneous results at very low lesion stiffness ratios, the effect is negligible. Lines represent linear regressions of the data.

also extend larger and so affect healthy tissue to more or less the same degree as the forming lesion.

In order to characterize the effect of using alternate ultrasound probing frequencies, simulations were carried out on lesions using probing frequencies of 2 MHz, 4 MHz, and 8 MHz. The simulated lesions had a diameter of 2.5 cm, were located at a depth of 10 cm and were strained at 5 %. The results of this study are given in Fig. 3.12.

As can be seen from Fig. 3.12, there is very little effect on the detection sensitivity from the ultrasound probing frequency that was used, therefore an appropriate frequency should be chosen so as to reach the full depth of the bone-muscle interface at suspected DTI locations while retaining the best image resolution.

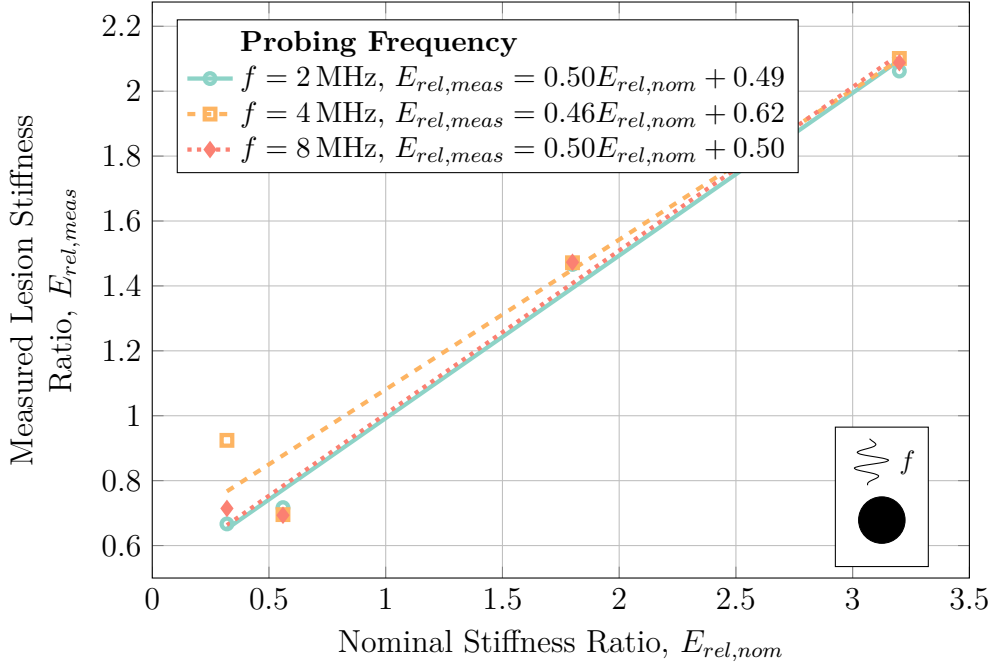


Fig. 3.12: Characterization of ultrasonic probing frequency on detection sensitivity. Apart from the requirement of using an ultrasonic frequency low enough to interrogate the desired tissue, probing frequency has negligible effect on the detection sensitivity. Lines represent linear regressions of the data.

As quasi-static ultrasound elastography is most likely to be performed via manual indentation where the exact magnitude of applied deformation is unknown, it is important to study the effect of applied strain magnitude on the detection sensitivity. Applied strains of 2.5 %, 5.0 %, and 10 % were investigated on a 2.5 cm diameter lesion at a depth of 10 cm using a probing frequency of 4 MHz; the results are given in Fig. 3.13.

While Fig. 3.13 shows a relatively constant detection sensitivity for compressive strains of 2.5 % and 5 %, compressive strains of 10 % generate significant measurement error for both very unstiff and very stiff lesions. Under large compressive strains, the tissue (either in the lesion as in the unstiff lesion case, or the surrounding tissue as in the stiff lesion case) deforms considerably which again interferes with the algorithm's ability to properly track the dis-

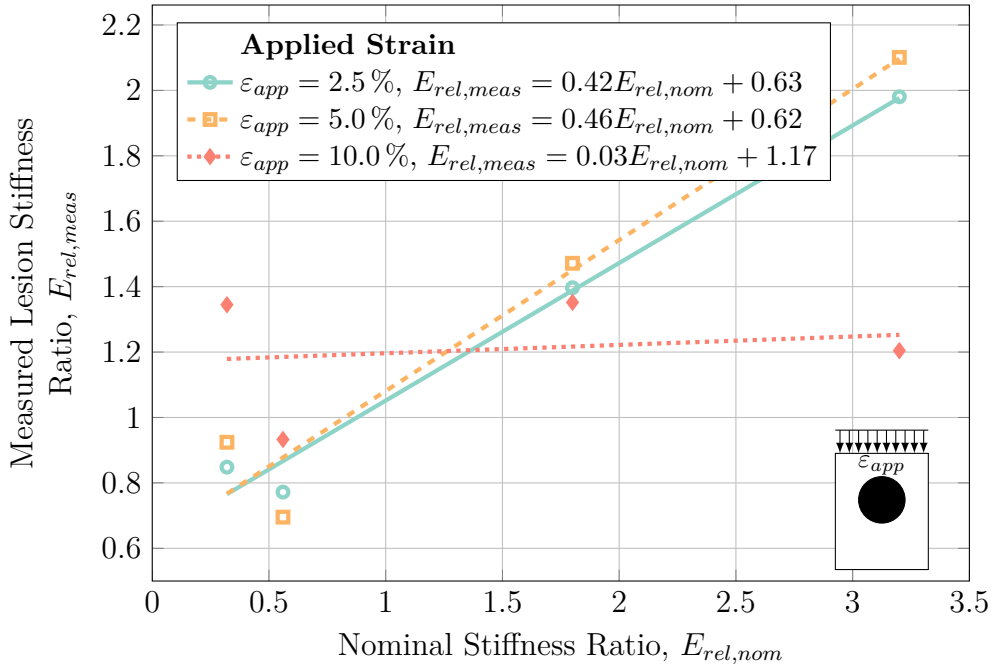


Fig. 3.13: Applied strain characterization plot for lesions with a diameter of 2.5 cm located at a depth of 10 cm interrogated at 4 MHz. There is little difference between 2.5 % and 5.0 % applied strain, while large-magnitude strains of 10 % generate significant error for both very unstiff and very stiff lesions. Lines represent linear regressions of the data.

placement of tissue. It should also be noted that applying overly large strains to an already forming deep tissue injury may cause additional unwarranted damage. Thus it is imperative that applied surface indentation be kept to reasonable bounds (2.5 % – 5 %, or 0.25 cm – 0.50 cm in 10 cm deep domains), not only for safety of the tissue but also for clarity of the diagnostic test.

To study the effect that closely spaced lesions will have on the detection sensitivity as well as how discernible the lesions will be from each other, the separation distance between two 1.0 cm diameter co-located lesions at a depth of 10 cm was examined using a 4 MHz probing frequency with 5 % applied strain magnitude. The results of this study are shown in 3.14.

While Fig. 3.14 shows that the separation distance between co-located

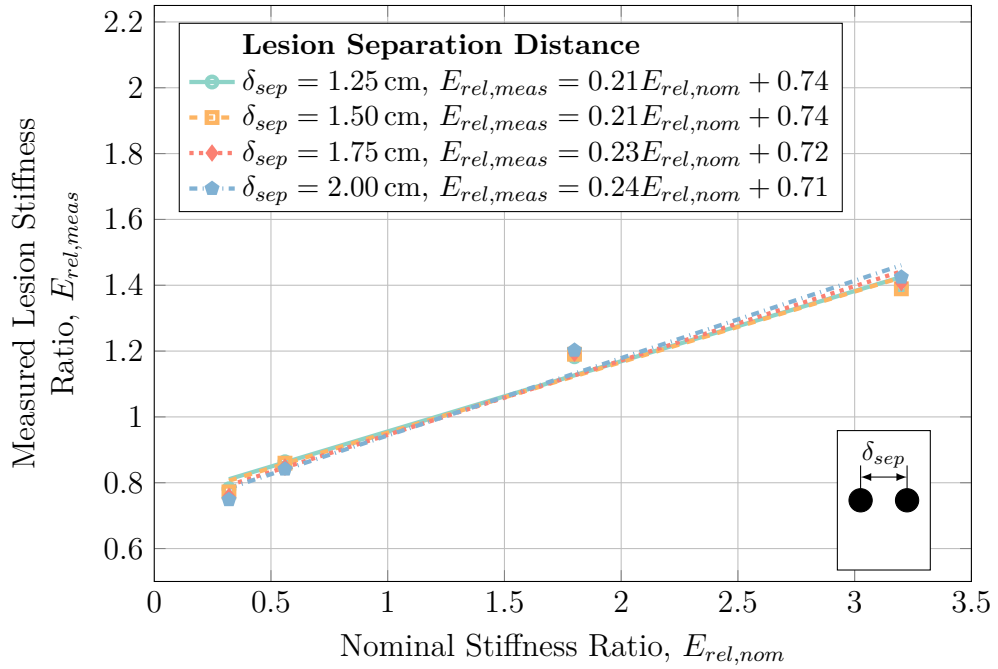


Fig. 3.14: Effect of lesion separation distance on two 1.0 cm diameter lesions co-located at a depth of 10 cm interrogated with a 4 MHz probe with 5 % applied strain. There is no negligible difference between separation distances on the detection sensitivity. Lines represent linear regressions of the data.

lesions causes a negligible effect on the detection sensitivity, Fig. 3.15 shows regions of decreased strain above and below the centreline of the lesions. While these regions had the same basal stiffness as the bulk tissue, the decreased strain pattern may obfuscate the true results by introducing “phantom lesions” which are not actually present but merely the result of the existing lesions.

While the simulations performed thus far assumed that lesions were perfect spheres with hard boundaries in order to isolate specific parameters of interest, this assumption may not always be accurate. Rather, due to the nature of injury formation, lesions may form gradual boundaries that “fade” from stiff or necrotic tissue to healthy tissue. To investigate the effect of this phenomenon on the detection sensitivity, lesions with “blurred boundaries” were investigated. Hard spherical lesions were blurred by convolving the lesion domain

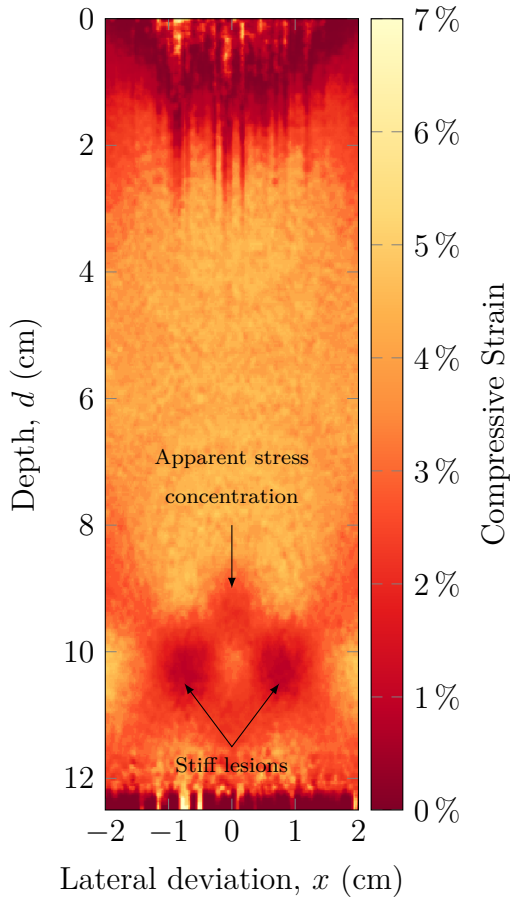


Fig. 3.15: Elastogram for two co-located lesions of 1.0 cm diameter at a depth of 10 cm interrogated using a 4 MHz probing frequency with 5 % applied strain. A pattern of decreased strain is present above and below the centerline between the two lesions themselves while the lesions themselves are not affected by each other.

with a disc blurring kernel of varying radius. The results for this investigation on lesions with a diameter of 2.5 cm, at a depth of 10 cm and interrogated with a 4 MHz probing frequency with 5 % applied strain are given in Fig. 3.16.

Fig. 3.16 shows that there is relatively little dependence of the lesion detection sensitivity on the lesion blur radius. No matter the blur radius, quasi-static elastography substantially overestimated the stiffness of stiff lesions and underestimated the stiffness of unstiff lesions. This technique was unable to discern differences in lesion stiffness due to blur radius for the least

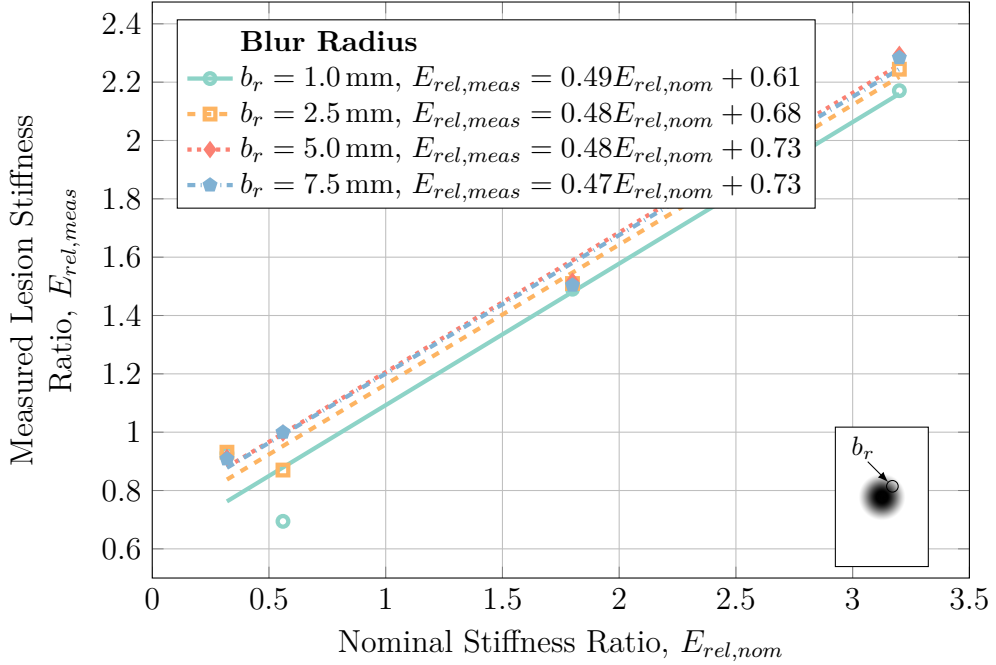


Fig. 3.16: Characterization of the effect of lesion blur radius on lesion detection sensitivity for a 2.5 cm diameter lesion at a depth of 10 cm using a probing frequency of 4 MHz and applied strain of 5 %. While there is negligible effect of the blur radius on stiff lesions, the strain ratio for unstiff lesions is considerably over-estimated. Lines represent linear regressions of the data.

stiff lesions—lesions with a nominal stiffness ratio of 0.32. Further, quasi-static elastography was generally unable to detect unstiff lesions ($E_{rel,nom} \leq 1$) whatsoever.

Similar to how lesions may have “blurred boundaries” rather than hard ones, so too may lesion composition not be homogeneous. In order to study the effect of heterogeneous regions of injured tissue, the detection sensitivity of a set of numerous small lesions located within close proximity to each other so as to form a large, heterogeneous area of diseased tissue was examined. Fig. 3.17 shows the results for this model for varying numbers of 2 mm diameter lesions in a 2.5 cm diameter circle located at a depth of 10 cm with a probing frequency of 4 MHz and 5 % applied strain. Fig. 3.19 further explores this

model by investigating the case where there are 30 small lesions per square cm with individual lesions ranging in diameter from 0.5 mm to 1.5 mm.

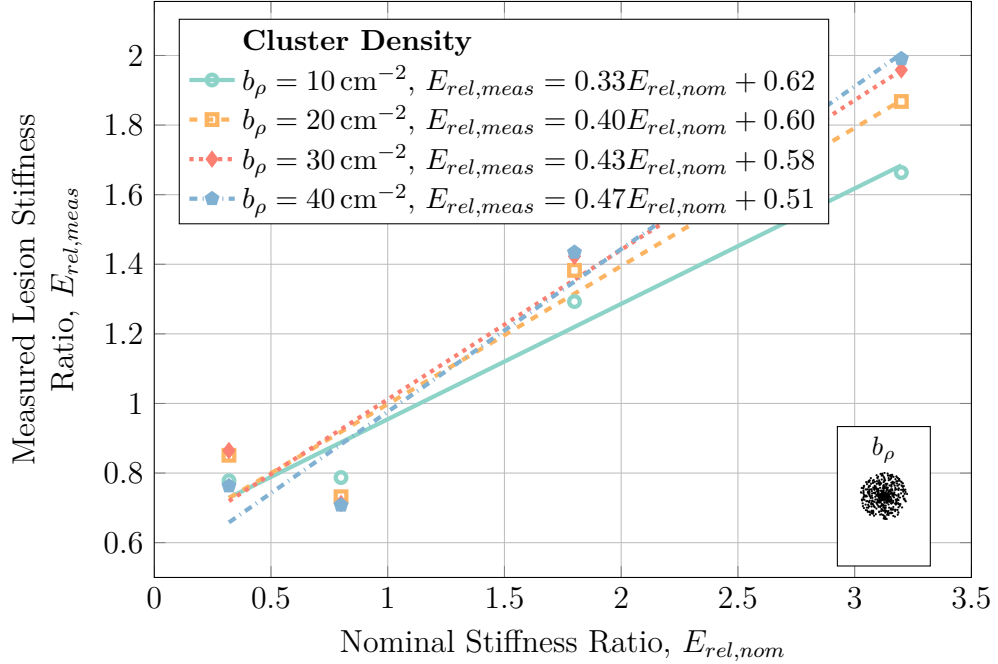


Fig. 3.17: Characterization of lesion density for a group of numerous smaller 2 mm diameter lesions comprising a large area with a diameter of 2.5 cm at a depth of 10 cm interrogated with a 4 MHz probing frequency and 5 % applied strain. Detection sensitivity decreases with decreasing lesion density, as expected. Lines represent linear regressions of the data.

The characterization plot in Fig. 3.17 for small lesion density is less linear than previous characterization plots, with lesion density having a significant effect on the detection sensitivity. Specifically, for low lesion densities, the detection sensitivity is much lower than for high lesion densities. However, this observation is warranted after examination of the elastogram produced from these results, given in Fig. 3.18, which shows how the small lesions are not individually detected but rather the entire region is detected as one large lesion. Since the average stiffness ratio over this region is less than the stiffness ratio of individual lesions, it makes sense that the “measured” strain ratio will

be less than expected.

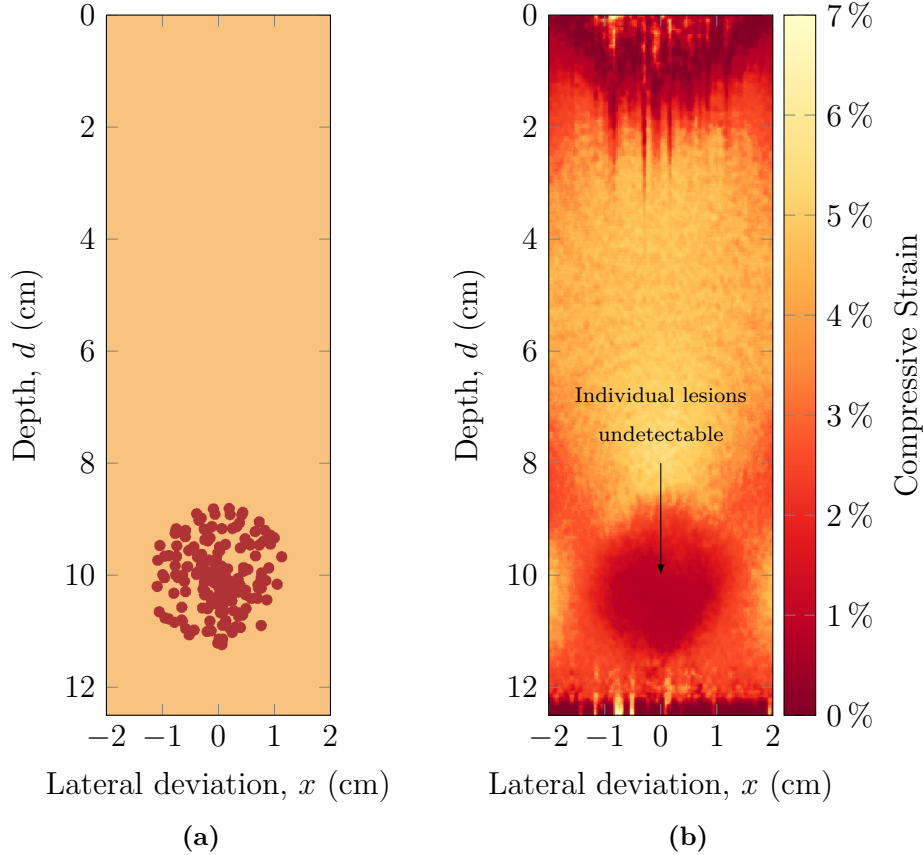


Fig. 3.18: Stiffness map (a) and corresponding elastogram (b) for a group of small lesions with a density of 10 lesions per cm^2 grouped in a 2.5 cm diameter circle at a depth of 10 cm interrogated with a 4 MHz probing frequency and 5 % applied strain. In (a), white regions are regular tissue while black regions are the small lesions. In the elastogram, individual lesions do not stand out, rather the entire region of lesions appears as one large region of unhealthy tissue.

Similar to the results shown in Fig. 3.17, changing the size of the individual small lesions does have an effect on the measured strain as seen in Fig. 3.19. In this case, when individual lesions are small, the total area occupied by lesions is lesser which results in a lesser average tissue stiffness over the grouped lesion region.

Note that although the elastography algorithm was able to detect the larger

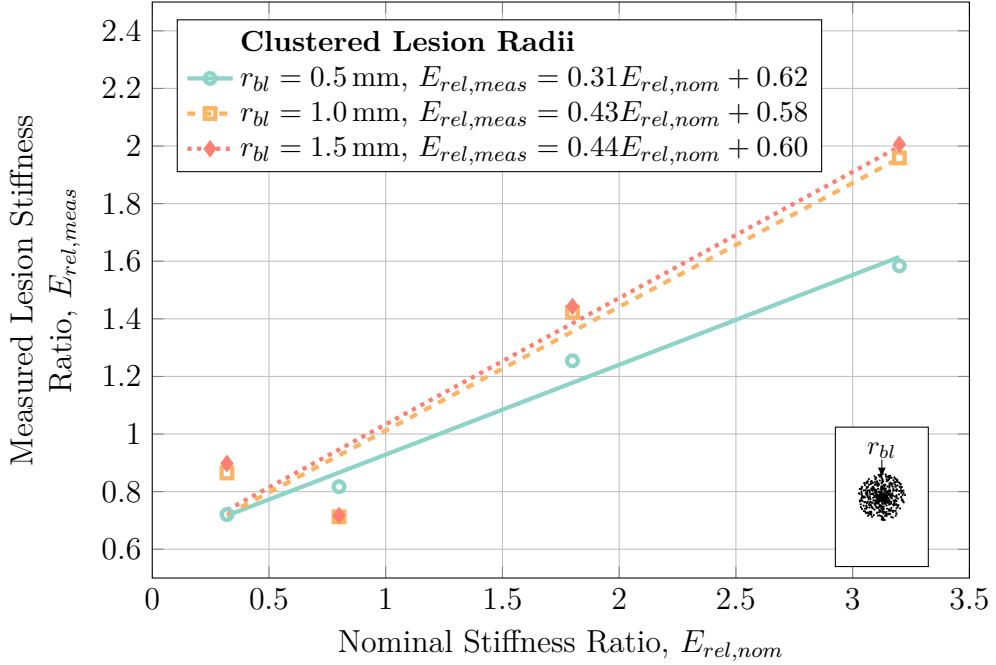


Fig. 3.19: Characterization of lesion radius for a group of numerous smaller lesions with a density of 30 lesions per cm^2 comprising a large area with a diameter of 2.5 cm at a depth of 10 cm interrogated with a 4 MHz probing frequency and 5% applied strain. Detection sensitivity decreases with decreasing individual lesion size, as expected. Lines represent linear regressions of the data.

lesion-filled regions in these simulations, it was completely unable to discern the individual lesions comprising those regions. This is not surprising due to both the generated strain fields in the healthy tissue throughout the larger lesion area as well as the results presented in Fig. 3.9 showing poor detection sensitivity for lesions with diameters $\leq 1\text{ cm}$ while the individual lesions in this simulation had diameters of the scale of 0.5 mm – 1.5 mm.

Finally, in order to place these results within the context of a real scenario in humans, a more complicated model utilizing an MRI-acquired lesion and slides from the Visible Human Project [126] was developed. Specifically, lesion geometry was taken from a real deep tissue injury in a pig model imaged using T_2^* -weighted MRI. The human geometry was taken from a transverse

plane slice across the left ischial tuberosity such that the lesion was placed immediately superficial to the boney prominence. For this model, the overall lesion width and lesion depth were examined with results shown in Figs. 3.20 and 3.22 respectively.

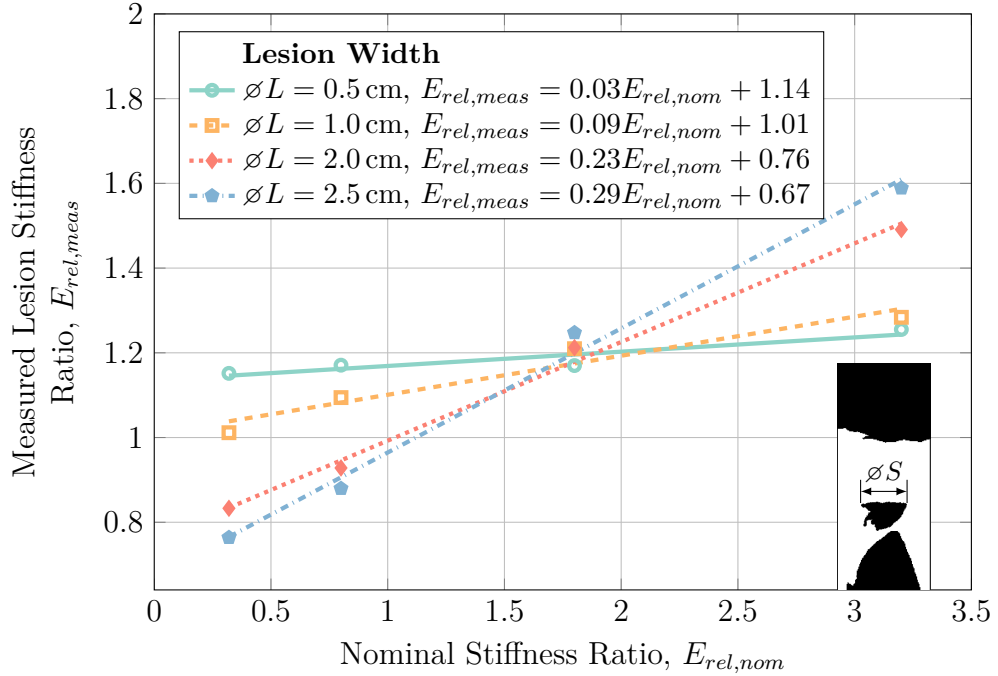


Fig. 3.20: Characterization of lesion width in a Visible Human-MRI model for lesions at a depth of 7.25 cm interrogated with a 4 MHz probing frequency with 5 % applied strain. Small lesions (with a width $\leq 1.0 \text{ cm}$) are severely misrepresented and portray general over-estimation of lesion stiffness larger lesions. Lines represent linear regressions of the data.

In Fig. 3.20, it is clear to see than small lesions (with a diameter $\leq 1.0 \text{ cm}$) are almost impossible to adequately detect (although larger lesions will be adequately detectable). It is hypothesized that this phenomenon is due to the excessive strain apparent above the boney prominence that is seen in the resultant elastogram given in Fig. 3.21 such that the lesion is “washed out” by the strain field developed by the relatively stiff bone nearby.

In Fig. 3.22, there is little to no dependence of the detection sensitivity

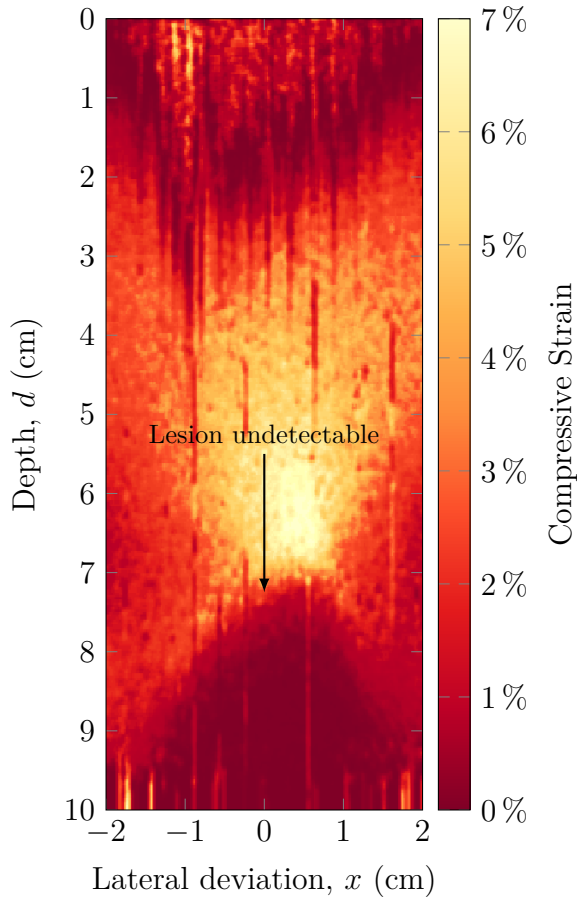


Fig. 3.21: Elastogram for a 0.5 cm wide lesion embedded in the Visible Human-MRI model domain at a depth of 7.25 cm interrogated at 4 MHz with an applied strain of 2.5 %. The lesion is not visible in the resultant elastogram.

on the lesion depth in the Visible Human-MRI model with all depth curves displaying the same profile. However, deeper lesions (lesions closer to the bony prominence) have stiffnesses that are over-estimated with respect to their superficial counterparts. This is hypothesized to be due to the increased strain field present in all of the soft tissue located immediately superior to the bony prominence, but should not pose a serious problem for imaging lesions of this nature.

Numerical values for the characterization plots presented here are given in

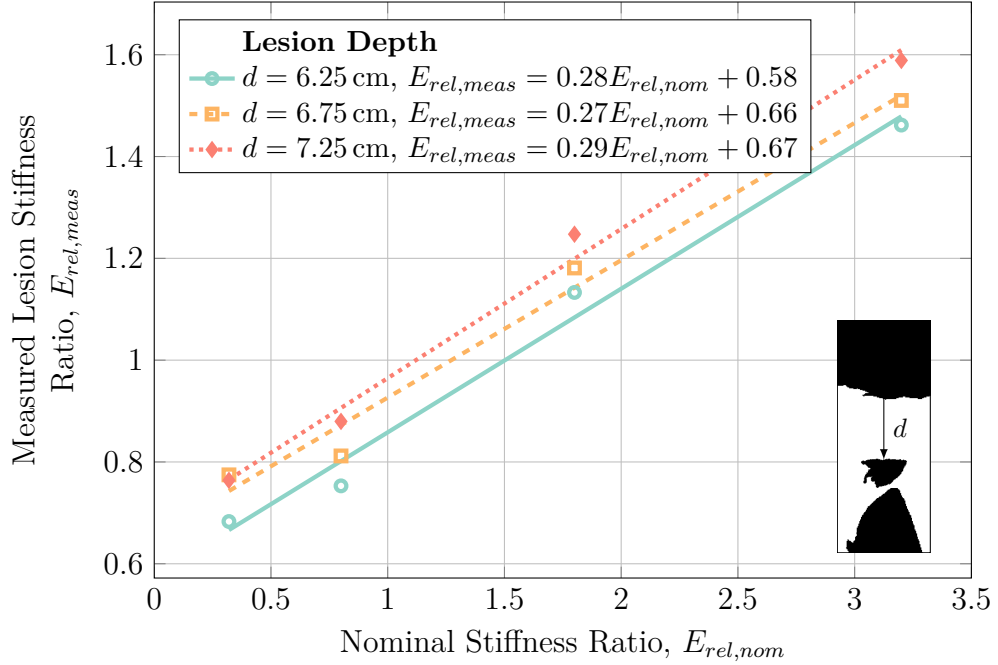


Fig. 3.22: Characterization of lesion depth in a Visible Human-MRI model for lesions with a width of 2.5 cm interrogated with a 4 MHz probing frequency and 5 % applied strain. Deeper lesions (closer to the bony prominence) are have slightly overestimated lesion stiffness ratios as opposed to more superficial lesions while detection sensitivity is not affected by lesion depth. Lines represent linear regressions of the data.

Section A.1 of Appendix A.

3.3.4 Physical Phantom Validation

In order to ensure that the models presented here represented physical realities, a small subset of the cases studied were modelled in a physical phantom, specifically for three lesions with stiffness ratios of 0.56, 1.80, and 3.20 with a diameter of 2.0 cm and at a depth of 3.5 cm, interrogated at 8 MHz with approximately 5 % applied strain. The results of this study are summarized in Fig. 3.23.

As can be seen in Fig. 3.23, a relatively simple (although inexact) rela-

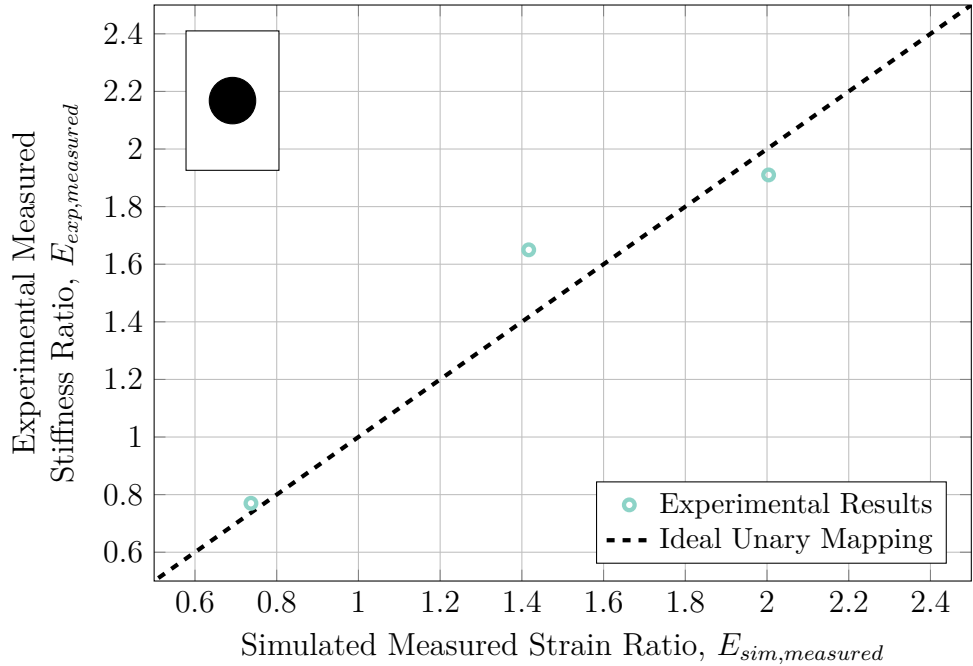


Fig. 3.23: Relation between simulated measured strain ratios and experimental measured strain ratios for a lesion at a depth of 3.5 cm and diameter of 2.0 cm showing general agreement between simulated and experimental cases. Idealization errors are the most likely the cause of the differences seen between simulated and experimental cases.

tionship between simulated and experimental measured strain ratios exists. It must be noted that the finite-element simulations of b-mode image formation and tissue deformation presented here are idealizations of reality and idealization errors such as the ultrasound pulse profile and plane-strain assumption no doubt contributed to the difference seen in Fig. 3.23.

It must be noted that in order to acquire quasi-static elastography results in the physical phantom, the ultrasound transducer was required to be manually manipulated to cause indentation in the phantom, as the technique would most likely be performed in a clinical setting. This was found to be problematic as the ultrasound transducer was difficult to maintain perfectly perpendicular and in-plane during the compression (largely due to the necessity of using coupling

might affect the simulation results, the model geometry extended laterally by 5 cm in either direction from the centreline. Simulations were run until the axial displacement at the focal point returned to 1 % of its maximal value during the entire simulation—at this point, the tissue was considered to be “relaxed” after being disturbed by the acoustic radiation force. Sample source code for calculating these finite-element models using COMSOL Multiphysics® is given in listing B.5 in Appendix B.

$$\vec{u} = 0, \quad \Gamma = \Gamma_{bottom} \quad (4.13a)$$

$$u_y = 0, \quad \Gamma = \Gamma_{top} \quad (4.13b)$$

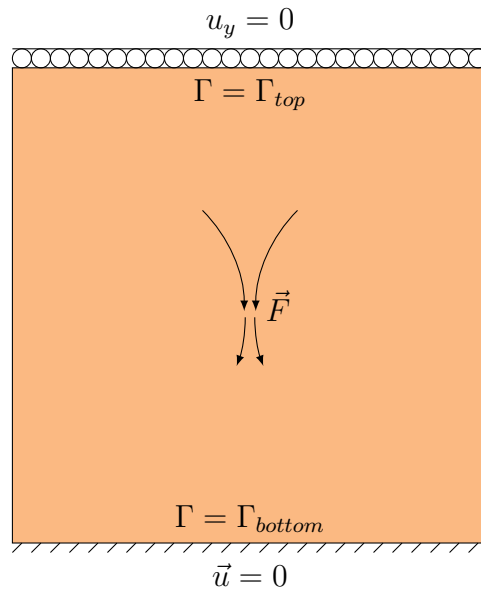


Fig. 4.1: Boundary conditions used in the finite-element calculations of soft tissue deformation.

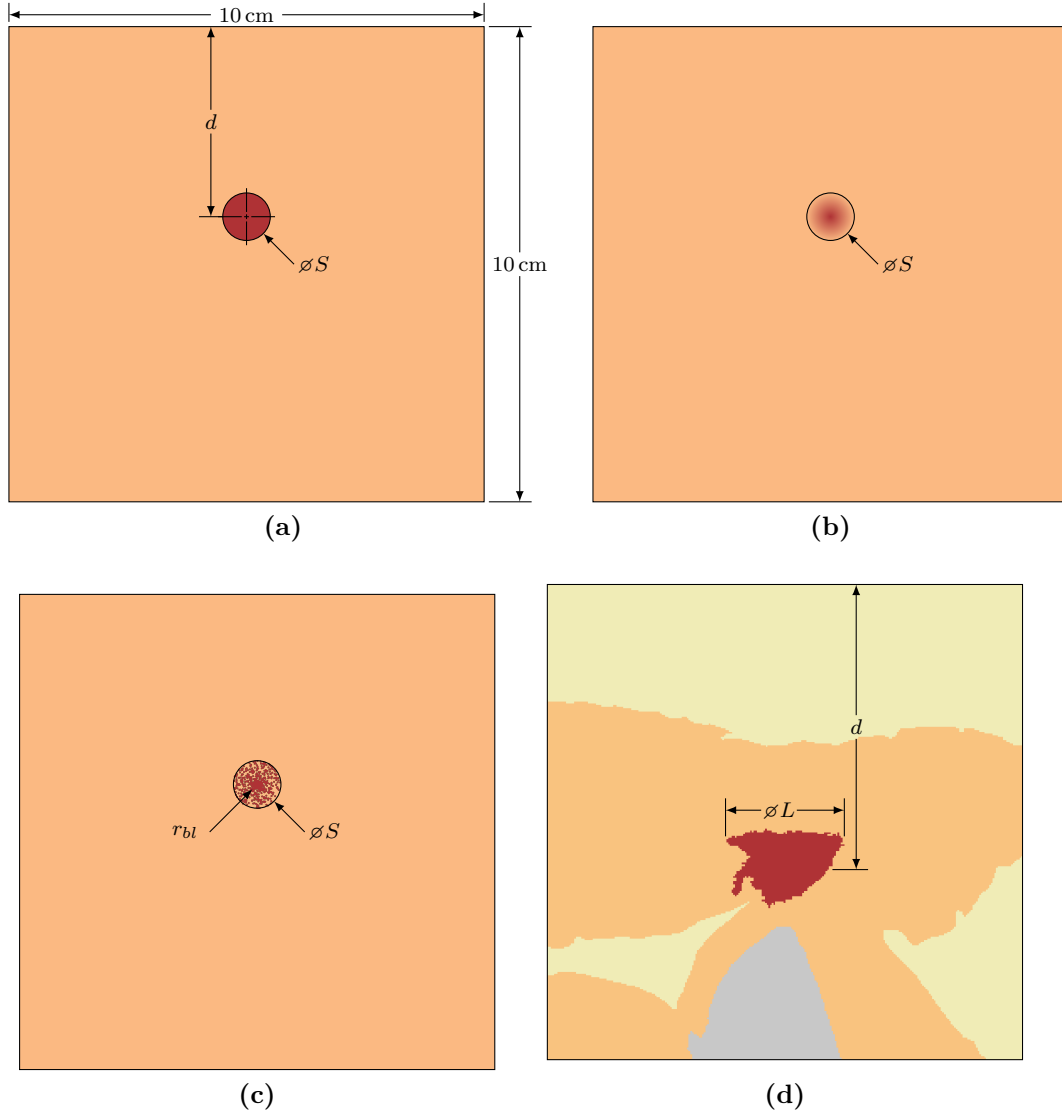


Fig. 4.2: Schematics of the lesion models that were investigated using acoustic radiation force impulse imaging showing (a) a spherical hard-boundaried lesion, (b) a spherical blurred-boundary lesion, (c) a cluster of numerous small lesions composing a larger lesionous region, and (d) the geometry from an MRI-acquired deep tissue injury overlaid on a slice from the Visible Human Project such that the injury lesion was located immediately superior to an ischial tuberosity.

and the width (and overall size) of the MRI-acquired lesion in the Visible Human model. The range of values of these investigated parameters are listed in Table 4.4.

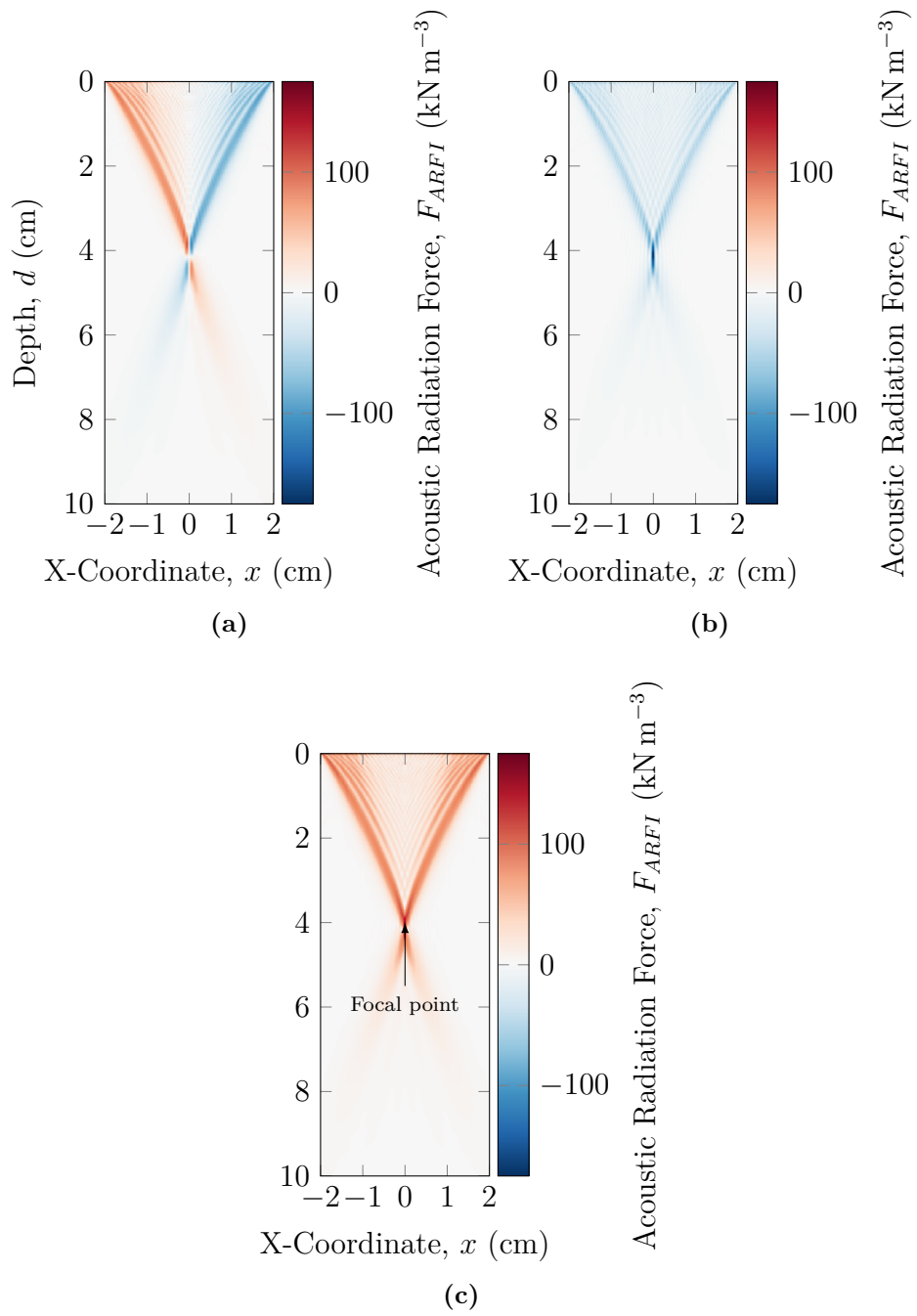


Fig. 4.3: Sample acoustic radiation force distribution in the (a) lateral and (b) axial directions, and (c) the resultant L^2 -norm generated by a 2 MHz transducer operating with an aperture of 4 cm focusing an acoustic beam at a depth of 4 cm continuously for 150 μ s applying a pressure of 3.35 MPa.

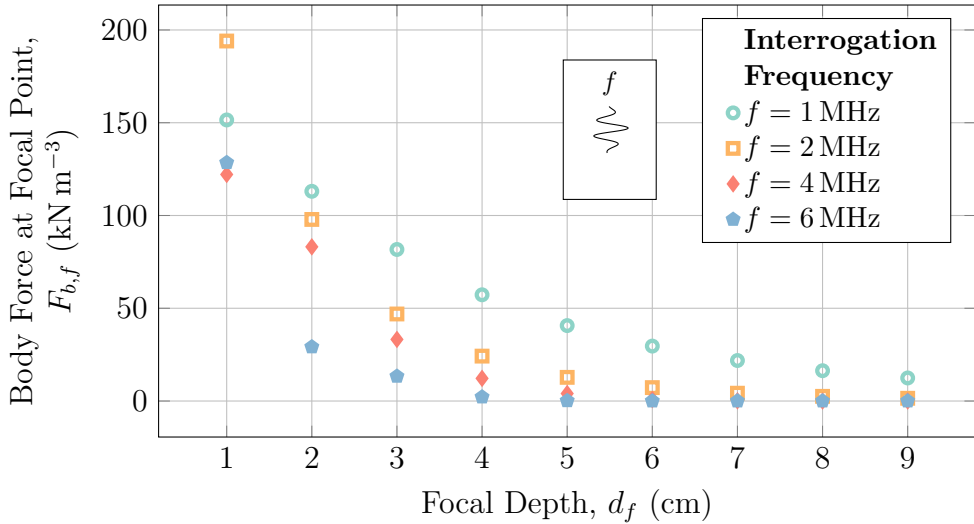


Fig. 4.4: Effect of depth and interrogation frequency on the magnitude of acoustic body forces developed in tissue. Increasing the interrogation frequency or the focal depth results in lesser body loads experienced by the tissue at the focal point, with the greatest loss of magnitude resulting from focal depth.

As Fig. 4.4 shows, increasing focal depth and probing frequency drastically decreases the magnitude of the force at the focal point of the tissue. In general, forces that are greater in magnitude are ideal as the deflection in the tissue that they cause must be detectable by the same transducer that is applying the forces—if the resulting deflections are too low, the tracking waves sent by the transducer will not be able to distinguish the motion. For the Siemens ACUSON S2000™ machine used in the validation of these studies, this lower limit is quoted as being $1/100$ of the applied wavelength, or approximately $1.7 \mu\text{m}$ for a 9 MHz probing frequency [114].

Since the forces developed in the tissue represent a transfer of energy, theoretically increasing the amount of energy input into the system should increase, or at least assist in greater amount of energy being transferred to the tissue. One way of increasing the amount of energy applied to the tissue by the transducer is to increase the size, or the “aperture” of the transducer—an

aperture of 8 cm will use twice as many physical pulsing elements than an aperture of 4 cm. To study this, the magnitude of the body force at the focal point was studied in simulation as the aperture changed. The results of this study are shown in Fig. 4.5.

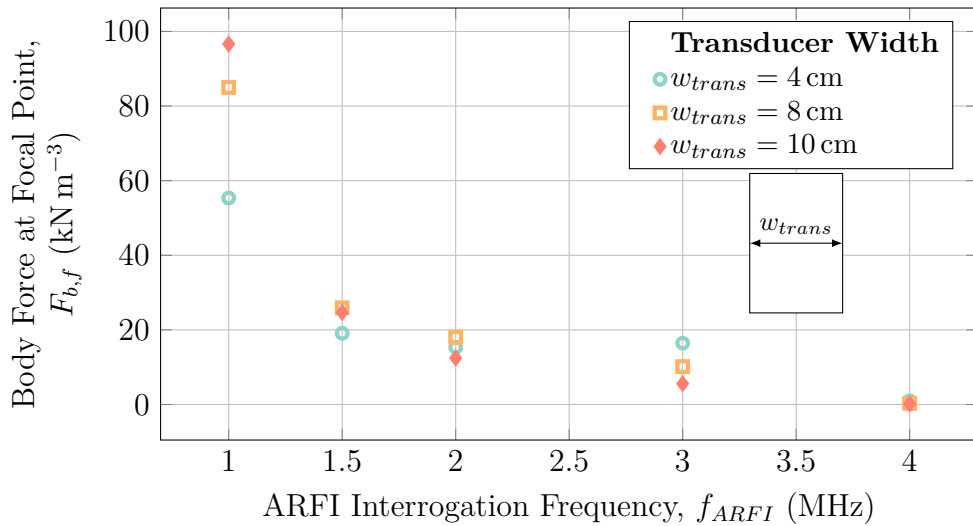


Fig. 4.5: Effect of transducer aperture on the magnitude of developed acoustic radiation force at the focal depth of 6 cm for a range of ultrasound interrogation frequencies.

Surprisingly, there was little consistent effect of the transducer aperture size on the magnitude of the acoustic radiation force that was seen at the focal point. As expected, the greatest and least forces were developed with the lowest and highest frequencies studied, respectively, as per the results found in Fig. 4.4. The greatest effect of the transducer aperture size occurred at a frequency of 1 MHz while the least effect of the transducer aperture size occurred at a frequency of 4 MHz which correlate to the greatest and least amount of energy input into the system respectively.

Another method of increasing the amount of energy transferred into the system is to increase the duration of time that the system is applying pressure

to the tissue. In other words, increasing the number of pulse cycles (insonification time) should generate more energy until tissue is under quasi-steady-state insonification. To investigate this, the effect of the number of acoustic pulse cycles—related to the insonification time by equation 4.15—was investigated, with the results shown in Fig. 4.6.

$$t_{inson} = \frac{n_c}{f_{applied}} \quad (4.15)$$

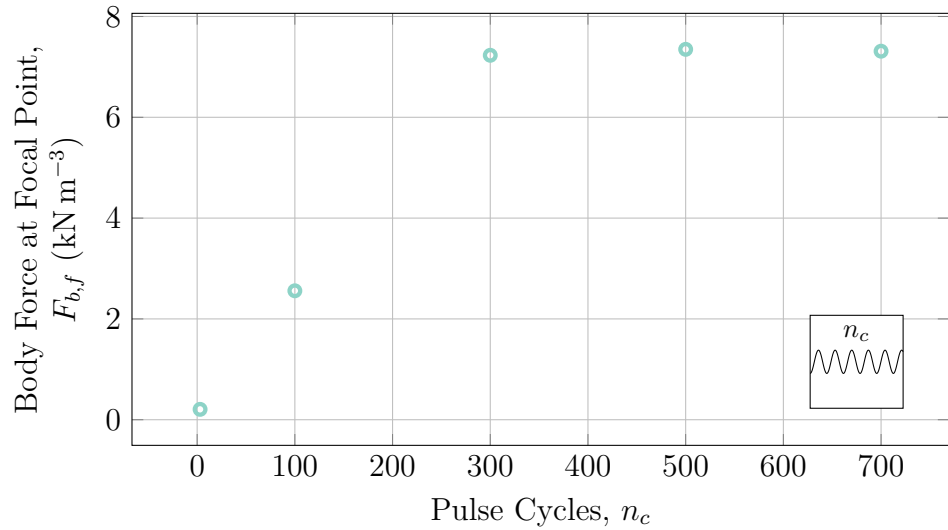


Fig. 4.6: Magnitude of the developed acoustic radiation force in relation to the number of applied pulse cycles in tissue at a focal depth of 6 cm using a transducer aperture of 4 cm and source pressure of 3.35 MPa.

As expected, increasing the number of pulse cycles increased the magnitude of the acoustic radiation force seen at the focal point until the domain reached quasi-steady-state at approximately 300 pulses, or 150 μs of insonification. At this point, since the calculation of the acoustic radiation force given in equation 4.10 relies on the *average* intensity during the insonification time, increasing the number of pulse cycles has little to no effect on the resulting acoustic radiation force.

One further way of increasing the energy in the system and thereby increasing the magnitude of the acoustic radiation force at the focal point is to increase the amount of pressure applied by the individual transducer elements. To investigate this technique, a range of acoustic pulsing element pressures were applied across a range of focal depths and the resulting acoustic radiation force at the focal point was monitored. The results of this study are shown in Fig. 4.7.

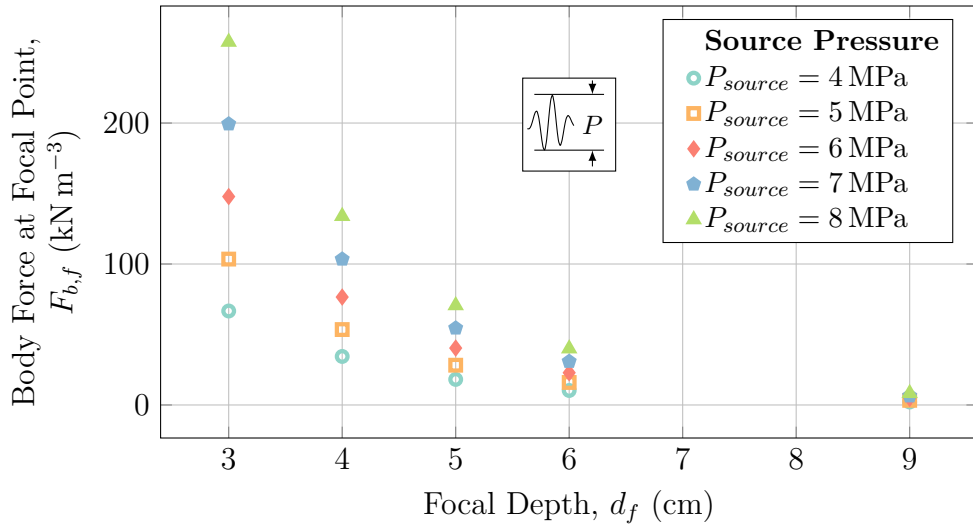


Fig. 4.7: Strong dependence on source pressure of focal point force

As Fig. 4.7 shows and as was expected, increasing the applied pressure results in greatly increasing the magnitude of the resultant acoustic radiation force developed in the tissue—doubling the applied pressure results in nearly quadrupling the magnitude of the acoustic radiation force at all depths. Note however that a critical measure of the safety of ultrasound is the cavitation pressure of the ultrasonic wave as it travels through the tissue. The safety of cavitation is described by the “mechanical index”, MI , which is calculated according to equation 4.16 [96] where P_r is the peak rarefaction pressure in the

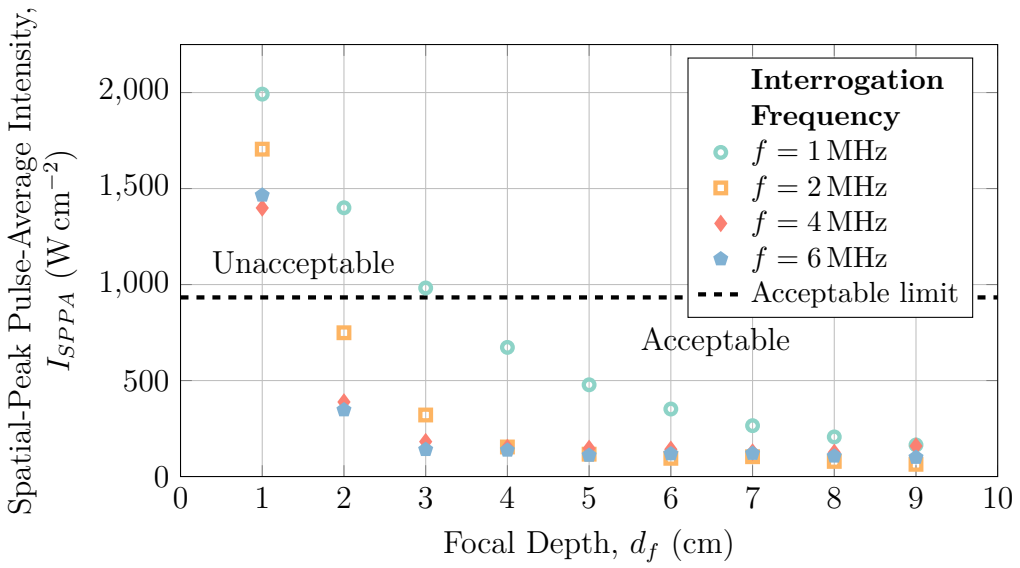


Fig. 4.8: The effect of depth and interrogation frequency on the spatial peak pulse average intensity, I_{SPPA} . I_{SPPA} is a measure of the safety of high-intensity ultrasound applications, with I_{SPPA} values below 933 W cm^{-2} considered acceptable for non-cardiovascular and non-fetal imaging.

4.3.2 Temporal Finite-Element Model of Soft Tissue Deformation

As ARFI imaging relies upon the detection of soft tissue deformation in response to the transducer-applied acoustic radiation force, a key parameter of interest is the magnitude of the deformation generated in the tissue in response to the applied loads. To this end, the temporal finite-element model of soft tissue deformation described in Section 4.2.3 was used to determine the magnitude of the deformation caused by varying acoustic radiation force parameters.

Fig. 4.9 show the relationship between the maximum induced tissue displacement, $|v|_{max}$, generated by acoustic radiation forces in soft tissue for a range of focal depths and interrogation frequencies. As expected, significantly

greater deformation is generated with shallower focal depths. Further, increases in the interrogation frequency generally resulted in lesser displacement induced in the tissue. The results obtained using a 1 MHz interrogation frequency stood apart from the higher frequencies investigated. This is likely due to the excess acoustic radiation force produced at such low frequencies shown in Figs. 4.4 and 4.8.

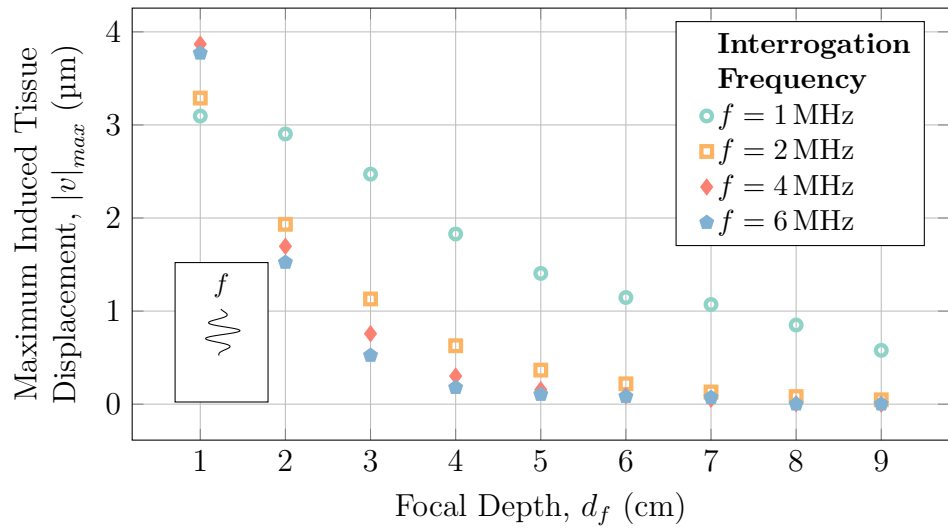


Fig. 4.9: Magnitude of deformation resulting from ARFI interrogation at various focal depths and interrogation frequencies with a transducer aperture of 4 cm and source pressure of 3.35 MPa.

To reiterate the results seen in Fig. 4.7, the maximum induced tissue displacement generated by the applied acoustic radiation force at various focal depths for various source pressures was investigated, the results of which are given in Fig. 4.10. These results echo the results seen in Fig. 4.7, where doubling the applied pressure resulted in approximately quadrupling the maximum displacement seen in the tissue across all focal depths as was expected.

The results given in Fig. 4.10 were further investigated by examining the effect of the interrogation frequency on the maximum induced tissue dis-

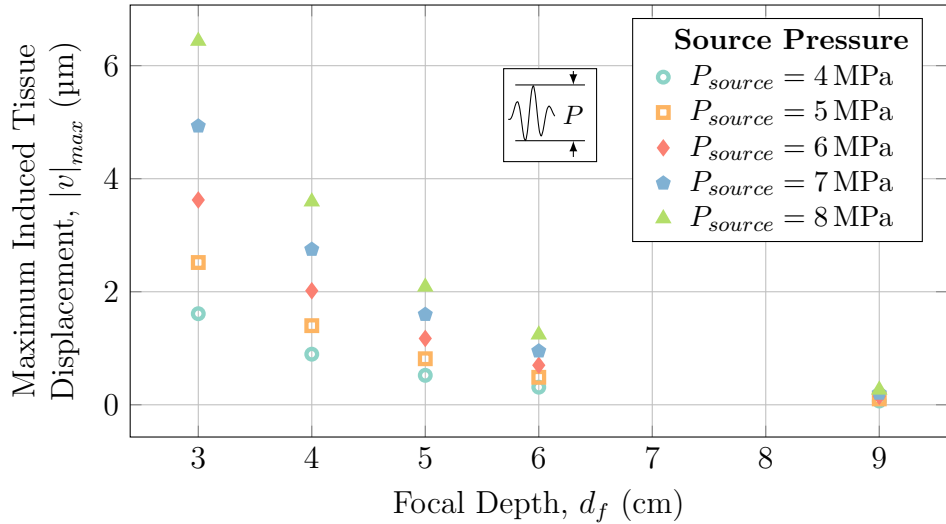


Fig. 4.10: Magnitude of deformation resulting from ARFI interrogation at various focal depths and source pressures at an interrogation frequency of 2 MHz with a transducer aperture of 4 cm and source pressure of 3.35 MPa.

placement. As expected, increasing the interrogation frequency resulted in decreases in the magnitude of deformation experienced by the tissue across all source pressures investigated. Further, increasing the amount of source pressure applied by the transducer into the tissue resulted in greater levels of tissue deformation. Of note is that the use of a 1 MHz interrogation frequency affected the magnitude of tissue deformation across the different source pressures much more than any of the higher interrogation frequencies studied, further echoing the results seen in Fig. 4.9.

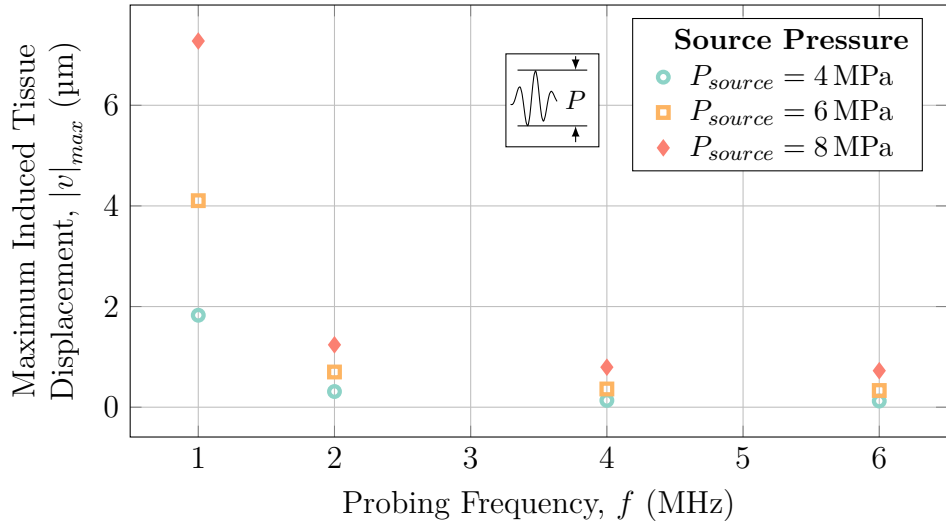


Fig. 4.11: Magnitude of deformation resulting from ARFI interrogation at various interrogation frequencies and source pressures at a depth of 6 cm with a transducer aperture of 4 cm and source pressure of 3.35 MPa.

4.3.3 Numerical Characterization of Acoustic Radiation Force Impulse Imaging

Beyond understanding the general nature of acoustic radiation forces in soft tissue, the effects of these forces in the presence of deep tissue injuries must also be characterized for ARFI imaging to become a useful diagnostic tool for such injuries. In order to investigate the suitability of ARFI imaging for the detection of DTI, the procedure outlined in Section 4.2.4 was carried out on a range of models with varying parameters of interest. The results of these characterizations are presented here.

In order to understand the effect of general lesion size on the detection sensitivity of ARFI imaging, hard-boundaried spherical lesions of various radii were placed in a soft tissue domain at a depth of 4 cm and insonated at 2 MHz with an aperture of 4 cm and pressure of 3.35 MPa for 150 μs (300 pulse cycles).

The results of this characterization are presented in Fig. 4.12.

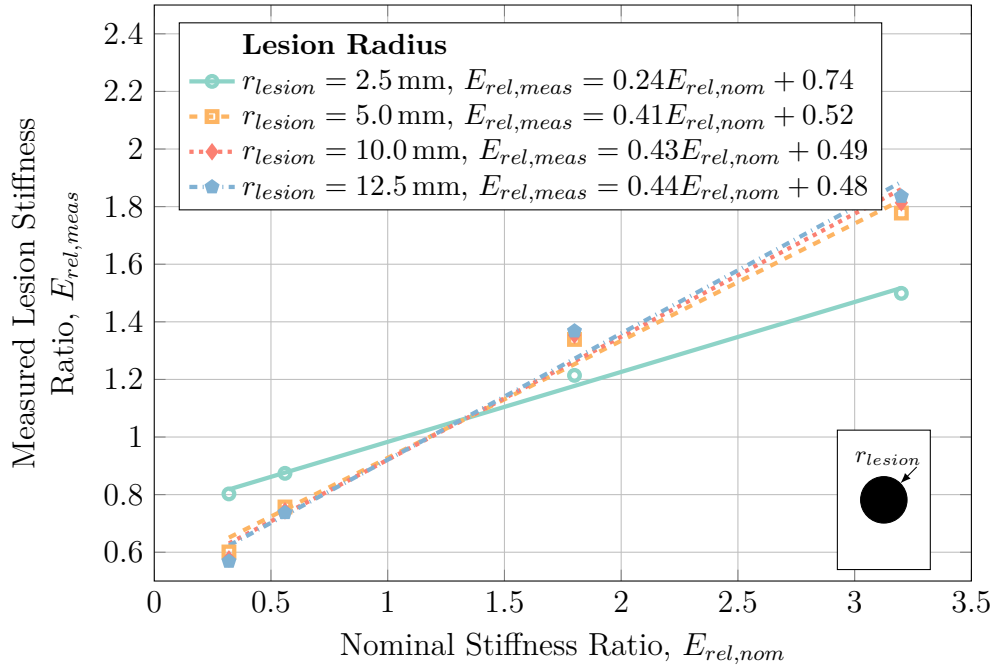


Fig. 4.12: Numerical characterization of the ARFI imaging-acquired stiffness ratios acquired with varying lesion radii for a hard-boundaried lesion at a depth of 4 cm using an ARFI probing frequency of 2 MHz.

As Fig. 4.12 shows, ARFI imaging was able to detect the presence of both stiff and unstiff lesions of all sizes, however the technique both severely underestimated the stiffness of stiff lesions and overestimated the stiffness of unstiff lesions—leading to the observation that ARFI imaging has a relatively low detection sensitivity with regards to both stiff and unstiff deep tissue injury lesions. Fig. 4.12 also shows that above lesion radii of approximately 2.5 mm, the lesions size does not have any appreciable effect on the detection sensitivity of the technique. Below this limit, however, lesions will be much more difficult to detect as the differences between them and the surrounding tissue are minimized.

To further corroborate these results, the mean-squared error associated with the various lesion radii was calculated according to equation 4.17 where

\hat{Y}_i are the true lesion stiffness ratios and Y_i are the measured lesion stiffness ratios. The results of this calculation with regards to lesion radius are given in Fig. 4.13. Figure 4.13 explicitly depicts a greater degree of error for lesions with radii of 2.5 mm, with only marginal improvements in measurement error resulting from increasing the lesion radius beyond 5.0 mm.

$$MSE = \frac{1}{n} \sum_{i=1}^n (\hat{Y}_i - Y_i)^2 \quad (4.17)$$

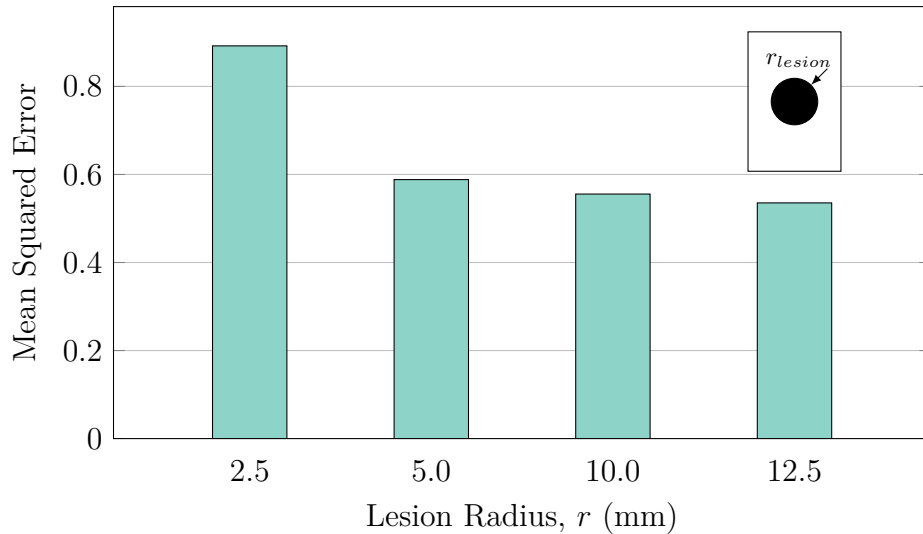


Fig. 4.13: Mean squared error between the true and measured lesion stiffness ratios for increasing lesion radii for a hard-boundaried lesion at a depth of 4 cm using an ARFI interrogation frequency of 2 MHz.

In order to investigate the effect of lesion depth on detection sensitivity, the use of ARFI imaging to distinguish spherical hard-boundaried lesions with radii of 10 mm was investigated at a range of depths, with the results shown in Fig. 4.14. As Fig. 4.14 shows, there is almost no dependence of the detection sensitivity on the depth of the lesion. However, it must be noted that the deformations resulting from acoustic radiation force impulses will be of such small magnitudes that they will not be detectable using current ultrasound

technology. To understand the limitations of depth in ARFI imaging, please refer to Section 4.3.2.

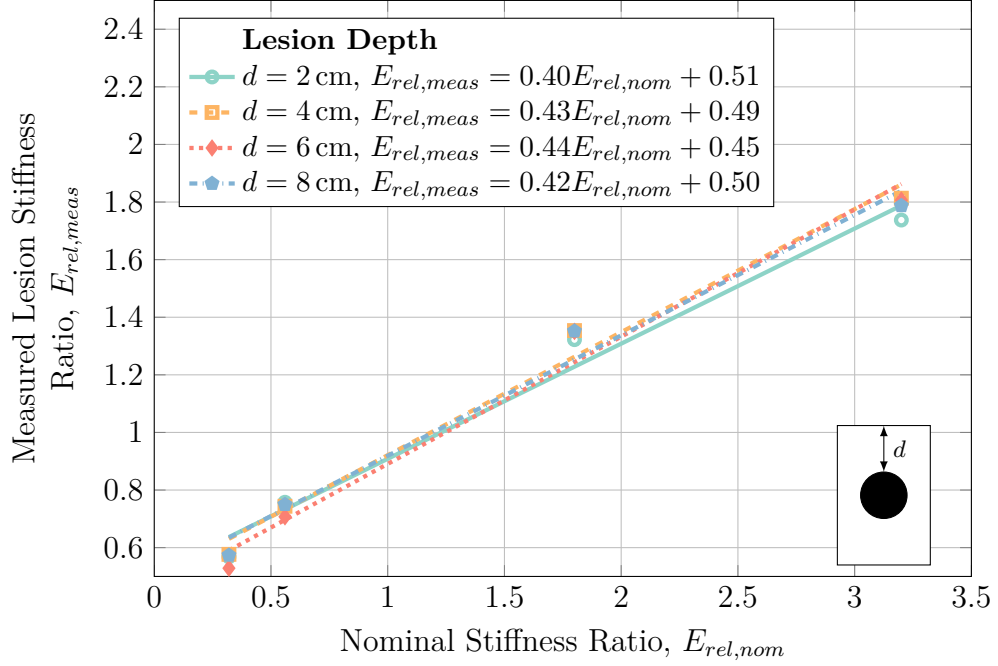


Fig. 4.14: Numerical characterization of the ARFI imaging-acquired stiffness ratios acquired with varying lesion and focal point depths for a hard-boundaried 0.5 cm radius lesion using an ARFI probing frequency of 2 MHz.

Fig. 4.15 portrays the mean-squared-error of the measured lesion stiffness across the various depths examined. Although the variance in error between the different depths is not substantial, both very shallow—lesions at a depth of 2 cm or less—and very deep—lesions at a depth of 8 cm or more—were found to have the greatest measurement error. In shallow tissue, this increase in error may be due to an inability to appropriately focus the acoustic radiation force so close to the transducer whereas in deep tissue, the increase in error is likely due to the reduced magnitude of radiation force present due to the relatively large amount of tissue absorption.

Since the aforementioned hard-boundaried, spherical lesion cases represent

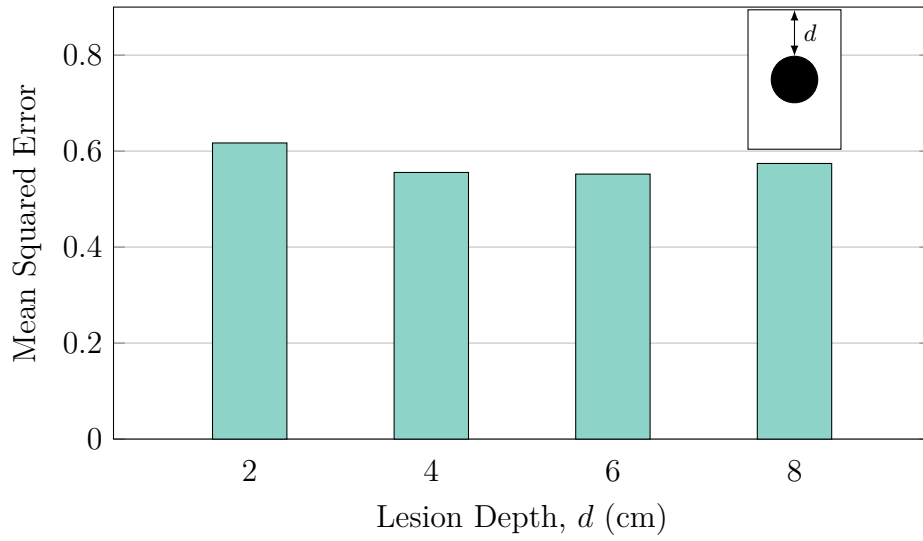


Fig. 4.15: Mean squared error between the true and measured lesion stiffness ratios for increasing lesion depths for a hard-boundaried 0.5 cm radius lesion using an ARFI interrogation frequency of 2 MHz.

simplifications of reality designed to obtain a general understanding of the ARFI technique, models representing more complicated geometry were also studied. Fig. 4.16 shows the simulated lesion stiffness ratios for a set of lesions with radii of 10 mm at a depth of 4 cm with blurred boundaries as described in Section 4.2.4. As Fig. 4.16 shows, there is no reliance of the detection sensitivity on the blur radius of the lesion, with the results shown repeating the results seen in Figs. 4.12 and 4.14.

The mean-squared error shown in Fig. 4.17 further supports this conclusion, with the error between different blur radii differing by just over 1%. This lack of sensitivity on the degree of lesion blurring presents a significant advantage over quasi-static elastography as it allows even lesions without well-defined boundaries to be detected.

It may also be possible that a diseased region of tissue is not a singular, continuous lesionous region, but rather an amalgamation of numerous small

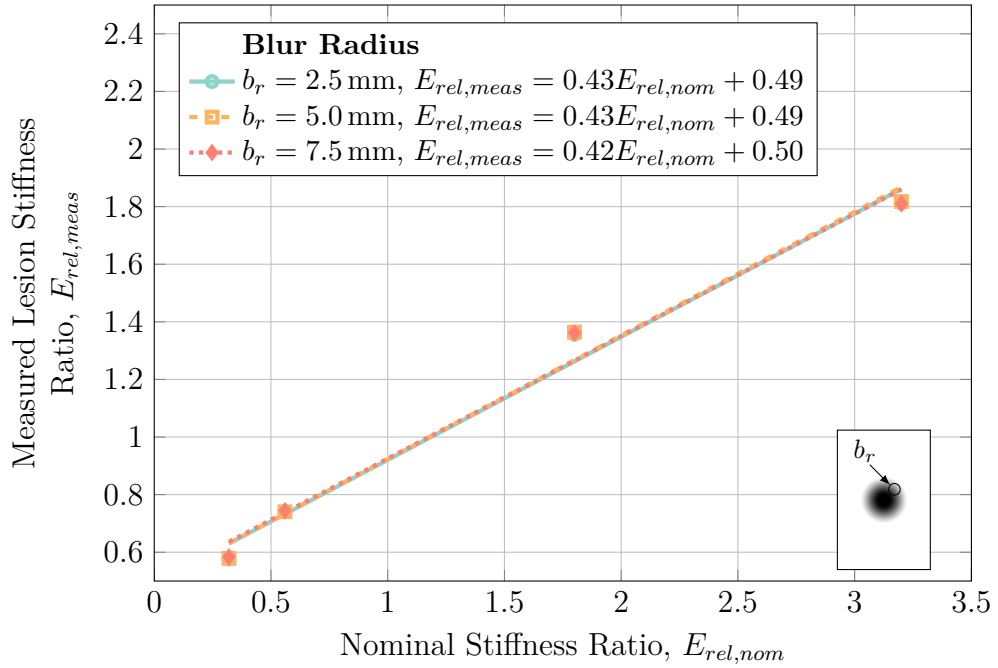


Fig. 4.16: Numerical characterization of the ARFI imaging-acquired stiffness ratios acquired with varying lesion and focal point depths for a blurred 1.0 cm radius lesion at a depth of 4 cm using an ARFI interrogation frequency of 2 MHz.

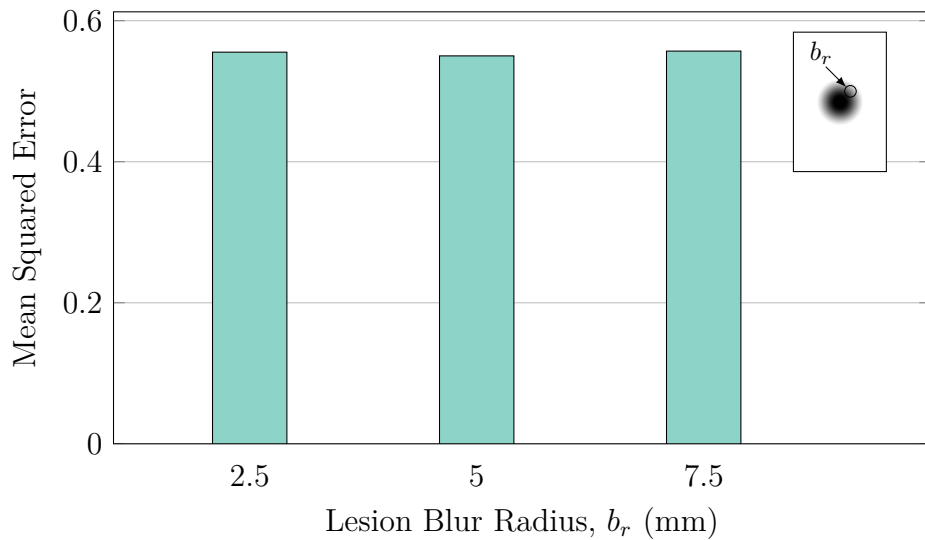


Fig. 4.17: Mean squared error between the true and measured lesion stiffness ratios for increasing lesion depths for a blurred 1.0 cm radius lesion at a depth of 4 cm using an ARFI interrogation frequency of 2 MHz.

lesions or damaged tissue which collectively compose a larger lesionous region.

To investigate the effect such a phenomenon would have on the detection sensitivity of ARFI imaging, the density and size of numerous small, clustered lesions were varied in models and the resulting measured stiffness ratios were investigated. Fig. 4.18 shows the characterization of the lesion cluster density—how many lesions are present per unit area—for densities ranging from 10 cm^{-2} to 40 cm^{-2} with small lesions of radius 1.0 mm. The centre of the lesionous regions were located at a depth of 4 cm in an overall region with a radius of 10 mm.

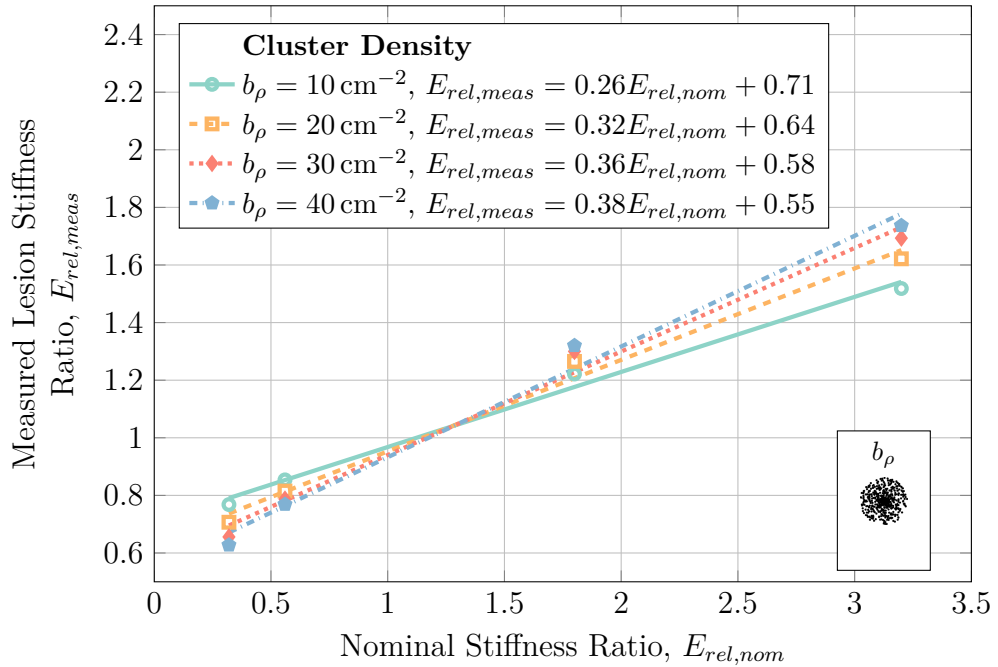


Fig. 4.18: Numerical characterization of the ARFI imaging-acquired stiffness ratios acquired with varying cluster densities for clustered 1 mm radius lesions within a 1.0 cm radius at a depth of 4 cm using an ARFI interrogation frequency of 2 MHz.

As Fig. 4.18 shows, increasing the cluster density results in monotonically increasing the detection sensitivity of the ARFI technique. This is as expected, as increasing the cluster density increases the total area contributing to the

modified tissue stiffness in the region, which in turn allows the ARFI technique to more readily distinguish the lesion. These results are further shown by the mean-squared error shown in Fig. 4.19 which shows the decrease in error attributed to increases in lesion cluster densities.

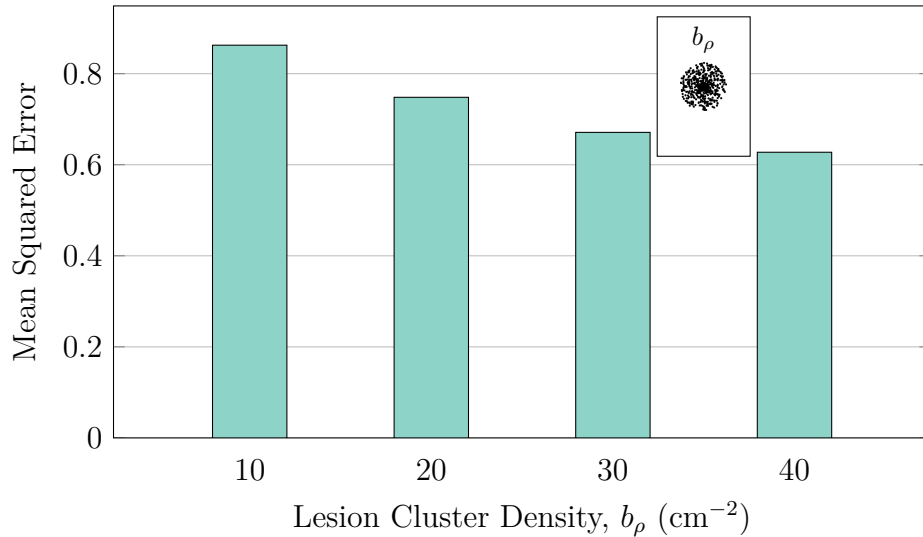


Fig. 4.19: Mean squared error between the true and measured lesion stiffness ratios for increasing lesion cluster density for clustered 1 mm radius lesions within a 1.0 cm radius at a depth of 4 cm using an ARFI interrogation frequency of 2 MHz.

Another method to alter the ratio of damaged to healthy tissue within the lesionous region is to alter the size of the individual lesions that comprise that region. This characterization was carried out using small lesions with radii ranging from 0.5 mm to 1.5 mm at a cluster density of 30 cm^{-2} , with the results given in Fig. 4.20.

As Fig. 4.20 shows, decreasing the individual lesion radii in the clustered model substantially decreased the detection sensitivity of the ARFI technique, again echoing the previous results where decreasing the ratio of damaged to healthy tissue in the lesionous region results in lesser detection sensitivity. This is confirmed by examining the mean-squared error of the results, which

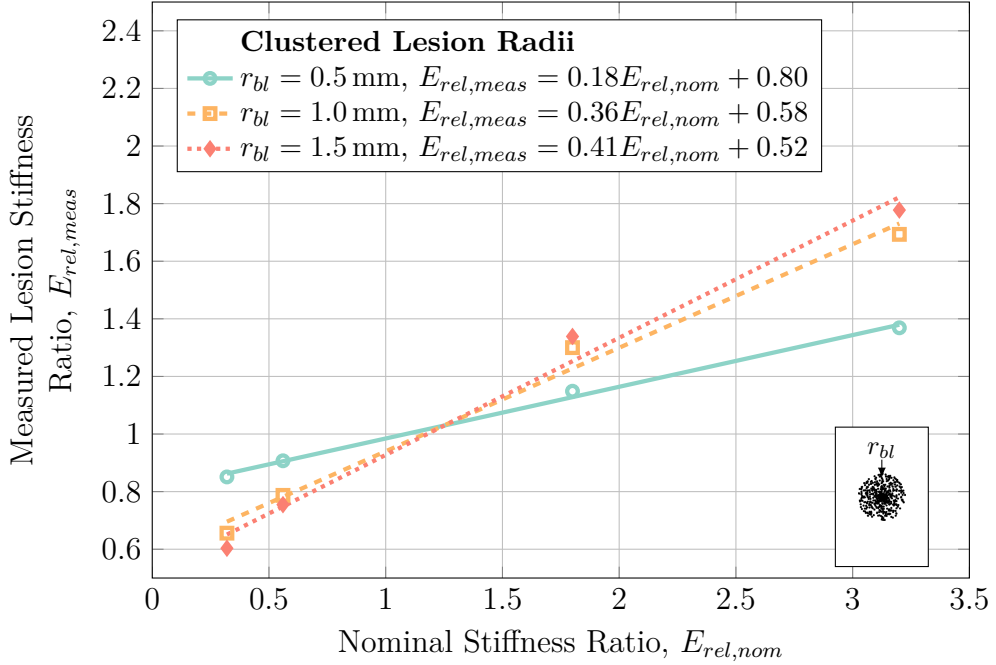


Fig. 4.20: Numerical characterization of the ARFI imaging-acquired stiffness ratios acquired with varying clustered lesion radii for clustered lesions with a density of 30 cm^{-2} within a 1.0 cm radius at a depth of 4 cm using an ARFI interrogation frequency of 2 MHz .

shows monotonically decreasing errors for monotonically increasing individual lesion radii.

While the aforementioned studies investigated generally spherical lesionous regions, this is unlikely to be the case in a real soft tissue domain. To further investigate ARFI imaging, a model utilizing complicated geometry arising from the combination of the MRI-acquired geometry of a deep tissue injury with the anatomical distribution of fat, muscle, and bone obtained from the Visible Human project [126] was created as described in Section 4.2.4. To investigate the effect of lesion size in this model, the lesion size, $\varnothing L$, was varied between 2.5 mm and 12.5 with the lesion being placed at a depth of 6 cm . The results of this characterization are shown in Fig. 4.22.

As Fig. 4.22 shows, decreasing the lesion width in the Visible Human

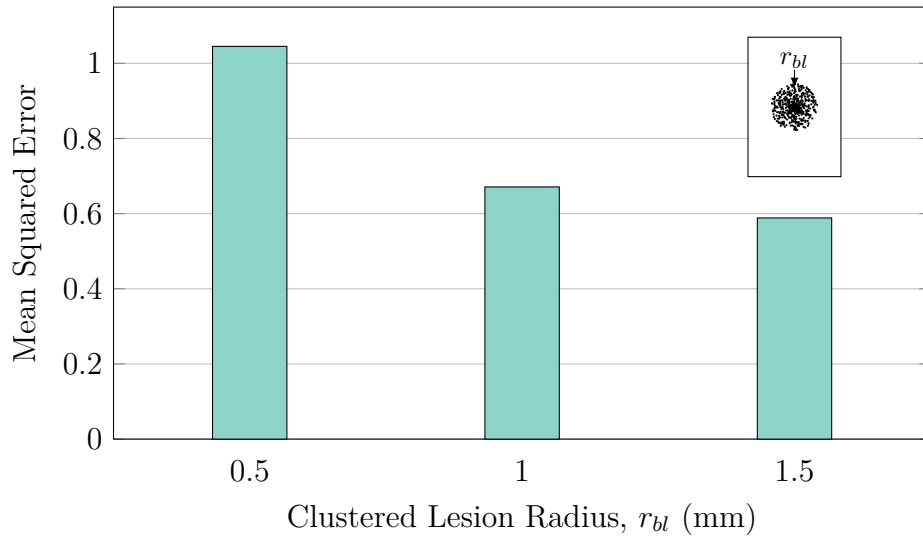


Fig. 4.21: Mean squared error between the true and measured lesion stiffness ratios for increasing clustered lesion radii for clustered lesions with a density of 30 cm^{-2} within a 1.0 cm radius at a depth of 4 cm using an ARFI interrogation frequency of 2 MHz .

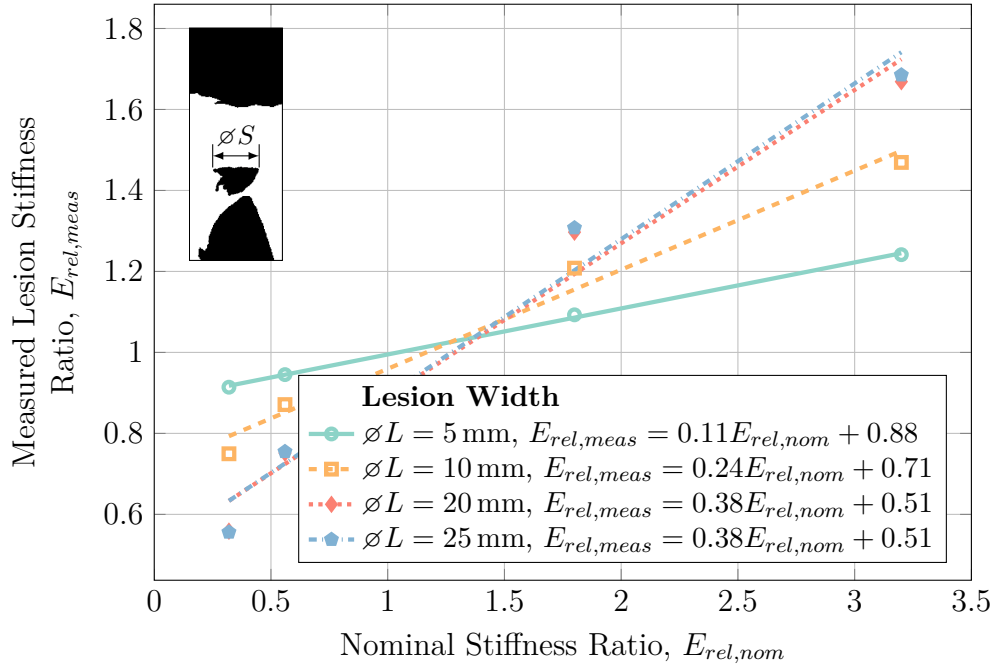


Fig. 4.22: Numerical characterization of ARFI imaging-acquired stiffness ratio with changing lesion radii for MRI-acquired lesion geometry in a Visible Human model at a depth of 6 cm using an ARFI interrogation frequency of 2 MHz .

model resulted in a decreased detection sensitivity which was echoed by the mean-square error of the results shown in Fig. 4.23. The detection sensitivity decreases with half-widths less than 10 mm in the Visible Human model as opposed to radii of 5 mm as found with the spherical lesion embedded in general soft tissue seen in Fig. 4.12. Although the reason for this is not immediately clear, possible differences lay in the depth at which the lesions were imaged at: the Visible Human model placed the lesion at a depth of 6 cm so as to have it lay immediately superior to the ischial tuberosity while the results for the spherical lesion were taken at a depth of 4 cm. Further, comparing the half-width of the Visible Human lesion to the radius of the spherical lesion may introduce errors as the overall area of lesionous tissue were different.

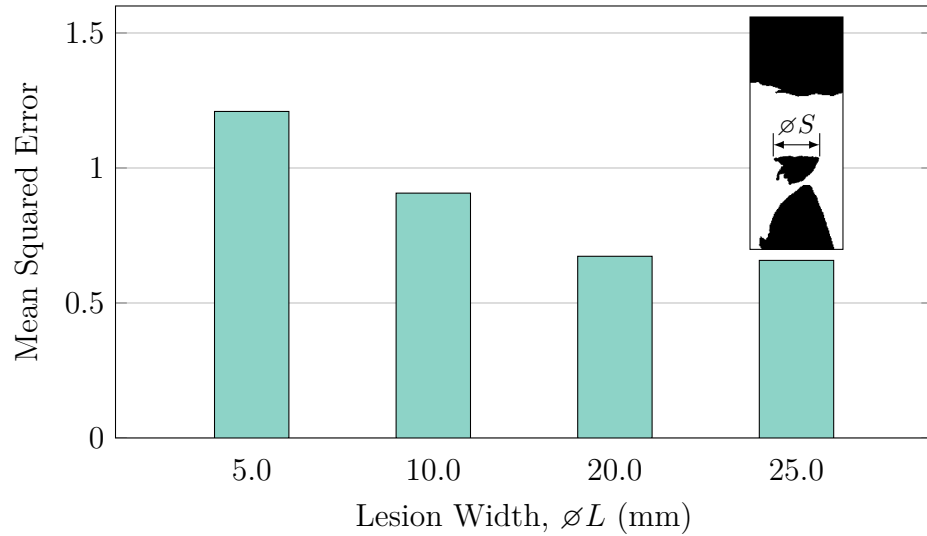


Fig. 4.23: Mean squared error between the true and measured lesion stiffness ratios for increasing lesion radii for MRI-acquired lesion geometry in a Visible Human model at a depth of 6 cm using an ARFI interrogation frequency of 2 MHz.

Numerical values for the characterization plots presented here are given in Section A.2 of Appendix A.

4.3.4 Physical Phantom Validation

In order to determine if the results presented in Section 4.3.3 represent valid simulations, validation experiments were carried out on a physical tissue mimicking phantom as described in Section 4.2.5. Fig. 4.24 shows the result of these experiments.

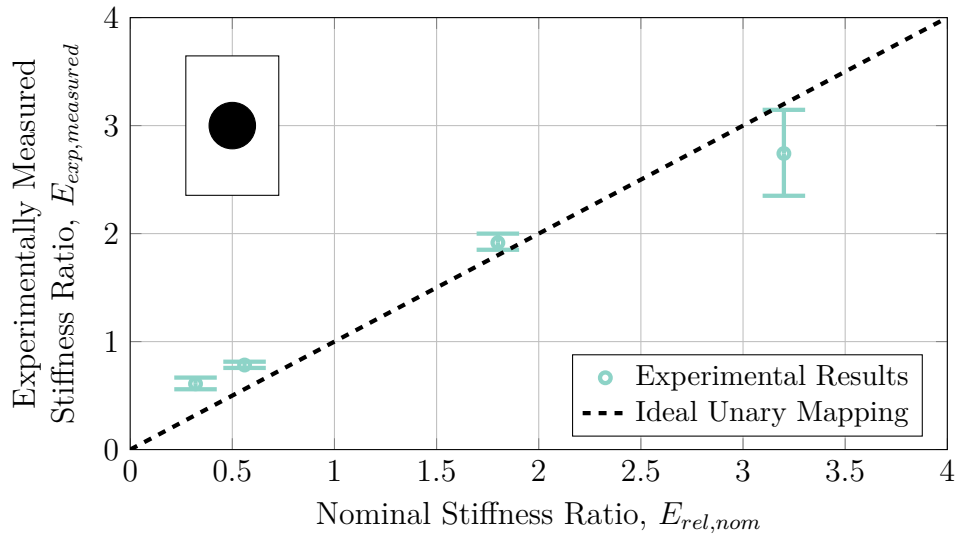


Fig. 4.24: Relation between nominally reported strain ratios of the tissue mimicking phantom and experimentally measured strain ratios for a lesion at a depth of 3.5 cm and diameter of 2.0 cm. Error bars represent the range of measurements acquired.

As the results seen in Fig. 4.24 show, ARFI imaging was found experimentally to significantly underestimate the stiffness of the stiffest lesions investigated—lesions with nominal stiffnesses of 3.2. For all other lesions investigated, ARFI imaging was shown to overestimate the lesion stiffness slightly. Although it is possible that the true stiffness ratio of the lesions in the phantom do not perfectly align with the manufacturer-reported nominal values, it is also possible that the acoustic radiation force developed by the ARFI transducer was not enough to substantially deform the stiffest of lesions, leading to

the stiffness being underestimated.

Fig. 4.25 compares the experimentally-acquired lesion stiffness ratios against measured stiffness ratios arising from parametrically identical simulated lesions. As Fig. 4.25 shows, although the experimentally measured stiffness ratios align well with the simulated stiffness ratios for relatively unstiff lesions ($E_{rel} < 1$), the simulated ARFI procedure was found to underestimate the stiffness of the stiff lesions that were investigated ($E_{rel} > 1$). The exact cause of this disparity is unclear and future work must be done in order to remedy this in the simulations that were performed in order to accurately understand ARFI imaging.

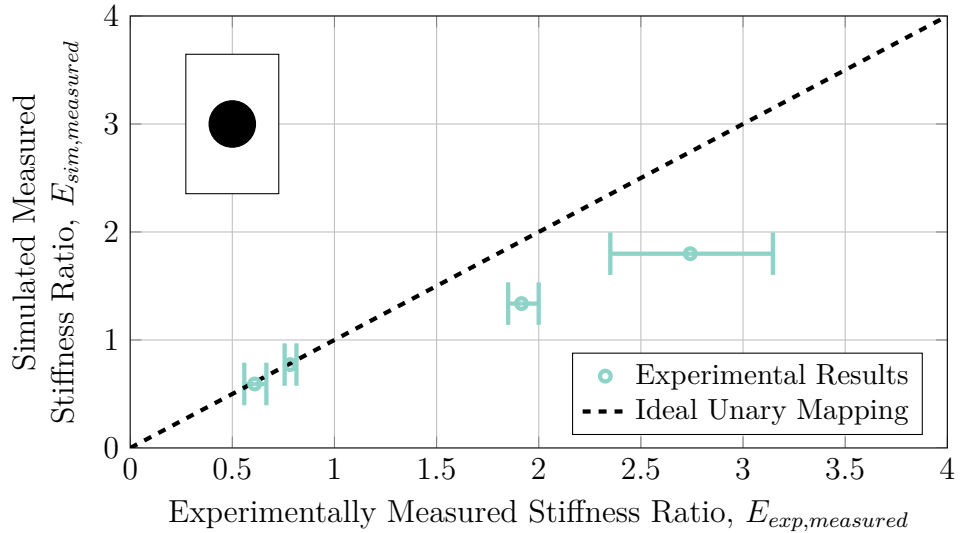


Fig. 4.25: Relation between simulated measured strain ratios and experimental measured strain ratios for a lesion at a depth of 3.5 cm and diameter of 2.0 cm.

4.4 Conclusion

The results presented in Section 4.3 represent a numerical characterization of the use of acoustic radiation force impulse imaging for the detection of deep

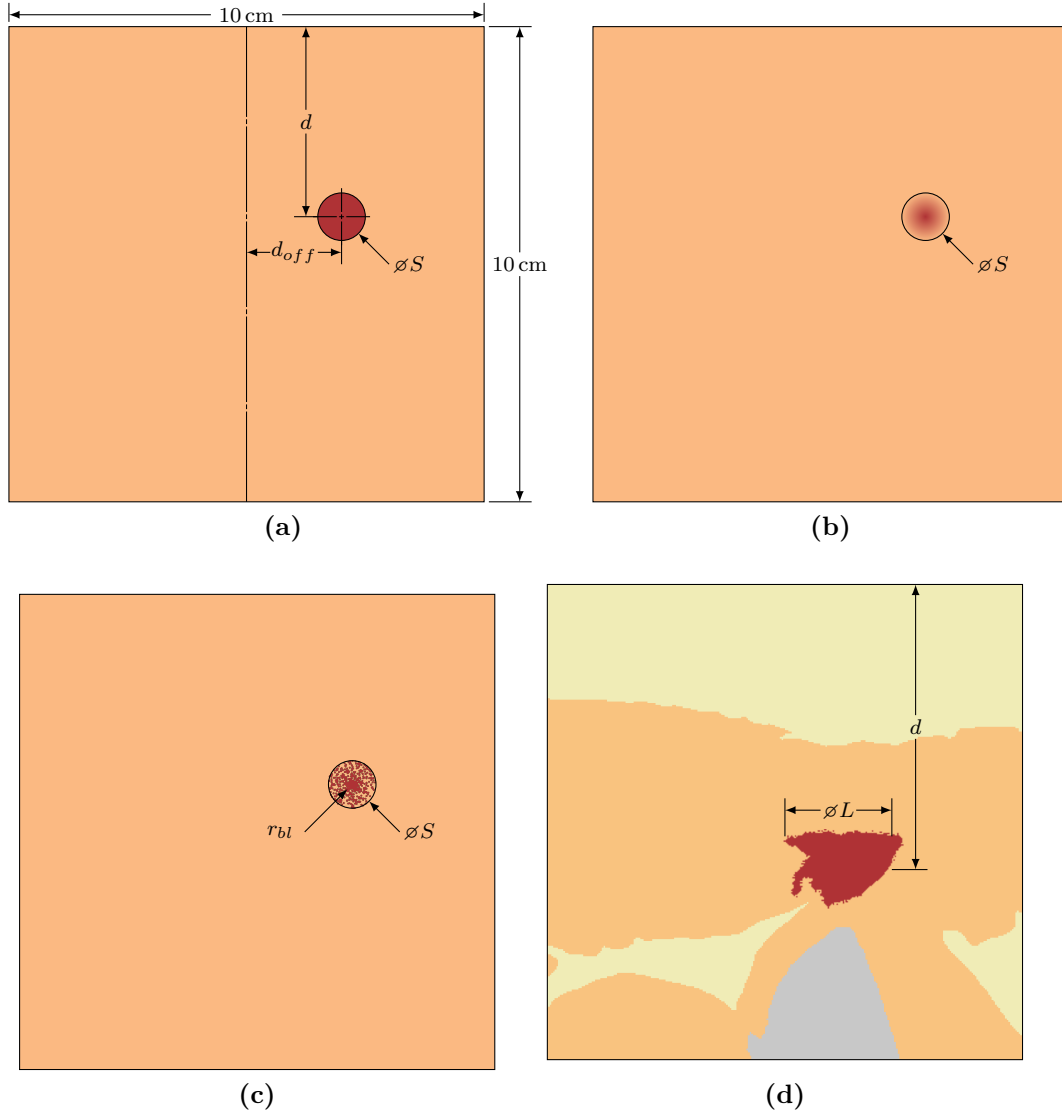


Fig. 5.1: Schematics of the lesion models that were investigated using shear wave speed quantification showing (a) a spherical hard-boundaried lesion, (b) a spherical blurred-boundary lesion, (c) a cluster of numerous small lesions composing a larger lesionous region, and (d) the geometry from an MRI-acquired deep tissue injury overlaid on a slice from the Visible Human Project such that the injury lesion was located immediately superior to an ischial tuberosity.

lies in the the data that was extracted and processed from the time-domain finite-element models of tissue displacement. A discussion of how shear wave speeds are tracked in the finite-element model of tissue deformation is given

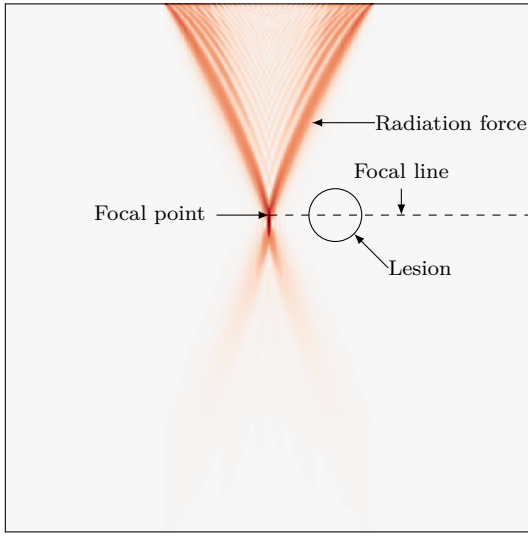


Fig. 5.2: A sample acoustic radiation force distribution shown with a schematic of the lesion's location and size in the simulated tissue domain. Note how the focal point is adjacent to the lesion, offset in this case by 1.25 cm. The focal line extends laterally from the focal point, through the lesion, to the edge of the tissue domain—this is the line that will be used to calculate shear wave speeds.

Lamé's second parameter for the lesion and tissue respectively, $c_{T,l}$ and $c_{T,t}$ are the shear wave speeds in the lesion and tissue respectively, and ρ is the density of the tissue and assumed to be constant between the lesion and tissue.

$$c_T = \sqrt{\frac{\mu}{\rho}} \quad (5.12a)$$

$$c_T^2 \rho = \mu \quad (5.12b)$$

$$E_{rel} = \frac{\mu_l}{\mu_t} = \left(\frac{c_{T,l}}{c_{T,t}} \right)^2 \quad (5.12c)$$

In order to determine the velocity of generated shear waves, the ARFI load-induced displacement of the soft tissue must be tracked through time along a line passing through the focal point radiating laterally outward in the finite-element model of tissue deformation. A sample result of tissue displacement

through time and along such a line is presented in Fig. 5.3 where the wave can be readily visualized through time, noting that the wave travels ever further from the centreline.

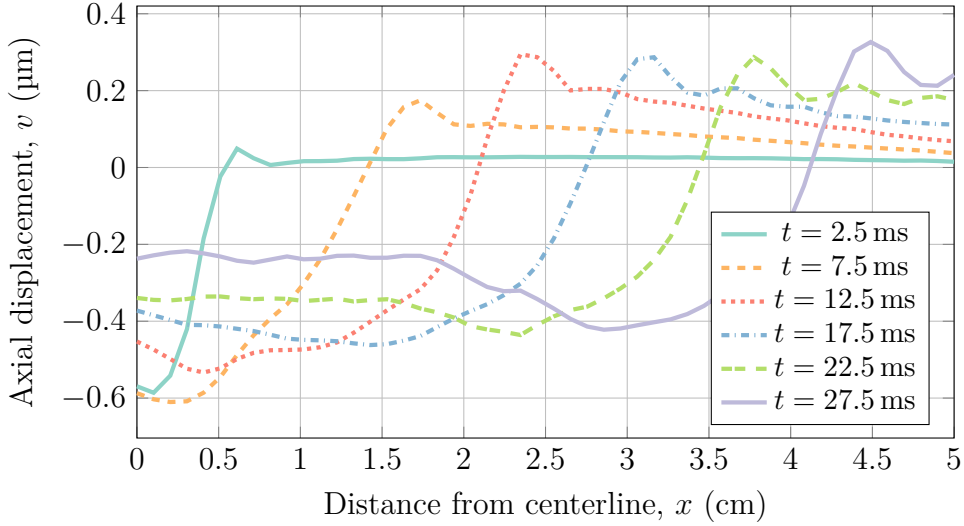


Fig. 5.3: Axial displacement induced by a shear wave traveling laterally across the focal line of an ARFI load. There is a stiff ($E_{rel} = 3.2$) lesion with a diameter of 1 cm located 1.25 cm away from the centerline, with both the focal line and the lesion located at a depth of 4 cm from the surface.

The results in Fig. 5.3 represent a finite subsample of the shear wave's propagation along the focal line. For a continuous representation of the shear wave propagation, the surface shown in Fig 5.4 may be constructed. In order to track the wave through both position and time, a contour line representing a constant displacement value may be extracted. For this work, a contour line representing the mean value of the displacement over the entire position-time domain was utilized and is portrayed in Fig. 5.5.

Fig. 5.6 represents the extracted contour line. This contour line now represents a position-time trace of the shear wave, from which the velocity of the wave may be calculated by differentiating the position of the wave with respect to time as per equation 5.13. Care must be taken when numerically

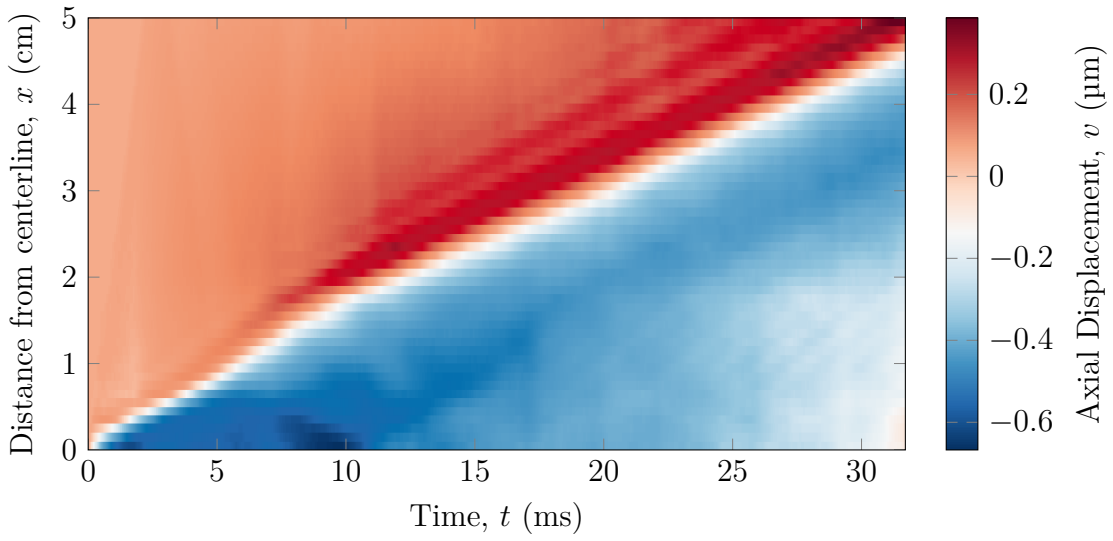


Fig. 5.4: Continuous surface plot of the shear wave induced axial displacement tracked through both time and distance from the transducer centreline. The sharp transition from negative to positive displacement marks the location of shear wave in time at any given location.

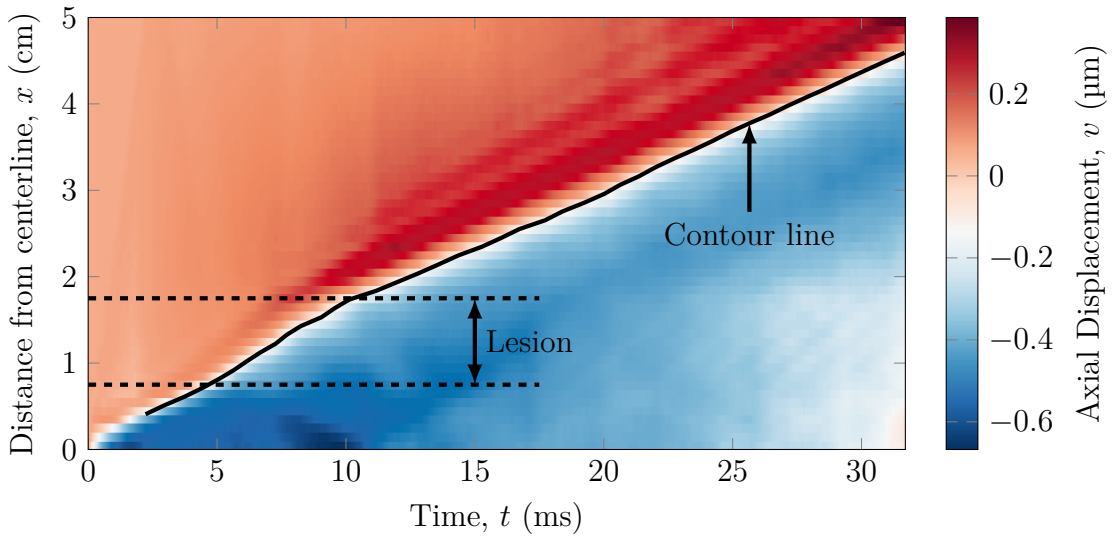


Fig. 5.5: Continuous surface plot of shear wave induced axial displacement highlighting a mean contour line representing the shear wave location as time progresses. By inspection, the slope of the contour line is greater within the lesionous region than outside of it, suggesting that the lesion is stiffer than the surrounding tissue.

differentiating, as numerical errors are greatly amplified by differentiation. To combat this, a moving window average filter with a kernel of 5 mm was applied

to the position-time curve before centre-difference differentiation was used to result in the shear wave speed graph given in Fig. 5.7. Sample source code used to extract and generate the shear wave speed plot is given in listing B.6 in Appendix B.

$$c_T = \frac{dx}{dt} \quad (5.13)$$

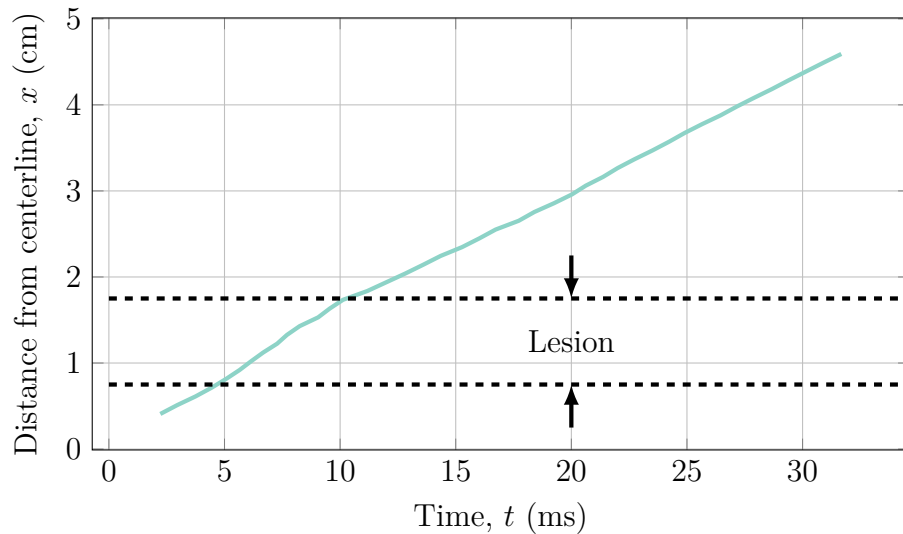


Fig. 5.6: The extracted shear wave position-time trace showing the location of the generated shear wave increases with time, albeit at different rates depending on the underlying tissue properties.

As is shown in Fig. 5.7, the speed of the shear wave within the lesion (which was in this case 3.2 times as stiff as the surrounding tissue) is substantially greater than the shear wave speed in the regular tissue. Note that instead of an impulse response at the boundaries of the lesion as might be expected, the shear wave speed reaches a peak value approximately halfway through the lesion, indicating that the wave requires some finite amount of time to both speed up and slow down within the lesion, suggesting that the technique may have difficulty identifying small lesions as the shear wave speed will not be

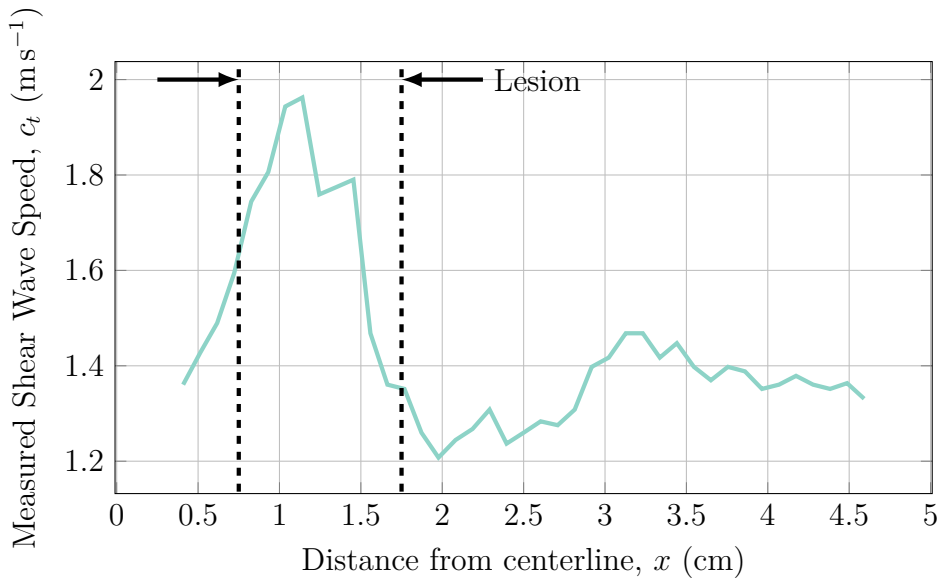


Fig. 5.7: Trace of the shear wave speed along the focal line through both lesionous and “healthy” tissue. The shear wave speed within the lesion is much greater than the shear wave speed through the “healthy” tissue, indicating that the lesion is significantly stiffer than the surrounding tissue. The shear wave speed was calculated as the numerical differentiation of the shear wave’s position through time.

able to fully adjust to the lesion in the time it takes for the wave to completely pass through the lesion.

5.3.3 Lesion Detection Characterization

In order to determine the detection sensitivity of shear wave speed quantification with respect to lesion size, hard-boundaried spherical lesions with varying radii were interrogated using ARFI loads while the speed of the shear waves developed along the focal line were monitored. The ARFI loads were applied using a probing frequency of 2 MHz for 150 μs with a source pressure of 3.35 MPa using an F-number of $f/1.0$. The lesions were located at a depth of 4 cm with an offset of 1.25 cm from the focal point of the ARFI load. The results of this characterization are given in Fig. 5.8. Lesions stiffness ratios

were measured by calculating the maximum or minimum shear wave speed within the lesion if the shear wave speed within the lesion was greater than or less than the surrounding tissue respectively and the mean shear wave speed without the lesion and applying equation 5.10.

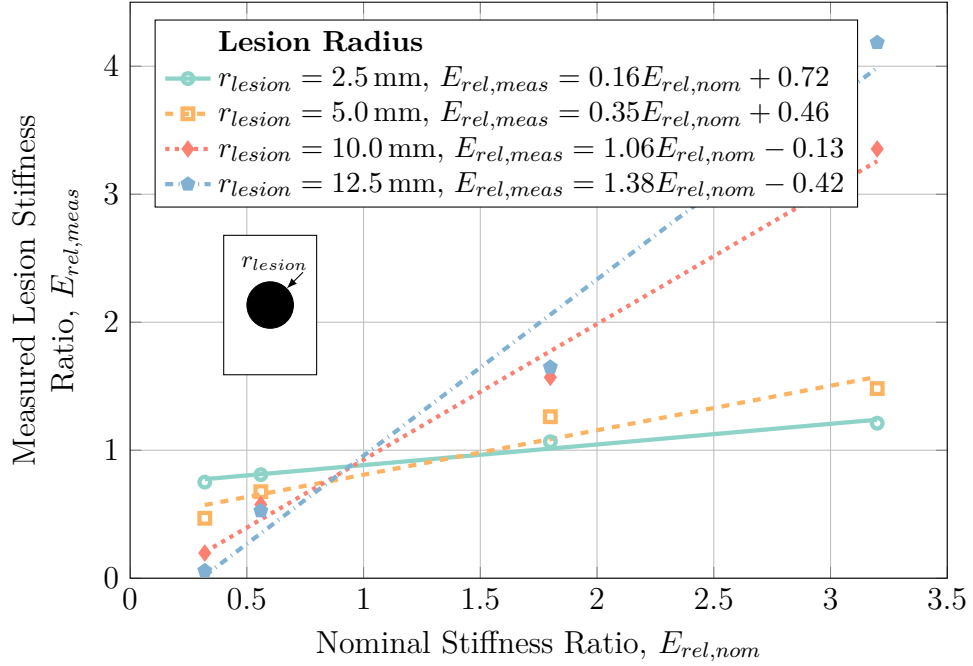


Fig. 5.8: Numerical characterization of the shear wave speed measured stiffness ratios acquired with varying lesion radii for a hard-boundaried lesion at a depth of 4 cm using an ARFI interrogation frequency of 2 MHz.

As can be seen in Fig. 5.8, small lesions with radii $\leq 5.0 \text{ mm}$ are nearly impossible to detect—large changes in the true lesion stiffness ratio represent very minute changes in the measured lesion stiffness ratio for these small lesions. Conversely, large lesions are much easier to detect, portraying a nearly one-to-one or better mapping between the true and measured lesion stiffness ratios. This suggests that the larger a lesion is, the more readily it may be detected while smaller lesions are more difficult to detect with a lower limit of the lesion radius approaching 5.0 mm.

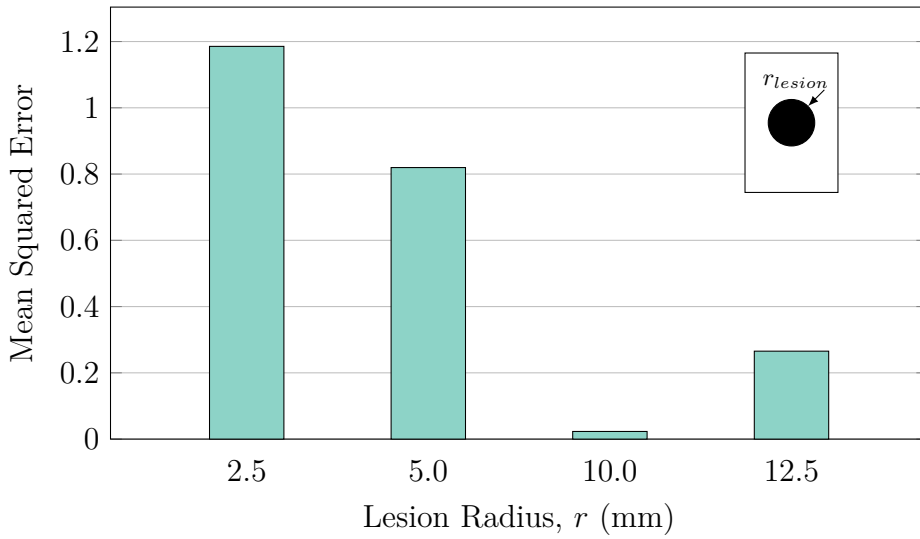


Fig. 5.9: Mean squared error between the true and measured lesion stiffness ratios for increasing lesion radii for a hard-boundaried lesion at a depth of 4 cm using an ARFI interrogation frequency of 2 MHz.

To further investigate these results, the mean-squared error associated with varying lesion size was calculated as per equation 4.17 with the results presented in Fig. 5.9. In Fig. 5.9, it is clear to see that the error associated with small lesions was significantly greater than with larger lesions. Interestingly, the largest lesions tested (with radii of 12.5 mm) presented greater error than lesions with radii of 10.0 mm. This increase in error may be largely attributed to the over-estimation of the lesion stiffness ratio for a stiff ($3.2 \times$ basal stiffness) lesion with a radius of 12.5 mm seen in Fig. 5.8.

One of the key parameters used in shear wave speed quantification is the distance between the focal point of the acoustic radiation force and the lesion itself. In order to adequately generate fully-formed shear waves within the lesion, the focal point of acoustic radiation force should be located adjacent to the lesion. As can be seen in Fig. 5.10, regardless of the lesion offset distance, shear wave speed quantification is able to differentiate lesions from the tissue

with reasonable accuracy. The largest exception to this generalization is for very stiff lesions for which the ARFI load is focused the farthest away from the lesion. It is hypothesized that the measured stiffness ratio of these lesions is underestimated because by the time the shear wave reaches the relatively far-away lesion, its energy has substantially dissipated, disallowing the wave to remain fully cohesive and speed up appropriately.

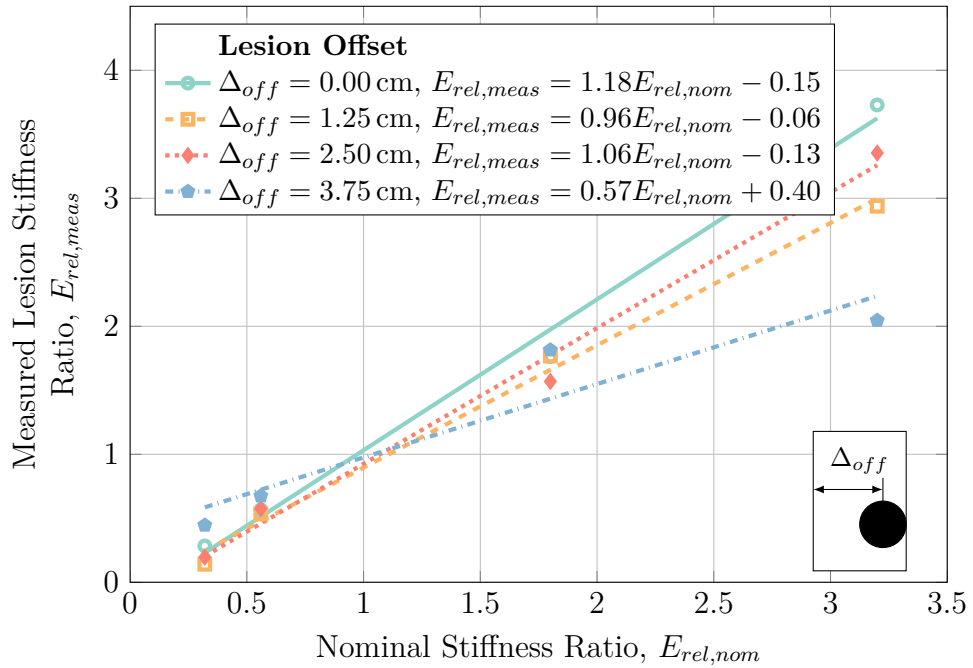


Fig. 5.10: Numerical characterization of the shear wave speed measured stiffness ratios acquired with varying lesion offsets for a hard-boundaried 0.5 cm radius lesion at a depth of 4 cm using an ARFI interrogation frequency of 2 MHz. The greatest error between the true and measured stiffness ratios occurred at the highest stiffness ratio of 3.2, with the large lesion offset underestimating the stiffness ratio and the negated lesion offset overestimating the stiffness ratio.

Fig. 5.11 portrays the mean squared error between the measured and true lesion stiffness ratios with increasing lesion offset distance. As Fig. 5.11 shows, a lesion offset of approximately 2.5 cm is ideal for quantifying lesion stiffness as it produces the least amount of error between the true and measured lesion

stiffness ratios which confirms the notion that the shear wave needs some time to become fully developed as it travels through the tissue. Since the error between lesion offsets of 1.25 cm and 2.50 cm is nearly negligible, it is likely that the wave is able to become fully developed even earlier than 2.50 cm and lesion offsets as small as 1.25 cm may be used. The relatively large error present for the largest lesion offset of 3.75 cm is largely due to the severe underestimation of the lesion stiffness for the stiffest lesion seen in Fig. 5.10.

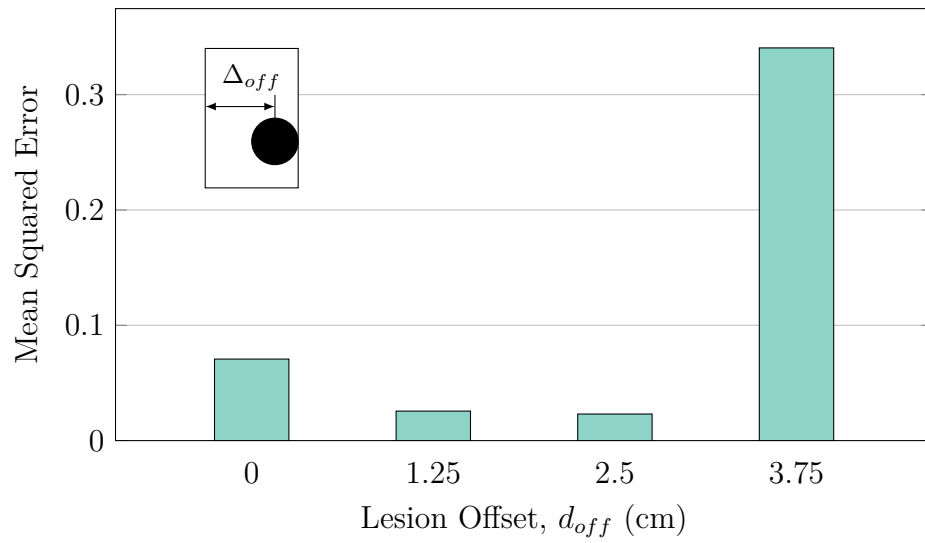


Fig. 5.11: Mean squared error between the true and measured lesion stiffness ratios for increasing lesion offsets for a hard-boundaried 0.5 cm radius lesion at a depth of 4 cm using an ARFI interrogation frequency of 2 MHz.

Another key parameter relating to the detection of deep tissue injury lesions relates to the depth that the lesions may actually be detected—for example, in people with large amounts of body fat or muscle, the distance between the surface of the skin and the boney prominence where lesions are most likely to form may be very large compared to someone with very little amounts of body fat or muscle. In order to study the effect of lesion depth on the detection sensitivity of shear wave speed quantification, simulated lesions were placed at

various depths ranging from 2 cm – 8 cm below the surface of the skin with the measured stiffness ratios for these lesions calculated and shown in Fig. 5.12.

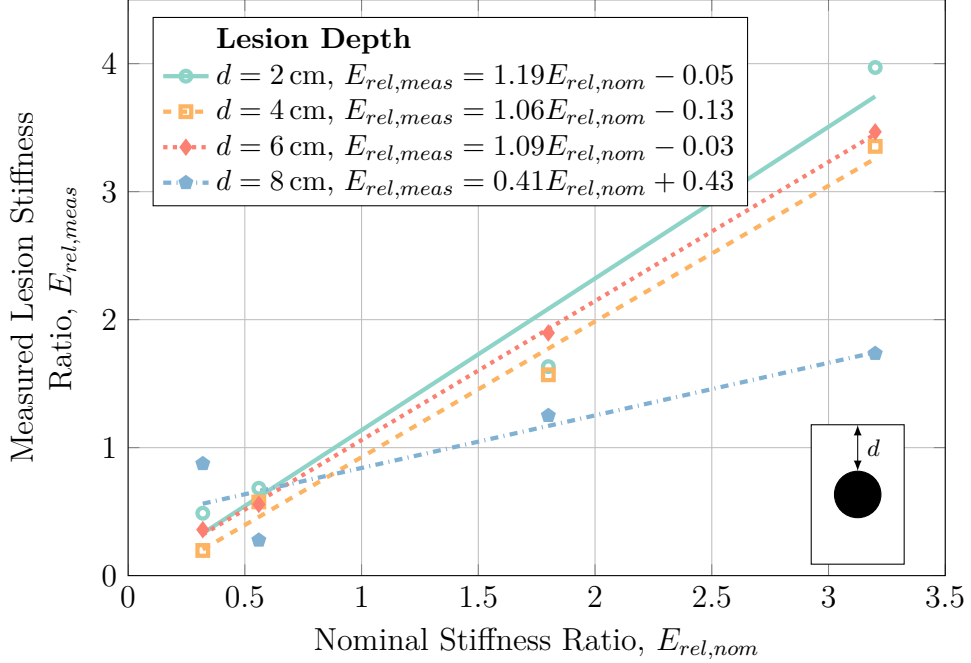


Fig. 5.12: Numerical characterization of the shear wave speed measured stiffness ratios acquired with varying lesion and focal point depths for a hard-boundaried 0.5 cm radius lesion with an offset of 2.50 cm using an ARFI interrogation frequency of 2 MHz.

As Fig. 5.12 shows, there is little dependence of shear wave speed quantifications detection sensitivity for shallow to medium-depth lesions—lesions placed at a depth of 2 cm – 6 cm presented approximately equal detection curves. Of note in Fig. 5.12 is that deep lesions—lesions at a depth of 8 cm or more—are difficult to detect as the method is not very sensitive to these deeper lesions—both underestimating the stiffness of deep stiff lesions and overestimating the stiffness of deep unstiff lesions. The large error involved with attempting to measure the stiffness of deep lesions can be seen in Fig. 5.13 where the mean squared error for the various depths examined was calculated. In Fig. 5.13, the 8 cm deep lesions present a significantly greater amount

of error than their shallower counterparts. Also of note is that the shallowest lesions investigated—lesions at a depth of 2 cm—presented with greater error than the mid-depth lesions. The source of this error largely lies in the over-estimation of the stiff lesion stiffness seen in Fig. 5.12 which may be due to numerical errors in the models and calculations.

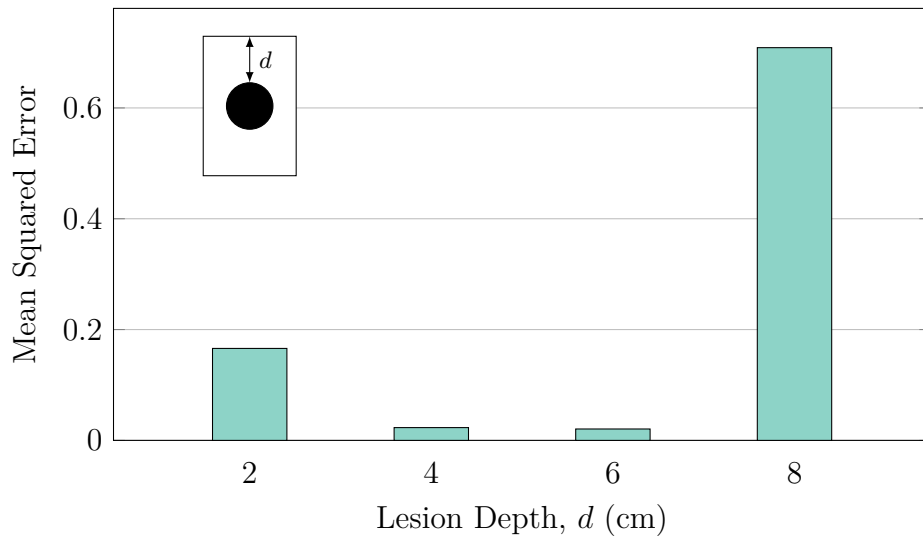


Fig. 5.13: Mean squared error between the true and measured lesion stiffness ratios for increasing lesion depths for a hard-boundaried 0.5 cm radius lesion with an offset of 2.50 cm using an ARFI interrogation frequency of 2 MHz.

Since deep tissue injury lesions are unlikely to be perfectly round and hard-boundaried, three different models of lesion geometry were investigated—namely, lesions with blurred boundaries that “fade” into the surrounding tissue, clusters of small lesions that together make up a larger lesions region, and a lesion with MRI-acquired geometry [67] embedded in geometry obtained from a Visible Human slice [126]. Although the spherical hard-boundaried lesions may not represent all the intricacies of real deep tissue injuries, the general trends that result from analysing them may improve the general understanding of lesion detection behaviour.

In order to investigate the effect of blurring lesions into the background tissue, hard-boundaried spherical lesions were blurred with varying blur radii as described in Section 5.2.2. The results of this characterization are presented in Fig. 5.14. As can be seen in Fig. 5.14, the effect of blur radii on lesion detection ability is negligible as noted by how the detection curves of the lesions with varying blur radii are largely coincident.

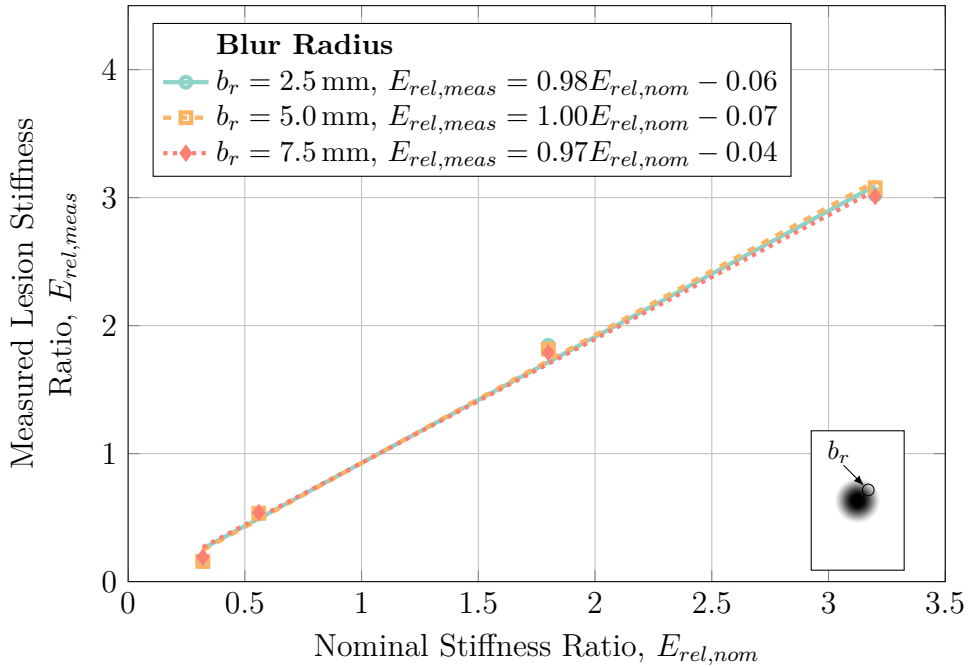


Fig. 5.14: Numerical characterization of the shear wave speed measured stiffness ratios acquired with varying lesion and focal point depths for a blurred 1.0 cm radius lesion with an offset of 1.25 cm at a depth of 4 cm using an ARFI interrogation frequency of 2 MHz.

This lack of reliance of detection sensitivity on blur radius is further portrayed by the mean squared error of the results, calculated in Fig. 5.15. While there are some minor differences in the error between the various blur radii—chiefly between blur radii of 2.5 mm and 5.0 mm—the scale of these differences lie within the range of numerical error and noise and so are not significant.

The fact that detection sensitivity does not decrease with increasing blur

radii in shear wave speed quantification makes shear wave speed quantification a desirable tool for detecting deep tissue injury lesions as it means that even imperfect, newly-forming lesions can still be readily detected and monitored.

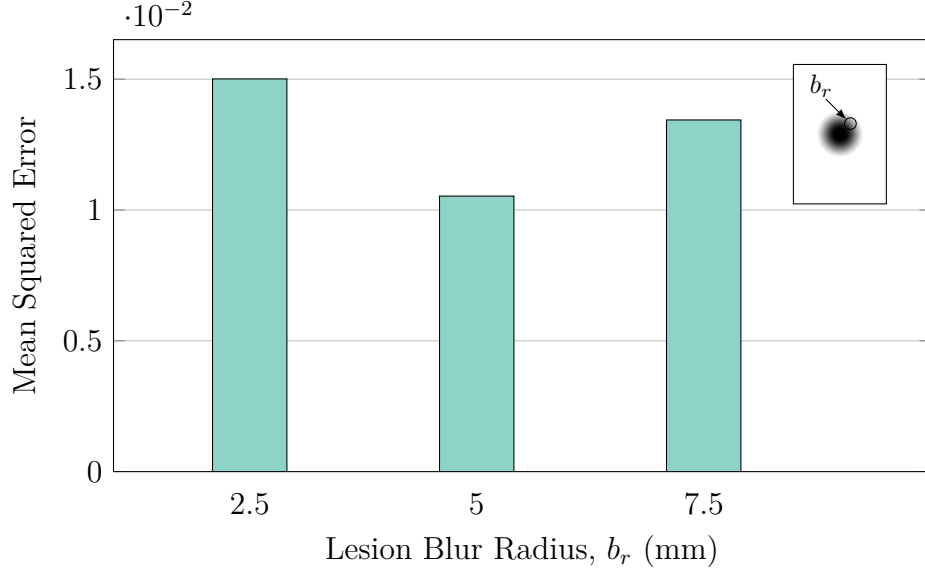


Fig. 5.15: Mean squared error between the true and measured lesion stiffness ratios for increasing lesion depths for a blurred 1.0 cm radius lesion with an offset of 1.25 cm at a depth of 4 cm using an ARFI interrogation frequency of 2 MHz.

Beyond having boundaries that “fade” into the background tissue, deep tissue injury lesions may in fact be heterogeneous in nature with a large number of small lesions clustered together to form a larger lesionous region. To investigate this phenomenon, the effect of small clustered lesion density and individual radii were investigated using shear wave speed quantification. The effect of clustered lesion density was investigated as outlined in Section 5.2.2, the results of which are shown in Fig. 5.16.

As Fig. 5.16 shows, decreasing the cluster density generally results in a decreasing detection sensitivity with the least dense clusters both underestimating the stiffness of stiff lesions and overestimating the stiffness of unstiff lesions. This behaviour is somewhat expected—as the density of clustered le-

sions decreases, so too does the mean true stiffness of the lesionous region that is inspected due to the greater ratio of “healthy” tissue to lesionous tissue.

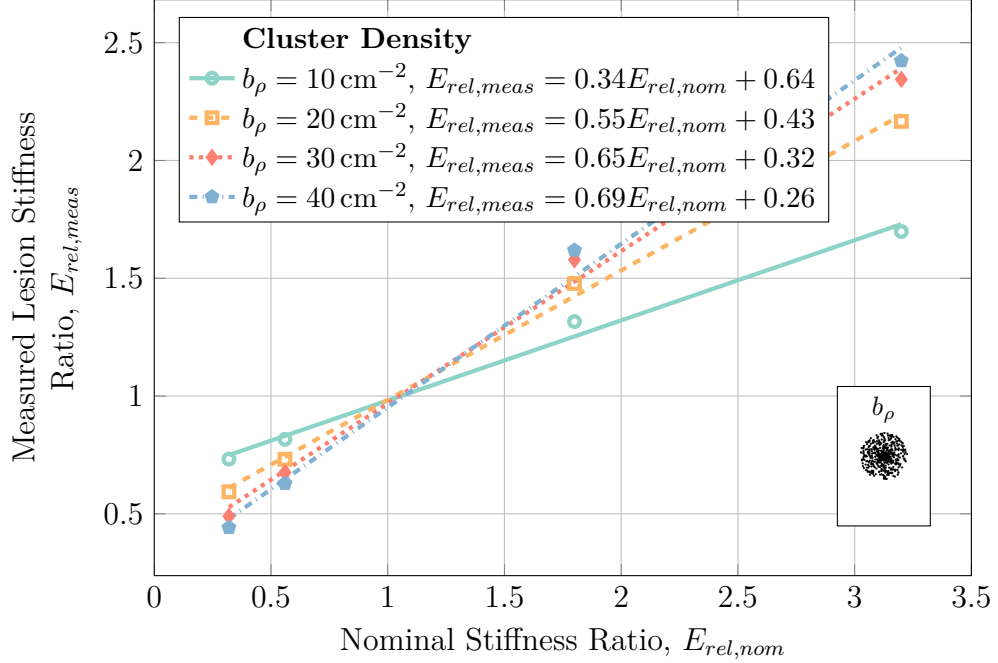


Fig. 5.16: Numerical characterization of the shear wave speed measured stiffness ratios acquired with varying cluster densities for clustered 1 mm radius lesions within a 1.0 cm radius with an offset of 1.25 cm at a depth of 4 cm using an ARFI interrogation frequency of 2 MHz.

This generalization is further portrayed by the mean squared error which is shown in Fig. 5.17. In Fig. 5.17, increasing cluster density results in monotonically decreasing error.

Beyond the cluster density, the size of individual clustered lesions within the lesionous region may affect the detection sensitivity. To investigate this parameter, the radii of the individual lesions in the clustered lesion model were varied, with the results presented in Fig. 5.18. Fig. 5.18 shows how decreasing the individual clustered lesion radii results in decreases in the detection sensitivity. This is similar to the results presented in Fig. 5.16 in that decreasing the individual lesion radii results in a decrease of the ratio between lesionous

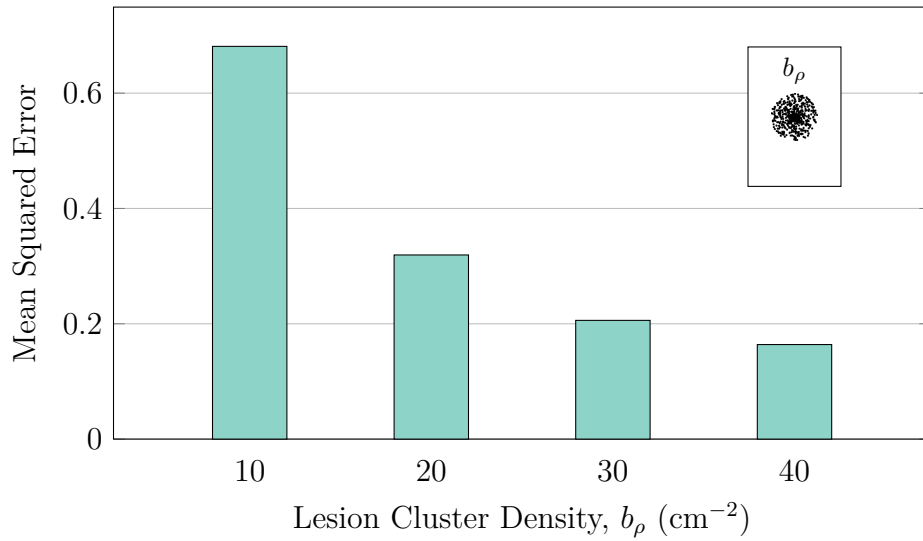


Fig. 5.17: Mean squared error between the true and measured lesion stiffness ratios for increasing lesion cluster density for clustered 1 mm radius lesions within a 1.0 cm radius with an offset of 1.25 cm at a depth of 4 cm using an ARFI interrogation frequency of 2 MHz.

tissue and healthy tissue within the lesionous region—the greater the proportion of lesionous tissue within the investigated region, the more accurate the detection of the lesionous region.

Again, this conclusion is corroborated by the mean squared error shown in Fig. 5.19. In Fig. 5.19, increasing the individual lesion radii results in a significant decrease in the stiffness measurement error in the lesionous region.

Finally, in order to place these characterizations within the context of a real deep tissue injury situated within the geometry of a real human soft tissue domain, a numerical characterization of lesion size in the Visible Human lesion model outlined in Section 5.2.2 was carried out with the results portrayed in Fig. 5.20. Fig. 5.20 relates the change in detection sensitivity with different sized lesions and shows that small lesions (with “radii” ≤ 5.0 mm) are extremely difficult to detect as the stiffness of small stiff lesions is severely un-

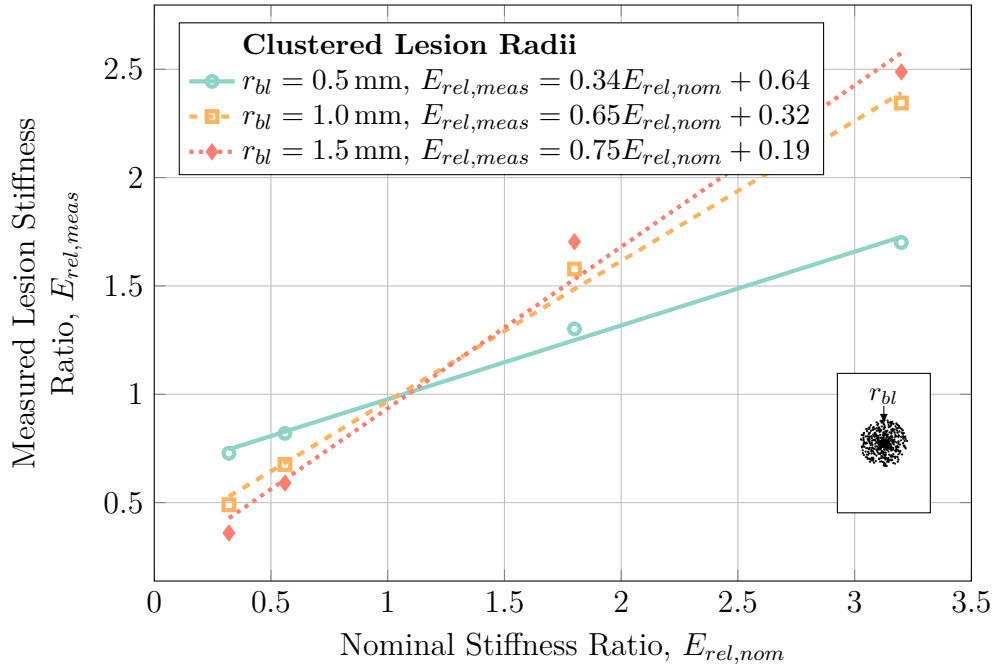


Fig. 5.18: Numerical characterization of the shear wave speed measured stiffness ratios acquired with varying clustered lesion radii for clustered lesions with a density of 30 cm^{-2} within a 1.0 cm radius with an offset of 1.25 cm at a depth of 4 cm using an ARFI interrogation frequency of 2 MHz .

derestimated and the stiffness of small unstiff lesions is severely overestimated. These results align with what was seen in the spherical hard-boundaried lesion case presented in Fig. 5.8, indicating that the simplified spherical results generally hold true for the more complex geometry results.

As expected from the results in Fig. 5.20, increasing the lesion radius results in monotonically decreasing measurement error as is shown in Fig. 5.21 with the least amount of measurement error present for the largest lesions. This means that relatively larger lesions will be easier to detect and accurately quantify and may be due to the shear wave requiring some finite period of time to speed up or slow down with a lesionous region of tissue as discussed previously.

Numerical values for the characterization plots presented here are given in

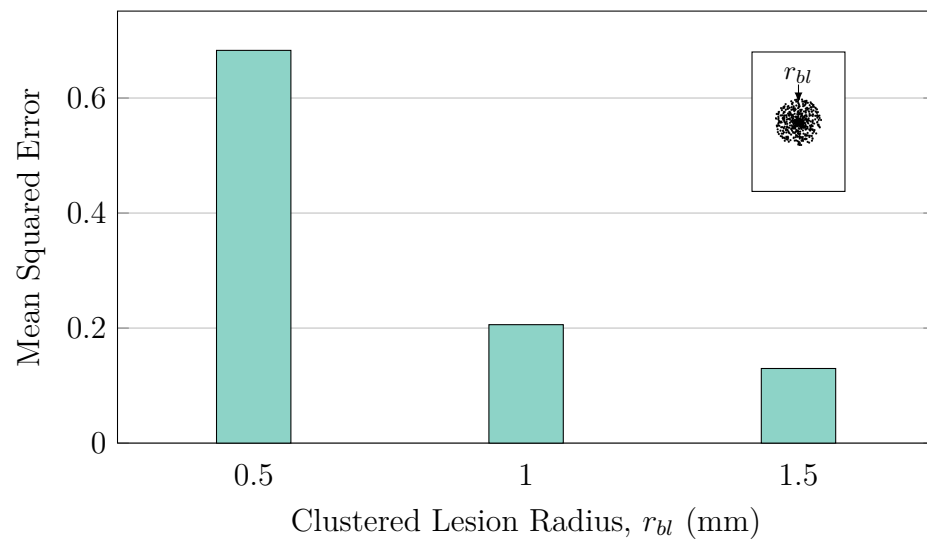


Fig. 5.19: Mean squared error between the true and measured lesion stiffness ratios for increasing clustered lesion radii for clustered lesions with a density of 30 cm^{-2} within a 1.0 cm radius with an offset of 1.25 cm at a depth of 4 cm using an ARFI interrogation frequency of 2 MHz .

Section A.3 of Appendix A.

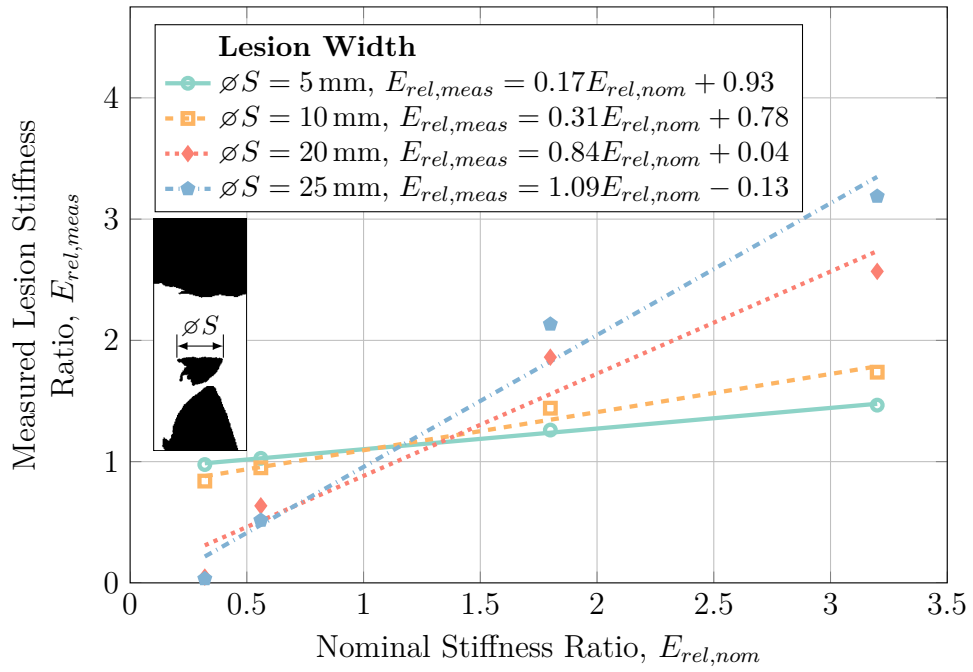


Fig. 5.20: Numerical characterization of shear wave speed measured stiffness ratio with changing lesion radii for MRI-acquired lesion geometry in a Visible Human model with an offset of 1.25 cm at a depth of 6 cm using an ARFI interrogation frequency of 2 MHz.

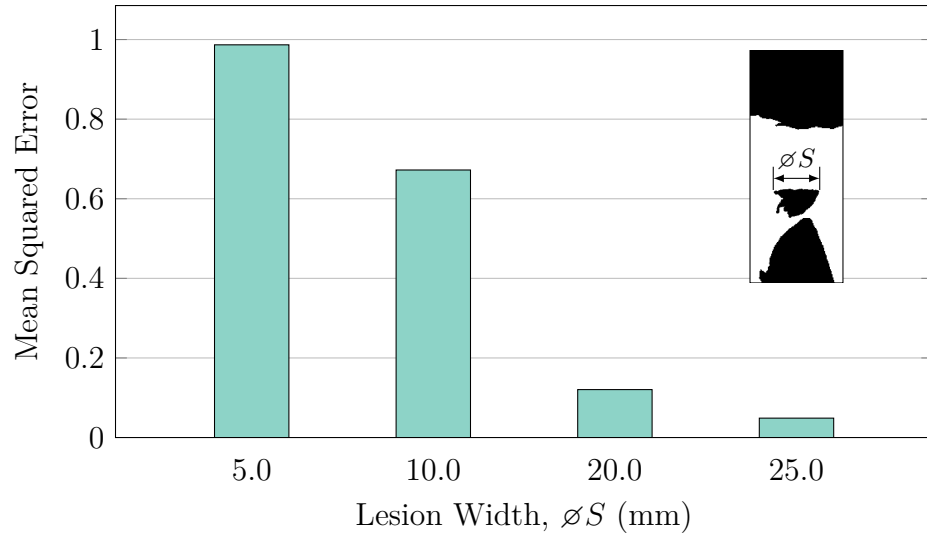


Fig. 5.21: Mean squared error between the true and measured lesion stiffness ratios for increasing lesion radii for MRI-acquired lesion geometry in a Visible Human model with an offset of 1.25 cm at a depth of 6 cm using an ARFI interrogation frequency of 2 MHz.

5.3.4 Physical Phantom Validation

In order to examine the validity of the simulations presented in Section 5.2.2 and the results presented in Section 5.3, experiments using a physical tissue mimicking phantom and an ultrasound machine were performed as described in Section 5.2.3. The results of these experiments are presented in Figs. 5.22 and 5.23 where the difference between the experimentally measured stiffness ratios of lesions were compared against their nominal and simulated stiffnesses respectively.

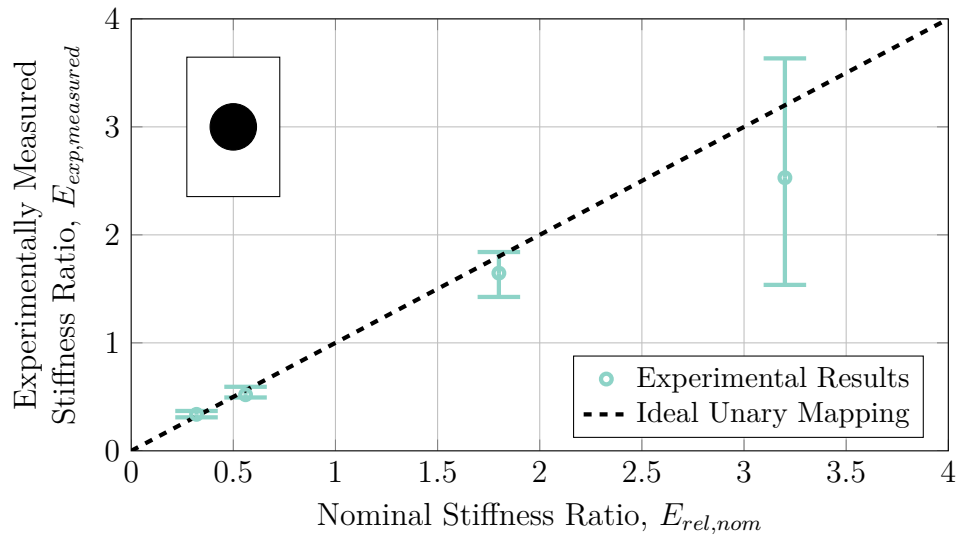


Fig. 5.22: Relation between nominally reported strain ratios of the tissue mimicking phantom and experimentally measured strain ratios for a lesion at a depth of 3.5 cm and diameter of 2.0 cm showing general agreement between simulated and experimental cases. Error bars represent the range of measurements acquired.

Fig. 5.22 shows the general agreement between the nominal and experimentally acquired lesion stiffness ratios. Of note is the increasing amount of measurement error associated with increasing nominal stiffness ratios and reflects the general underestimation of stiff lesion stiffness that was seen in the characterization of nearly all stiff lesions in Section 5.3. Further, the relatively

large degree of error was due to the measurement of the shear wave speed within the lesion rather than variability in the shear wave speed of the surrounding tissue. Nonetheless, the experimentally-acquired values lay within error of the expected nominal stiffness ratios, so the experiment was considered to produce acceptable results to compare against the simulations. The results of this comparison are shown in Fig. 5.23 where the stiffness ratios acquired through simulation are compared against experimentally-acquired stiffness ratios of parametrically identical lesions.

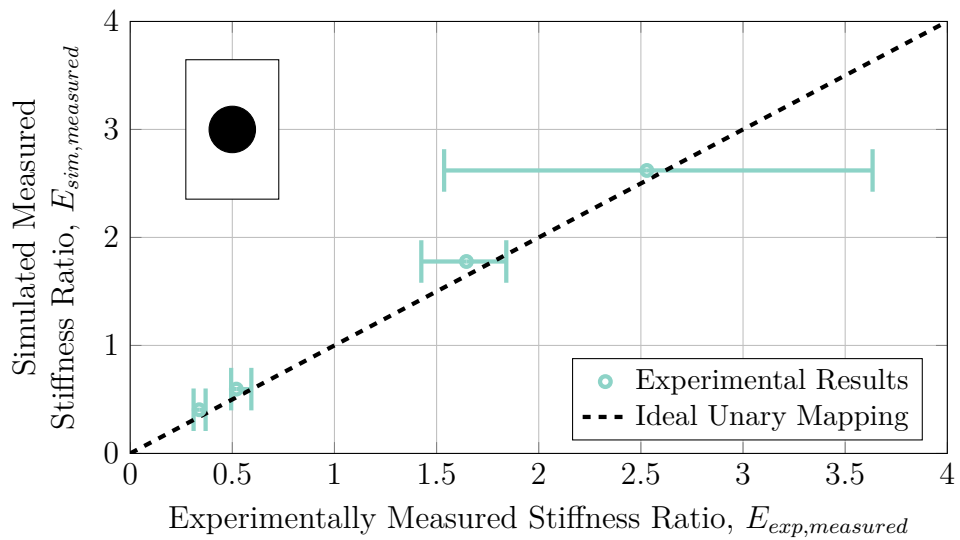


Fig. 5.23: Relation between simulated measured strain ratios and experimental measured strain ratios for a lesion at a depth of 3.5 cm and diameter of 2.0 cm showing general agreement between simulated and experimental cases.

As expected, there is nearly a one-to-one correspondence between the experimentally measured lesion stiffness ratios and the simulated lesion stiffness ratios for the various lesions investigated. In all of the lesion cases studied, the simulated lesion stiffness ratio was slightly greater than the experimentally measured stiffness ratio. This suggests that the simulated models introduce a minor bias in the results, although as the correlation is linear this may be

sions represent the most “basic” and general case used to investigate overarching lesion parameters such as overall size of the lesion and the depth at which it is placed. In order to compare the investigated modalities, a cross-section of the data centred around a lesion with radius of 10 mm at a depth of 4 cm is shown in Fig. 6.1. In Fig. 6.1, it is clear to see that shear wave speed quantification is by far the most accurate of the three detection modalities with its characterization curve representing an almost ideal one-to-one mapping of measured stiffness to true stiffness. Quasi-static elastography and ARFI imaging resulted in less detection sensitivity and were not substantially different from each other.

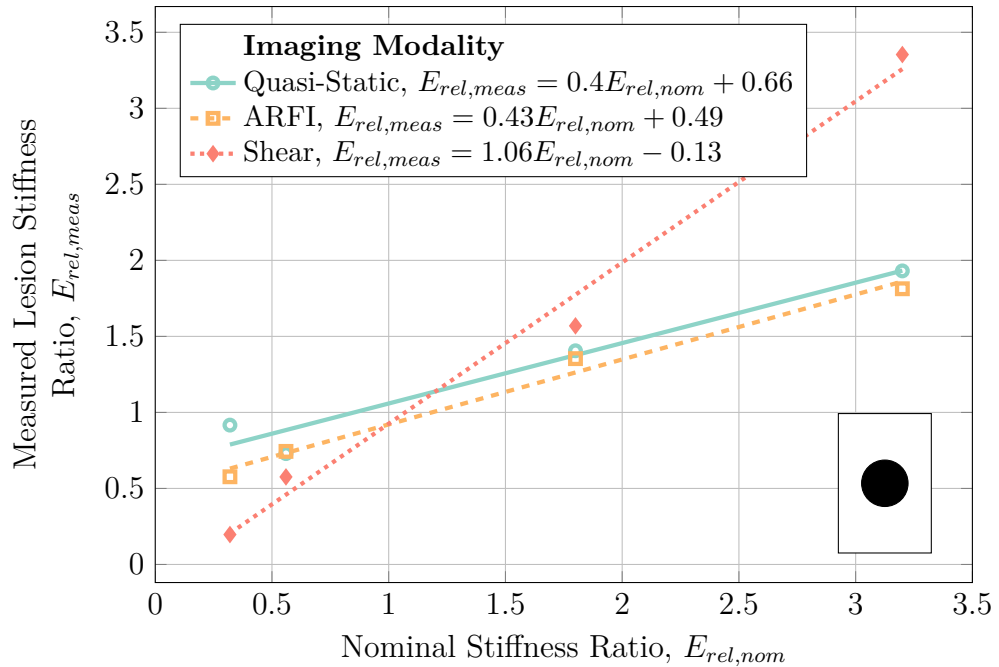


Fig. 6.1: Detection sensitivities of hard-boundaried spherical lesions with radii of 10 mm at a depth of 4 cm using quasi-static elastography, ARFI imaging, and shear wave speed quantification.

To further examine the error introduced by the various detection modalities, the percent difference between the expected true values of lesion stiffness

and the measured lesion stiffness for the results seen in Fig. 6.1 are shown in Fig. 6.2. Fig. 6.2 shows that across all lesion stiffnesses, shear wave speed quantification results in the least amount of error between the true and measured lesion stiffness. Errors across all the modalities were greatest for the least stiff lesions—those with stiffness ratios of 0.32. Errors involved with ARFI imaging were slightly greater than for quasi-static imaging across the remaining investigated stiffness ratios. It is likely however that the slight increase in error associated with ARFI imaging may be worth the added benefit of increased reliability and repeatability. Beyond this, shear wave speed quantification is certainly recommended for detecting lesions if at all possible not only due to its nature of fully quantifying tissue stiffness rather than simply estimating it but also due to its superior accuracy over quasi-static elastography and ARFI imaging.

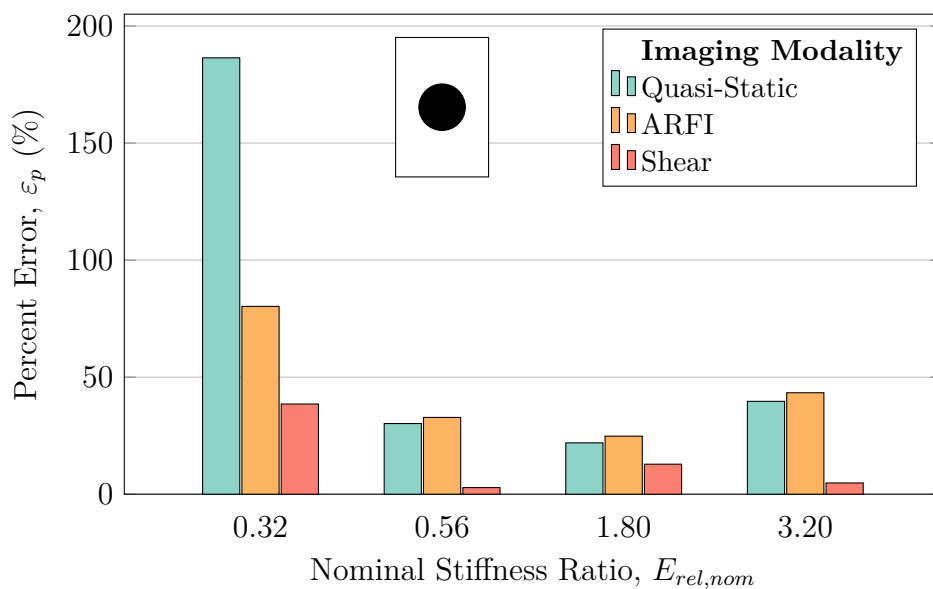


Fig. 6.2: Percent error of measured stiffness ratios for spherical lesions with radii of 10 mm at a depth of 4 cm across the three investigated modalities.

Since it is highly unlikely that real-world lesions will present as perfectly

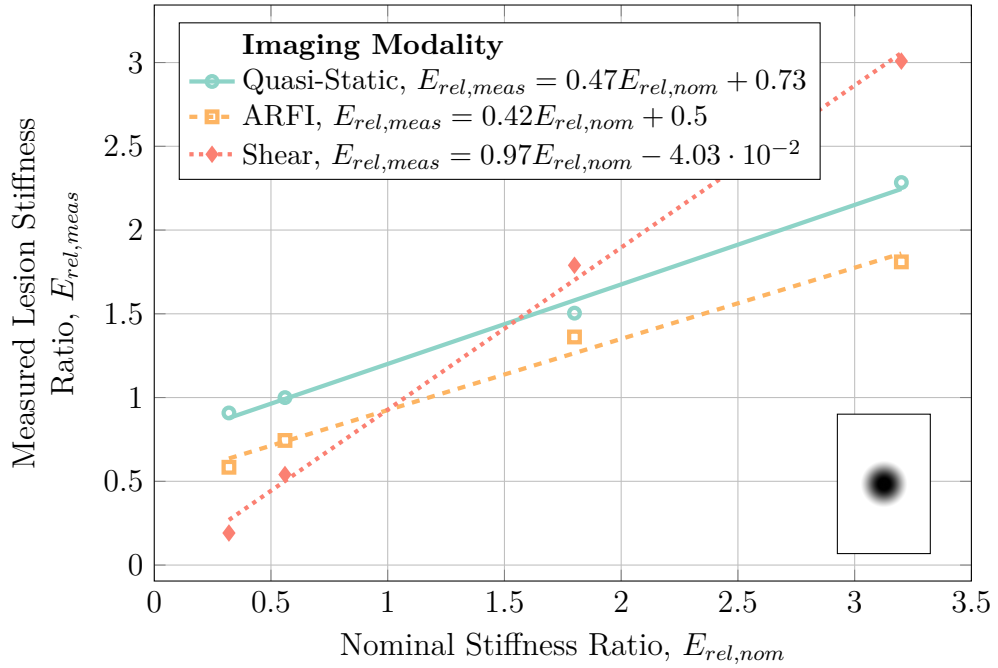


Fig. 6.3: Detection sensitivities of blurred-boundary spherical lesions with radii of 10 mm with blur radii of 7.5 mm using quasi-static elastography, ARFI imaging, and shear wave speed quantification.

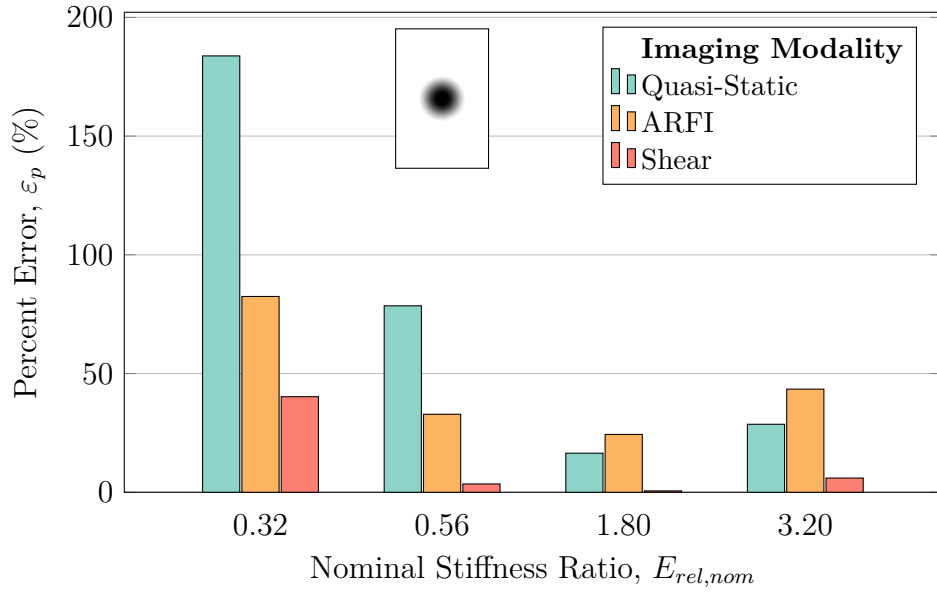


Fig. 6.4: Percent error of measured stiffness ratios for blurred lesions with radii of 10 mm and blur radii of 7.5 mm across the three investigated modalities.

injured tissue, a model comprising numerous small lesions clustered together to form a greater lesionous region was developed. Fig. 6.5 shows a cross-section of the characterization curves for this model when small lesions with radii of 1 mm were clustered with a density of 20 cm^{-2} . Although none of the investigated modalities were able to distinguish individual lesions in the various cluster models, all were able to differentiate the lesionous region as a whole. Once again, shear wave speed quantification proved to be the most accurate method with its characterization curves coming the closest to a one-to-one mapping of true to measured stiffnesses. Of note in this case, however, is that even shear wave speed quantification was still substantially less sensitive to lesions than an ideal case—all investigated modalities both over-estimated the stiffness of unstiff lesions and under-estimated the stiffness of stiff lesions.

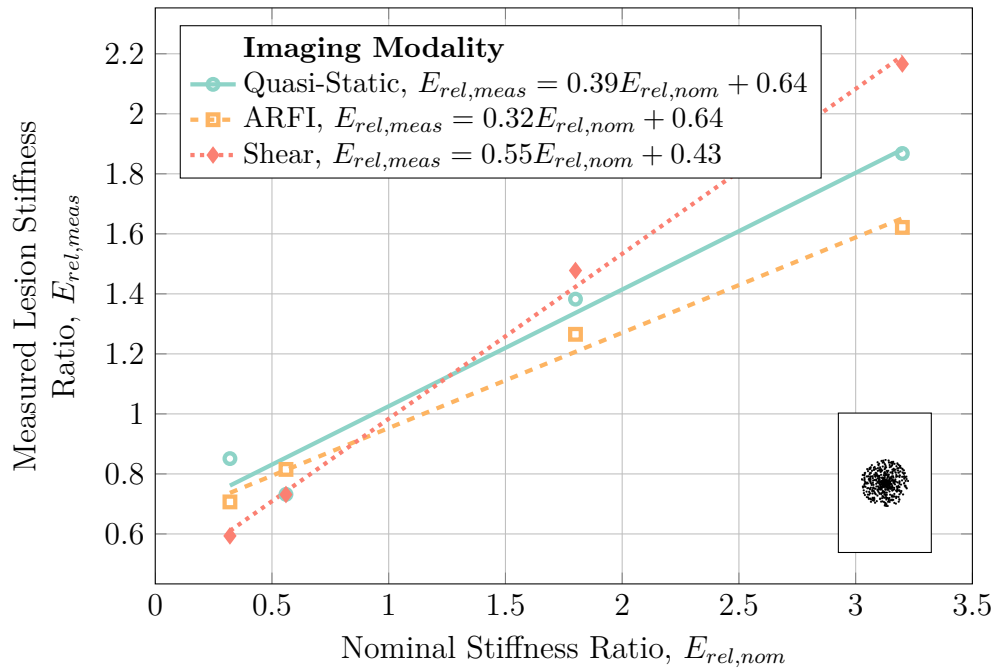


Fig. 6.5: Detection sensitivities of clustered lesions with a cluster density of 20 cm^{-2} and individual radii of 1 mm using quasi-static elastography, ARFI imaging, and shear wave speed quantification.

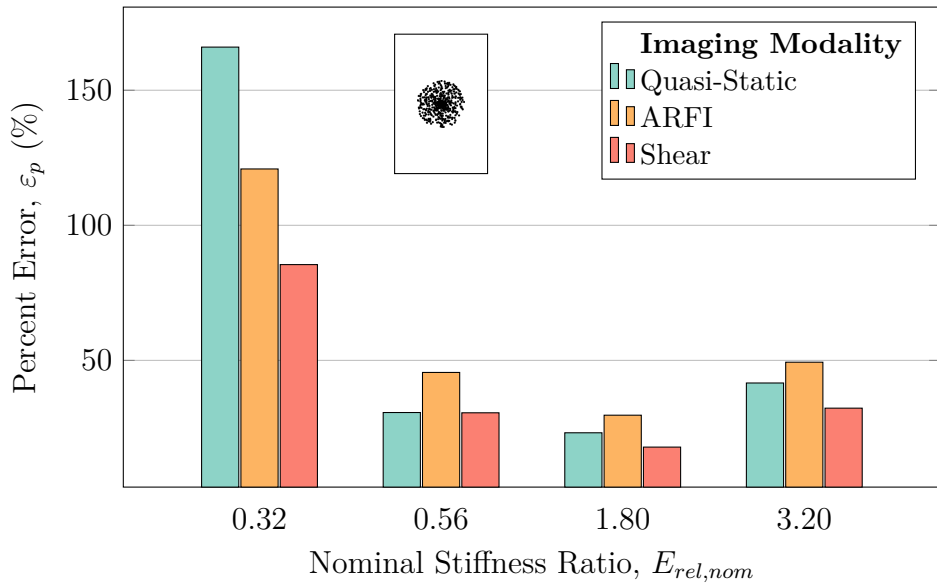


Fig. 6.6: Percent error of measured stiffness ratios for clustered lesions with a cluster density of 20 cm^{-2} and individual radii of 1 mm across the three investigated modalities.

superior to the ischial tuberosity—a boney prominence often associated with deep tissue injuries. As Fig. 6.7 shows, shear wave speed quantification once again presented the most ideal detection sensitivity of the three modalities. Both quasi-static elastography and ARFI imaging were much less sensitive to lesions in this model, with unstiff lesions being almost impossible to detect using quasi-static elastography. A key differentiation in this Visible Human model from the hard-boundaried spherical model studied previously is that shear wave speed quantification grossly underestimated the stiffness of both the least stiff and stiffest lesions examined.

As Fig. 6.8 shows, the error for shear wave speed quantification is much greater for both very unstiff ($E_{rel,nom} = 0.32$) and very stiff ($E_{rel,nom} = 3.20$) lesions—the error for unstiff lesions even surpasses that of ARFI imaging for the first time. For all other nominal stiffness ratios, shear wave speed quan-

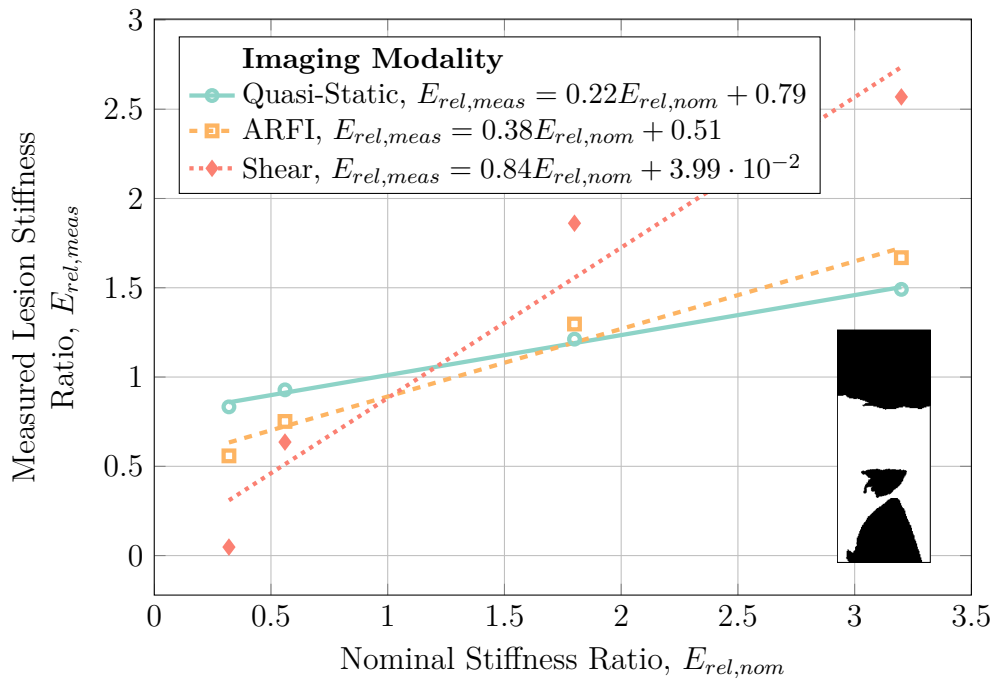


Fig. 6.7: Detection sensitivities of MRI-acquired Visible Human lesions with a width of 20 mm at a depth of 6 cm using quasi-static elastography, ARFI imaging, and shear wave speed quantification.

tification once again outperformed both quasi-static elastography and ARFI imaging. Although the use of more complicated geometry in the Visible Human project decreased the accuracy of shear wave speed quantification, it was once again the most sensitive and accurate of the investigated imaging modalities, suggesting it be used for quantifying deep tissue injuries if at all possible.

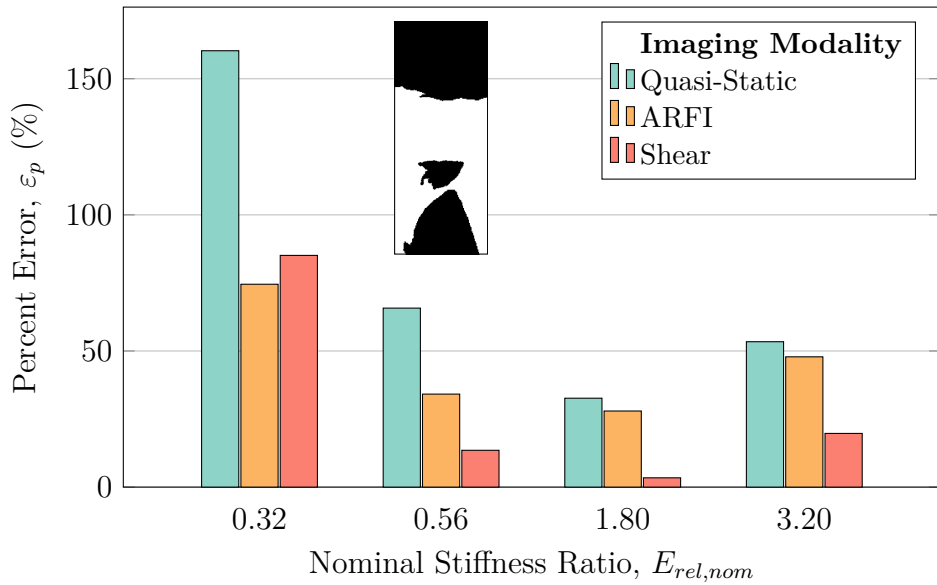


Fig. 6.8: Percent error of measured stiffness ratios for MRI-acquired Visible Human lesions with a width of 20 mm at a depth of 6 cm across the three investigated modalities.

Experimental Validations

In the experiments that were performed with each of the three elastography modalities on a tissue mimicking phantom, all three methodologies were able to distinguish both hard and unstiff lesions with some degree of accuracy. However, the stiffest lesions that were examined—those with a nominal stiffness ratio of 3.2—presented the greatest error and variation in the results as seen in Fig. 6.9. In these experiments, both ARFI imaging and shear wave speed quantification score similarly, although the variation in the shear results was much greater than the variation in the ARFI experiments. Both ARFI imaging and shear wave speed quantification showed relatively similar detection sensitivities with the major difference between the two being that ARFI imaging consistently over-estimated lesion stiffness as compared to shear wave speed quantification. Shear wave speed quantification was found to be the most accu-

rate for unstiff lesions, while ARFI imaging performed marginally better with stiff lesions. Quasi-static elastography generally displayed the worst results, echoing what was seen in Section 6.1.

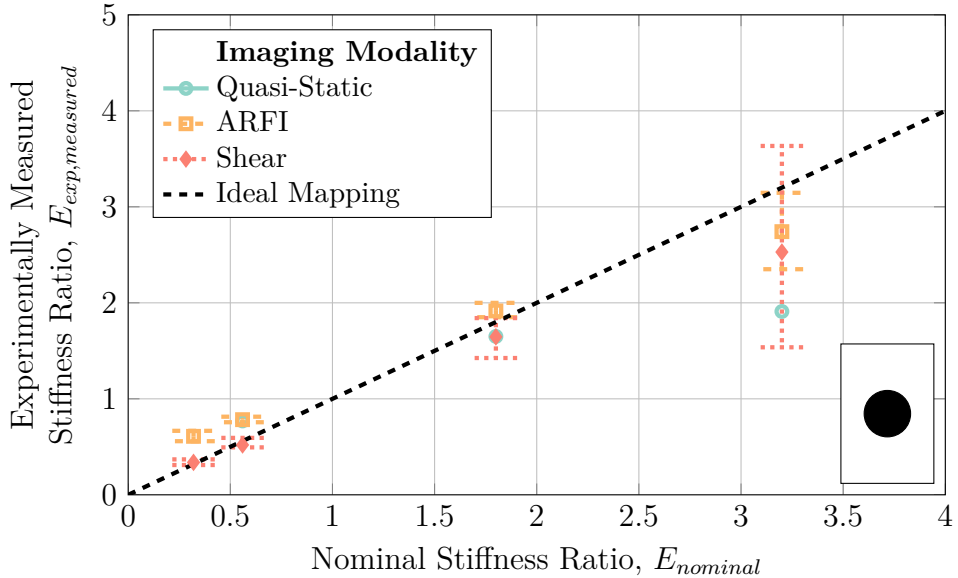


Fig. 6.9: Experimental results of the three methodologies investigated. ARFI imaging consistently overestimated the stiffness of the lesion compared to both quasi-static and shear wave speed quantification, which generally underestimated the stiffness of lesions.

By comparing the simulated results presented throughout this work to the parametrically identical results obtained through experiment, the accuracy of the simulations apart from the overall accuracy of the technique may be determined. These results are compared in Fig. 6.10 which shows a general agreement between experimentally measured stiffness ratios and their simulated counterparts for all but stiff ARFI imaging-acquired lesions. Since the simulation results for quasi-static elastography and shear wave speed quantification fall within error of their experimental counterparts, these simulation paradigms may be deemed acceptable. Counter to this, the simulation-acquired stiffness ratios in ARFI imaging fall well below their experimental values, suggesting

that the current ARFI imaging simulation methodology is insufficient in accurately reproducing real-world results and that future work is necessary to more closely align the ARFI imaging models with reality.

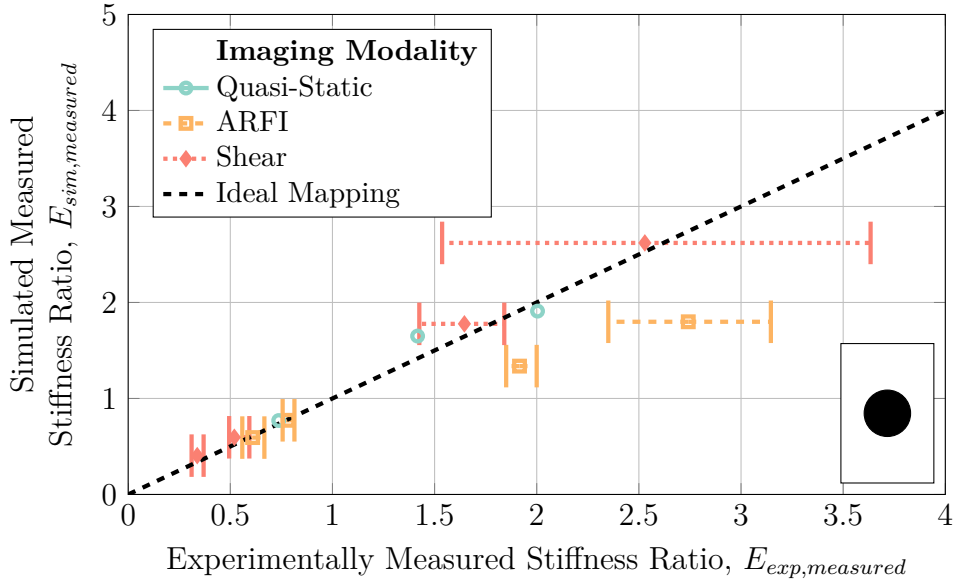


Fig. 6.10: Experimental validation of the simulation results across all three methodologies investigated. The quasi-static ultrasound elastography and shear wave speed quantification simulations most closely matched the results seen experimentally.

6.2 Recommendations and Future Work

The work presented in Chapters 3 – 5 represents a numerical characterization of three different ultrasound elastography imaging modalities: quasi-static ultrasound elastography, acoustic radiation force impulse imaging, and shear wave speed quantification. From the results presented in these chapters the critical parameters relating to detecting both formative and progressive deep tissue injuries across all three detection modalities were investigated. These parameters included device-design specifics such as: frequency; transmit pres-

Appendix B

Source Code

B.1 Quasi-Static Ultrasound Elastography

Listing B.1: Sample code used to simulate b-mode ultrasound images through the convolution of a simulated scattering center distribution with the point spread function of an ultrasound pulse.

```
1 % generate normally distributed noise across the domain
2 rng(domainSeed);
3 backgroundMap = 1 + noiseMagnitude * randn([Ny, Nx]);

5 % transform the background map into the domain -1 -> 1
6 backgroundMap = (backgroundMap - min(min(backgroundMap))) / (
7     max(max(backgroundMap)) - min(min(backgroundMap)));
8 backgroundMap = 2 * backgroundMap - 1;

9 % if a finite-element model of tissue compression is being used
10 ,
11 % compress the background map
12 if model ~= 0
13     % extract the resultant degrees of freedom from the model
14     [x, y, u, v] = extractUV([transducerWidth, depth], size(
15         backgroundMap), model);

16 % generate the domain over which interpolation will occur
17 [xx, yy] = meshgrid(x, y);

18 % interpolate the data to deform it
19 backgroundMap = interp2(xx, yy, backgroundMap, xx - u, yy - v
20 , 'spline', mean(mean(backgroundMap)));
21 end
```

```

21 % use a cosine function to create the point-spread function
22 % shape in the axial direction
23 xpsf = linspace(-windowWidth / 2, windowHeight / 2, 1 *
24     pointsPerWaveLength);
25 ypsf = linspace(0, 4 * wavelength, 2 * pointsPerWaveLength);
26 [xmpsf, ympsf] = meshgrid(xpsf, ypsf);
27 psf = cos(2 * pi * frequency * ympsf / waveSpeed);
28
29 % apply a lateral gaussian "filter" to the signal
30 mu = 0;
31 sigma = windowHeight / 4;
32 gauss = (1 / (sigma * sqrt(2 * pi))) * exp(-(xmpsf - mu) .^ 2 /
33     (2 * sigma ^ 2));
34 psf = psf .* gauss;
35
36 % apply an axial gaussian "filter" to the signal
37 mu = 2 * wavelength;
38 sigma = wavelength * 2;
39 gauss = (1 / (sigma * sqrt(2 * pi))) * exp(-(ympsf - mu) .^ 2 /
40     (2 * sigma ^ 2));
41 gauss = (gauss - min(min(gauss))) / (max(max(gauss)) - min(min(
42     gauss)));
43 psf = psf .* gauss;
44
45 % normalize it to -1 -> 1
46 psf = (psf - min(min(psf)))/(max(max(psf)) - min(min(psf)));
47 psf = 2 * psf - 1;
48
49 % convolve the scattering map with the point spread function
50 bmode = conv2(backgroundMap, psf);
51
52 % crop the image to the appropriate size
53 sz = size(bmode);
54 bmode = bmode(int32(floor((sz(1) - pointDepth) / 2)) : int32(
55     floor((sz(1) - pointDepth) / 2) + pointDepth - 1), int32(
56     floor((sz(2) - numElements) / 2)) : int32(floor((sz(2) -
57         numElements) / 2) + numElements - 1));
58
59 % apply classical ultrasound post-processing
60 % the signal is currently oscillating a high frequency
61 % - extract the envelope of the signal
62 bmode = envelopeDetection(bmode)';
63 % apply log compression to allow to be readily viewed
64 bmode = logCompression(bmode, 3, true);
65
66 % normalize it to 0 -> 1
67 bmode = (bmode - min(min(bmode))) ./ (max(max(bmode)) - min(min(
68     bmode)));

```

Listing B.2: Sample code used to generate displacement maps under quasi-static deformation

```

1  function model = compression(parameters)
2    % import COMSOL features
3    import com.comsol.model.*
4    import com.comsol.model.util.*

5    % create the model
6    model = ModelUtil.create('Model');
7    model.modelPath('compression');
8    model.modelNode.create('mod1');
9    model.geom.create('geom1', 2);
10   model.mesh.create('mesh1', 'geom1');
11   model.physics.create('solid', 'SolidMechanics', 'geom1');
12   model.study.create('std1');
13   model.study('std1').feature.create('stat', 'Stationary');
14   model.study('std1').feature('stat').activate('solid', true);

15   % set parameters in the model
16   model.param.set('modelWidth', sprintf('%f[m]', parameters.
17     domainWidth));
18   model.param.set('modelDepth', sprintf('%f[m]', parameters.
19     domainDepth));
20   model.param.set('appliedStrain', sprintf('%f', parameters.
21     appliedStrain));
22   model.param.set('compression', 'modelDepth*appliedStrain');
23   model.param.set('basalStiffness', sprintf('%f[Pa]', 
24     parameters.basalStiffness));
25   model.param.set('stiffnessRatio', sprintf('%f', parameters.
26     lesionStiffnessRatio));
27   model.param.set('lesionStiffness', 'basalStiffness*
28     stiffnessRatio');
29   model.param.set('lesionExtraStiffness', 'lesionStiffness -
30     basalStiffness');
31   model.param.set('density', sprintf('%f[kg/m^3]', parameters.
32     density));
33   model.param.set('poissonsRatio', sprintf('%f', parameters.
34     poisonsRatio));

35   % deal with the human model case
36   if strcmpi(cell2mat(parameters.caseCategory), 'human') == 1
37     model.param.set('fatStiffness', '80[kPa]');
38     model.param.set('boneStiffness', '18.6[GPa]');
39     model.param.set('fatExtraStiffness', 'fatStiffness -
40       basalStiffness');
41     model.param.set('boneExtraStiffness', 'boneStiffness -
42       basalStiffness');

43   % import our stiffness image
44   model.func.create('im1', 'Image');

```

```

38     model.func('im1').set('filename', sprintf('compression/
stiffnessMap_%03d.png', caseIndex));
40     model.func('im1').importData;
41     model.func('im1').set('xmin', sprintf('%f', (-parameters.
domainWidth / 2)));
42     model.func('im1').set('xmax', sprintf('%f', (parameters.
domainWidth / 2)));
43     model.func('im1').set('ymax', sprintf('%f', parameters.
domainDepth));
44     model.func('im1').set('inplace', 'off');
45     model.func('im1').set('scaling', 'manual');
46     model.func('im1').set('manualexpr', 'r');
47     model.func('im1').set('funcname', 'lesionMap');
48     model.func.duplicate('im2', 'im1');
49     model.func('im2').set('funcname', 'boneMap');
50     model.func('im2').set('manualexpr', 'b');
51     model.func.duplicate('im3', 'im2');
52     model.func('im3').set('funcname', 'fatMap');
53     model.func('im3').set('manualexpr', 'g');
54 else
55     % import our stiffness image
56     model.func.create('im1', 'Image');
57     model.func('im1').set('funcname', 'stiffnessMap');
58     model.func('im1').set('filename', sprintf('compression/
stiffnessMap_%03d.png', caseIndex));
59     model.func('im1').importData;
60     model.func('im1').set('xmin', sprintf('%f', (-parameters.
domainWidth / 2)));
61     model.func('im1').set('xmax', sprintf('%f', (parameters.
domainWidth / 2)));
62     model.func('im1').set('ymax', sprintf('%f', parameters.
domainDepth));
63 end
64
65 % define the model geometry
66 model.geom('geom1').feature.create('r1', 'Rectangle');
67 model.geom('geom1').feature('r1').setIndex('size', '
    domainWidth', 0);
68 model.geom('geom1').feature('r1').setIndex('size', '
    domainDepth', 1);
69 model.geom('geom1').feature('r1').setIndex('size', '
    modelWidth', 0);
70 model.geom('geom1').feature('r1').setIndex('size', '
    modelDepth', 1);
71 model.geom('geom1').feature('r1').setIndex('pos', '-'
    modelWidth/2', 0);
72 model.geom('geom1').run;
73
74 % set the material properties
75 model.physics('solid').feature('lemm1').set(
    'NearlyIncompressible', 1, '1');

```

```

model.physics('solid').feature('lemm1').set('E_mat', 1, 'userdef');

76
% deal with the human model case
78 if strcmpi(cell2mat(parameters.caseCategory), 'human') == 1
    model.physics('solid').feature('lemm1').set('E', 1, 'basalStiffness + (fatMap(x, modelDepth - y) * fatExtraStiffness) + (lesionMap(x, modelDepth - y) * lesionExtraStiffness) + (boneMap(x, modelDepth - y) * boneExtraStiffness)');
else
    model.physics('solid').feature('lemm1').set('E', 1, 'basalStiffness+(stiffnessMap(x,modelDepth-y)*lesionExtraStiffness)');
end

80
82
84 model.physics('solid').feature('lemm1').set('nu_mat', 1, 'userdef');
model.physics('solid').feature('lemm1').set('nu', 1, 'poissonsRatio');
model.physics('solid').feature('lemm1').set('rho_mat', 1, 'userdef');
model.physics('solid').feature('lemm1').set('rho', 1, 'density');

86
88 % set the boundary conditions
90 model.physics('solid').feature.create('fix1', 'Fixed', 1);
model.physics('solid').feature('fix1').selection.set([2]);
model.physics('solid').feature.create('disp1', 'Displacement1', 1);
model.physics('solid').feature('disp1').selection.set([3]);
model.physics('solid').feature('disp1').set('Direction', 2, '1');
model.physics('solid').feature('disp1').set('U0', 2, '-compression');

92
94
96 % create the mesh
98 model.mesh('mesh1').feature.create('ftri1', 'FreeTri');
model.mesh('mesh1').feature('size').set('hauto', '1');
model.mesh('mesh1').run;

100
102 % setup the study and run it
104 model.sol.create('sol1');
model.sol('sol1').study('std1');
model.sol('sol1').feature.create('st1', 'StudyStep');
model.sol('sol1').feature('st1').set('study', 'std1');
model.sol('sol1').feature('st1').set('studystep', 'stat');
model.sol('sol1').feature.create('v1', 'Variables');
model.sol('sol1').feature('v1').set('control', 'stat');
model.sol('sol1').feature.create('s1', 'Stationary');
model.sol('sol1').feature('s1').feature.create('fc1', ' '

```

```

112    || FullyCoupled');
112    model.sol('sol1').feature('s1').feature.remove('fcDef');
113    model.sol('sol1').attach('std1');
114
115    model.sol('sol1').runAll;
116 end

```

Listing B.3: Sample code used to estimate the lateral and axial strain along a given scanline of a pre- and post- compression b-mode image using quasi-static ultrasound elastography.

```

% calculate the number of windows along this scanline
2 M = maxX / deltaAx;

4 % these variables will return the alpha and tau coefficients
% along this scanline
6 alpha = [];
tau = [];

8 % loop through every window along this scanline
10 for m = 1:M
    % calculate the locations of the two windows to start the
    % search from
12    pr1 = m .* deltaAx;
    pr2 = sum(deltaAx ./ alpha);

14    % extract the window in the uncompressed image
16    x1 = linspace(pr1, pr1 + L, numPoints);
    r1 = interp1(1 : length(I1), I1, x1, 'linear', 'extrap');

18    % initialize search variables
20    alphas = maxAlpha:-0.001:1;
    taus = zeros(size(alphas));
    correlations = zeros(size(alphas));

24    % loop through the possible values of alpha
25    for i = 1 : length(alphas)
        % keep track of which scanline gives us the best
        % correlation
        columnCorrelations = [];

28        % loop through the adjacent scanlines
30        for c = (column - columnRadius) : (column + columnRadius)
            % make sure we have a valid scanline
32            if (c < 1) || (c > columns)
                continue;
            end

36            % extract the window in the compressed image
            x2 = linspace(round(pr2), round(pr2) + round(L),
            numPoints);

```

```

38     r2 = interp1(1:length(I2(:, c)), I2(:, c), x2, 'linear',
39                   'extrap');

40     % get the correlation for the two windows
41     columnCorrelations = [columnCorrelations, Correlate(r1,
42 r2)];
43
44     % pick the scanline that had the best correlation for this
45     % alpha
46     c = -columnRadius : column + columnRadius;
47     [correlations(i), mindex] = min(columnCorrelations);
48     taus(i) = c(mindx);
49
50     % employ a-priori smoothing to the data
51     % in case of errant outliers
52     [~, mindex] = min(correlations);
53     if abs(alphas(mindx) - alpha(length(alpha))) > 0.02
54         alpha = [alpha; alpha(length(alpha))];
55         tau = [tau; tau(length(tau))];
56     else
57         alpha = [alpha; alphas(mindx)];
58         tau = [tau; taus(mindx)];
59     end
60 end

```

B.2 Acoustic Radiation Force Impulse Imaging

Listing B.4: Sample code used in conjunction with the K-Wave Toolbox to simulate acoustic radiation force body loads generated by an ultrasonic transducer.

```

% calculate the best grid size for computational efficiency
2 % taking into account Nyquist so that appropriate sampling is
3   used
4 dx = medium.sound_speed / (2 * probingFrequency);
5 dy = dx;
6 Nx = bestFactor(domainDepth / dx + (2 * PML_X_SIZE)) - (2 *
7   PML_X_SIZE);
8 Ny = bestFactor(domainWidth / dy + (2 * PML_Y_SIZE)) - (2 *
9   PML_X_SIZE);
10 dx = domainDepth / Nx;
11 dy = domainWidth / Ny;

12 % make the grid!
13 kGrid = makeGrid(Nx, dx, Ny, dy);
14
15 % create the time array

```

```

14 kGrid.t_array = makeTime(kGrid, medium.sound_speed, [] ,
15     pulseCycles / probingFrequency);
16
17 % beam-form the data
18 % create indices for our elements
19 numActiveElements = Ny;
20 elementIndices = -(numActiveElements - 1) / 2 : (
21     numActiveElements - 1) / 2;
22
23 % calculate time delays for a steered and focussed beam
24 elementWidth = dy;
25 delayTimes = focalDepth / medium.sound_speed * (1 - sqrt(1 + (
26     elementIndices * elementWidth ./ focalDepth) .^ 2)); % [s]
27
28 % convert the delays to be in units of time points
29 delayTimes = delayTimes - min(delayTimes);
30 delayTimes = delayTimes ./ kGrid.dt;
31
32 % use the k-wave toolbox's function "toneBurst" to create the
33 % signal
34 inputSignal = toneBurst(1 / kGrid.dt, probingFrequency,
35     pulseCycles, 'SignalOffset', delayTimes);
36
37 % scale the signal by the source pressure
38 source.p = sourcePressure .* inputSignal;
39
40 % truncate the input signal to the appropriate length
41 source.p = source.p(:, 1:length(kGrid.t_array));
42
43 % make only the nodes along the top boundary apply pressure to
44 % the domain
45 source.p_mask = zeros([Nx, Ny]);
46 source.p_mask(1, 1 : (numActiveElements)) = 1;
47
48 % tell the k-wave toolbox to record the pressure and intensity
49 % for
50 % the entire domain, continuously
51 sensor.mask = ones(Nx, Ny);
52 sensor.record = {'I', 'p'};
53
54 % set up simulation settings
55 inputArgs = {'PlotSim', false, 'PMLInside', false, 'PlotPML',
56     false, 'PMLSize', [PML_X_SIZE, PML_Y_SIZE], 'DataCast', 'single',
57     'DataRecast', true, 'DisplayMask', 'off'};
58
59 % run the simulation
60 sensorData = kspaceFirstOrder2D(kGrid, medium, source, sensor,
61     inputArgs{:});
62
63 % reshape the output data to make sense
64 Ix = reshape(sensorData.Iy, [Nx, Ny, kGrid.Nt]);

```

```

56    Iy = reshape(sensorData.Ix, [Nx, Ny, kGrid.Nt]);
57    P = reshape(sensorData.p, [Nx, Ny, kGrid.Nt]);

58    % calculate body forces
59    alpha = (attenuationCoefficient * 100 * probingFrequency / 1e6)
60        / (20 / log(10));
61    Fx = 2 * alpha .* Ix ./ soundSpeed;
62    Fy = -2 * alpha .* Iy ./ soundSpeed;

```

Listing B.5: Sample code used to simulate time-dependent displacement of viscoelastic soft tissue as a response to acoustic radiation force impulse loads applied to it.

```

1 function model = relaxation(parameters)
2     % import COMSOL features
3     import com.comsol.model.*
4     import com.comsol.model.util.*
5
6     % create the model
7     model = ModelUtil.create('Model');
8     model.modelPath('ARFI');
9     model.name('relaxation.mph');

11    % set parameters in the model
12    model.param.set('domainWidth', sprintf('%f[m]', parameters.
13        domainWidth));
14    model.param.set('domainDepth', sprintf('%f[m]', parameters.
15        domainDepth));
16    model.param.set('focalDepth', sprintf('%f[mm]', parameters.
17        focalDepth));
18    model.param.set('timeStep', sprintf('%f[us]', parameters.
19        timeStep));
20    model.param.set('loadTime', sprintf('%f[us]', parameters.
21        loadTime));
22    model.param.set('listenTime', sprintf('%f[ms]', parameters.
23        listenTime));
24    model.param.set('focalY', 'domainDepth-focalDepth');
25    model.param.set('dFocalY', 'focalY/1[m]');
26    model.param.set('stiffnessRatio', sprintf('%f', parameters.
27        stiffnessRatio));
28    model.param.set('cutoffAmplitude', sprintf('%f', parameters.
29        cutoffAmplitude));

32    % load interpolation files for both geometry
33    % and initial acoustic radiation force
34    model.modelNode.create('mod1');
35    model.func.create('int1', 'Interpolation');
36    model.func.create('int2', 'Interpolation');
37    model.func.create('step1', 'Step');
38    model.func.create('im1', 'Image');
39    model.func('int1').set('funcs', {'Fx', '1'});

```

```

31 model.func('int1').set('source', 'file');
32 model.func('int1').set('filename', 'ARFI/Fx.txt');
33 model.func('int1').set('struct', 'grid');
34 model.func('int1').set('defvars', 'on');
35 model.func('int1').set('extrap', 'value');
36 model.func('int1').set('argunit', 'm');
37 model.func('int1').set('fununit', 'N/(m^3)');
38 model.func('int2').set('funcs', {'Fy' '1'});
39 model.func('int2').set('source', 'file');
40 model.func('int2').set('filename', 'ARFI/Fy.txt');
41 model.func('int2').set('struct', 'grid');
42 model.func('int2').set('defvars', 'on');
43 model.func('int2').set('extrap', 'value');
44 model.func('int2').set('argunit', 'm');
45 model.func('int2').set('fununit', 'N/(m^3)');
46 model.func('step1').set('location', 'loadTime');
47 model.func('step1').set('from', '1');
48 model.func('step1').set('to', '0');
49 model.func('step1').set('smoothactive', false);
50 model.func('im1').set('funcname', 'stiffnessMap');
51 model.func('im1').set('filename', 'ARFI/stiffnessMap.png');
52 model.func('im1').set('xmin', '-domainWidth/2');
53 model.func('im1').set('xmax', 'domainWidth/2');
54 model.func('im1').set('ymax', 'domainDepth');
55 model.func('im1').set('extrap', 'value');

56 % create the geometry
57 model.geom.create('geom1', 2);
58 model.geom('geom1').feature.create('r1', 'Rectangle');
59 model.geom('geom1').feature.create('r2', 'Rectangle');
60 model.geom('geom1').feature('r1').set('pos', {'0' '0'});
61 model.geom('geom1').feature('r1').set('size', {'domainWidth/2
62     ' 'domainDepth'});
63 model.geom('geom1').feature('r2').set('pos', {'domainWidth/2
64     ' '0'});
65 model.geom('geom1').feature('r2').set('size', {'domainWidth/8
66     ' 'domainDepth'});
67 model.geom('geom1').run;

68 % set up material properties
69 model.material.create('mat1');
70 model.material('mat1').propertyGroup.create('KG', 'Bulk
71     modulus and shear modulus');
72 model.material('mat1').propertyGroup('def').set('density', '1060');
73 model.material('mat1').propertyGroup('KG').set('K', '');
74 model.material('mat1').propertyGroup('KG').set('G', '');
75 model.material('mat1').propertyGroup('KG').set('K', 'stiffnessRatio*515.656[kPa]');
76 model.material('mat1').propertyGroup('KG').set('G', 'stiffnessRatio*1032[Pa]');

```

```

75
% set up the physics
% including boundary and ‘‘initial’’ conditions
% fix the bottom of the domain
model.physics.create('solid', 'SolidMechanics', 'geom1');
model.physics('solid').feature.create('fix1', 'Fixed', 1);
model.physics('solid').feature('fix1').selection.set([2 5]);
model.physics('solid').feature('fix1').name('bottom hold');

83
% prevent motion in the vertical direction at the top
% boundary
model.physics('solid').feature.create('disp1', 'Displacement1',
    1);
model.physics('solid').feature('disp1').selection.set([3 6]);
model.physics('solid').feature('disp1').set('Direction', {'0',
    '1'; '0'});
model.physics('solid').feature('disp1').name('top hold');

89
% the ARFI is a body load
model.physics('solid').feature.create('bl1', 'BodyLoad', 2);
model.physics('solid').feature('bl1').selection.set([1]);
model.physics('solid').feature('bl1').set('FperVol', {'Fx(x,y'
    )*step1(t[1/s]); 'Fy(x,y)*step1(t[1/s]); '0'});
model.physics('solid').feature('bl1').set('Ftot', {''; 'Fy(x,
    y)*step1(t[1/s])*10^2'; '0'});
model.physics('solid').feature('bl1').name('ARFI load');

97
% make the model symmetric
model.physics('solid').feature.create('sym1', 'SymmetrySolid',
    1);
model.physics('solid').feature('sym1').selection.set([1]);

101
% use a viscoelastic tissue model
model.physics('solid').feature.create('vmm1', ,
    'ViscoelasticModel', 2);
model.physics('solid').feature('vmm1').selection.all;
model.physics('solid').feature('vmm1').set('K_mat', 'userdef',
    );
model.physics('solid').feature('vmm1').set('K', '(515.656 [
    kPa]) * (1 + (stiffnessMap(x, y) * (stiffnessRatio - 1)))')
    ;
model.physics('solid').feature('vmm1').set('G_mat', 'userdef',
    );
model.physics('solid').feature('vmm1').set('G', '(1032 [Pa])
    * (1 + (stiffnessMap(x, y) * (stiffnessRatio - 1))))';
model.physics('solid').feature('vmm1').set('Branch', {'1';
    '2
    '}; '2'});
model.physics('solid').feature('vmm1').set('Gi', {'(791 [Pa])
    * (1 + (stiffnessMap(x, y) * (stiffnessRatio - 1)))';
    '(66.5 [Pa]) * (1 + (stiffnessMap(x, y) * (stiffnessRatio -
    1)))';
    '(628 [mPa]) * (1 + (stiffnessMap(x, y) * (

```

```

    stiffnessRatio - 1))))}]});
model.physics('solid').feature('vmm1').set('tau', {'2 [s]'; '40 [s]'; '80 [s]'});
model.physics('solid').feature('vmm1').set(
    'NearlyIncompressible', '1');

% create the mesh
model.mesh.create('mesh1', 'geom1');
model.mesh('mesh1').feature.create('ftri1', 'FreeTri');
model.mesh('mesh1').feature.create('map1', 'Map');
model.mesh('mesh1').feature('size').set('hauto', 3);
model.mesh('mesh1').feature('map1').active(false);
model.mesh('mesh1').feature('map1').set('adjustedgdistr',
    true);
model.mesh('mesh1').run;

% set up a probe at the focal point
model.result.table.create('tbl1', 'Table');
model.result.table.create('tbl2', 'Table');
model.probe.create('pdom1', 'DomainPoint');
model.probe('pdom1').model('mod1');
model.coordSystem.create('pml1', 'geom1', 'PML');
model.coordSystem('pml1').selection.set([2]);
model.probe('pdom1').set('coords2', {'0' 'domainDepth-
    focalDepth'});
model.probe('pdom1').feature('ppb1').set('probename', 'focalPointDisplacement');
model.probe('pdom1').feature('ppb1').set('table', 'tbl1');
model.probe('pdom1').feature('ppb1').set('window', 'window1')
    ;
model.result.table('tbl1').name('Probe Table 1');
model.result.table('tbl2').comments('Global Evaluation 1 (t)')
    );

% create a transient study
model.study.create('std1');
model.study('std1').feature.create('time', 'Transient');

% set up the solution parameters
model.sol.create('sol1');
model.sol('sol1').study('std1');
model.sol('sol1').attach('std1');
model.sol('sol1').feature.create('st1', 'StudyStep');
model.sol('sol1').feature.create('v1', 'Variables');
model.sol('sol1').feature.create('t1', 'Time');
model.sol('sol1').feature('t1').feature.create('fc1', 'FullyCoupled');
model.sol('sol1').feature('t1').feature.create('st1', 'StopCondition');
model.sol('sol1').feature('t1').feature.remove('fcDef');
model.sol('sol1').attach('std1');

```

```

151 model.sol('sol1').feature('st1').name('Compile Equations:
    Time Dependent');
model.sol('sol1').feature('st1').set('studystep', 'time');
model.sol('sol1').feature('v1').set('control', 'time');
model.sol('sol1').feature('v1').feature('mod1_u').set(
    'scalemethod', 'manual');
model.sol('sol1').feature('v1').feature('mod1_u').set(
    'scaleval', '1e-2*0.0640312423743285');
model.sol('sol1').feature('t1').set('tlist', 'range(0,
    timeStep,loadTime+listenTime)');
model.sol('sol1').feature('t1').set('fieldselection', 'mod1_u
    ');
model.sol('sol1').feature('t1').set('atolmethod', {'mod1_u' ,
    'global' 'mod1_solid_qXX3' 'global' 'mod1_solid_qXY2' ,
    'global' 'mod1_solid_qXY3' 'global' 'mod1_solid_qXX1' ,
    'global' ...
    'mod1_solid_qXX2' 'global' 'mod1_solid_qYY3' 'global' ,
    'mod1_solid_qYY2' 'global' 'mod1_solid_qYY1' 'global' ,
    'mod1_solid_qXY1' 'global' ...
    'mod1_solid_pw' 'global'});
model.sol('sol1').feature('t1').set('atol', {'mod1_u' '1e-3',
    'mod1_solid_qXX3' '1e-3' 'mod1_solid_qXY2' '1e-3' ,
    'mod1_solid_qXY3' '1e-3' 'mod1_solid_qXX1' '1e-3' ...
    'mod1_solid_qXX2' '1e-3' 'mod1_solid_qYY3' '1e-3' ,
    'mod1_solid_qYY2' '1e-3' 'mod1_solid_qYY1' '1e-3' ,
    'mod1_solid_qXY1' '1e-3' ...
    'mod1_solid_pw' '1e-3'});
model.sol('sol1').feature('t1').set('atoludot', {'mod1_u' '1e
    -3' 'mod1_solid_qXX3' '1e-3' 'mod1_solid_qXY2' '1e-3' ,
    'mod1_solid_qXY3' '1e-3' 'mod1_solid_qXX1' '1e-3' ...
    'mod1_solid_qXX2' '1e-3' 'mod1_solid_qYY3' '1e-3' ,
    'mod1_solid_qYY2' '1e-3' 'mod1_solid_qYY1' '1e-3' ,
    'mod1_solid_qXY1' '1e-3' ...
    'mod1_solid_pw' '1e-3'});
model.sol('sol1').feature('t1').set('atoludotactive', {'mod1_u
    'off' 'mod1_solid_qXX3' 'off' 'mod1_solid_qXY2' ,
    'off' 'mod1_solid_qXY3' 'off' 'mod1_solid_qXX1' 'off' ...
    'mod1_solid_qXX2' 'off' 'mod1_solid_qYY3' 'off' ,
    'mod1_solid_qYY2' 'off' 'mod1_solid_qYY1' 'off' ,
    'mod1_solid_qXY1' 'off' ...
    'mod1_solid_pw' 'off'});
model.sol('sol1').feature('t1').set('timemethod', 'genalpha')
    ;
model.sol('sol1').feature('t1').set('tstepsgenalpha', 'manual
    ');
model.sol('sol1').feature('t1').set('timestepgenalpha', 'timeStep
    ');
model.sol('sol1').feature('t1').set('plot', 'on');
model.sol('sol1').feature('t1').set('plotgroup', 'pg2');
model.sol('sol1').feature('t1').feature('fc1').set('plot', 'on
    ');

```

```

model.sol('sol1').feature('t1').feature('fc1').set('plotgroup
', 'pg2');

177
% add a stop condition to stop the simulation when the tissue
has relaxed
179 model.sol('sol1').feature('t1').feature('st1').set('stopcond',
, 'if(t > 0.003 && mod1.focalPointDisplacement <
cutoffAmplitude, -1, 1)');

181 % create data sets to evaluate later:
182 % * The displacement at the focal point over time
183 % * The displacement along an axial line going through the
focal point
184 % * The displacement along a lateral line going through the
focal point
185 model.result.dataset.create('cpt1', 'CutPoint2D');
186 model.result.dataset.create('cln1', 'CutLine2D');
187 model.result.dataset.create('cln2', 'CutLine2D');
188 model.result.dataset.create('dset2', 'Solution');
189 model.result.dataset('dset2').set('probetag', 'pdom1');
190 model.result.dataset.create('cpt2', 'CutPoint2D');
191 model.result.dataset('cpt2').set('probetag', 'pdom1');
192 model.result.dataset('cpt2').set('data', 'dset2');
193 model.result.numerical.create('pev1', 'EvalPoint');
194 model.result.numerical('pev1').set('probetag', 'ppb1');
195 model.result.numerical.create('gev1', 'EvalGlobal');
196 model.result.numerical('gev1').set('probetag', 'none');
197 model.result.create('pg1', 'PlotGroup1D');
198 model.result('pg1').set('probetag', 'none');
199 model.result('pg1').feature.create('ptgr1', 'PointGraph');
200 model.result.create('pg2', 'PlotGroup2D');
201 model.result('pg2').feature.create('surf1', 'Surface');
202 model.result.create('pg3', 'PlotGroup1D');
203 model.result('pg3').set('probetag', 'none');
204 model.result('pg3').feature.create('lngr1', 'LineGraph');
205 model.result.create('pg4', 'PlotGroup1D');
206 model.result('pg4').set('probetag', 'none');
207 model.result('pg4').feature.create('lngr1', 'LineGraph');
208 model.result.create('pg5', 'PlotGroup1D');
209 model.result('pg5').set('probetag', 'window1');
210 model.result('pg5').feature.create('tblp1', 'Table');
211 model.result('pg5').feature('tblp1').set('probetag', 'ppb1');
212 model.result.dataset('cpt1').name('Focal Point');
213 model.result.dataset('cpt1').set('pointx', '0');
214 model.result.dataset('cpt1').set('pointy', 'dFocalY');
215 model.result.dataset('cln1').name('Lateral Cut');
216 model.result.dataset('cln1').set('genpoints', {'-domainWidth
/2' , 'domainDepth - focalDepth'; 'domainWidth/2' ,
domainDepth - focalDepth'});
217 model.result.dataset('cln2').name('Axial Cut');
model.result.dataset('cln2').set('genpoints', {'0' ,

```

```

    domainDepth'; '0' '0'}));
219 model.result.dataset('dset2').name('Probe Solution 2');
model.result.dataset('cpt2').set('pointy', 'focalY');
221 model.result.numerical('gev1').set('table', 'tbl2');
model.result.numerical('gev1').set('expr', 't');
223 model.result.numerical('gev1').set('unit', 's');
model.result.numerical('gev1').set('descr', 'Time');
225 model.result.numerical('gev1').set('dataseries', 'maximum');
model.result.numerical('pev1').setResult;
227 model.result.numerical('gev1').setResult;
model.result('pg1').name('Focal Point Relaxation');
229 model.result('pg1').set('data', 'cpt1');
model.result('pg1').set(' xlabel', 'Time (ms)');
231 model.result('pg1').set(' ylabel', 'Displacement (m)');
model.result('pg1').set(' xlabelactive', false);
233 model.result('pg1').set(' ylabelactive', false);
model.result('pg1').feature('ptgr1').set('descractive', true)
    ;
235 model.result('pg1').feature('ptgr1').set('descr', 'Displacement');
model.result('pg1').feature('ptgr1').set('titletype', 'manual');
237 model.result('pg1').feature('ptgr1').set('title', 'Focal Point Relaxation');
model.result('pg1').feature('ptgr1').set('xdata', 'expr');
239 model.result('pg1').feature('ptgr1').set('xdataexpr', 't');
model.result('pg1').feature('ptgr1').set('xdataunit', 'ms');
241 model.result('pg1').feature('ptgr1').set('xdatadescr', 'Time');
    );
model.result('pg2').name('Surface Displacement');
243 model.result('pg3').name('Displacement of Axial Focal Cut');
model.result('pg3').set('data', 'cln2');
245 model.result('pg3').set(' xlabel', 'Depth (m) (m)');
model.result('pg3').set(' ylabel', 'Total displacement (m)');
247 model.result('pg3').set(' xlabelactive', false);
model.result('pg3').set(' ylabelactive', false);
249 model.result('pg3').feature('lngr1').set('xdata', 'expr');
model.result('pg3').feature('lngr1').set('xdataexpr', 'domainDepth - y');
251 model.result('pg3').feature('lngr1').set('xdatadescractive', true);
model.result('pg3').feature('lngr1').set('xdatadescr', 'Depth (m)');
253 model.result('pg3').feature('lngr1').set('legend', true);
model.result('pg4').name('Displacement of Lateral Focal Cut')
    ;
255 model.result('pg4').set('data', 'cln1');
model.result('pg4').set(' xlabel', 'x-coordinate (m)');
257 model.result('pg4').set(' ylabel', 'abs(v) (m)');
model.result('pg4').set('legendpos', 'lowerright');
259 model.result('pg4').set(' xlabelactive', false);

```

```

261 model.result('pg4').set('ylabelactive', false);
262 model.result('pg4').feature('lngr1').set('expr', 'abs(v)');
263 model.result('pg4').feature('lngr1').set('descr', 'abs(v)');
264 model.result('pg4').feature('lngr1').set('xdata', 'expr');
265 model.result('pg4').feature('lngr1').set('xdataexpr', 'x');
266 model.result('pg4').feature('lngr1').set('xdatadescr', 'x-
    coordinate');
267 model.result('pg4').feature('lngr1').set('legend', true);
268 model.result('pg5').name('Probe 1D Plot Group 5');
269 model.result('pg5').set(' xlabel', 't');
270 model.result('pg5').set(' ylabel', 'Total displacement, Point
    Probe Expression 1');
271 model.result('pg5').set('windowtitle', 'Probe Plot 1');
272 model.result('pg5').set(' xlabelactive', false);
273 model.result('pg5').set(' ylabelactive', false);
274 model.result('pg5').feature('tblp1').name('Probe Table Graph
    1');

275 % initiate the domain probe we defined earlier
276 model.probe('pdom1').genResult([]);

277 % set the timestepping for the solution
278 model.study('std1').feature('time').set('tlist', 'range(0,
    timeStep, loadTime+listenTime)');
279 model.study('std1').feature('time').set('plot', 'on');
280 model.study('std1').feature('time').set('plotgroup', 'pg2');

281 % run the model
282 model.sol('sol1').runAll;
283
284 end

```

B.3 Shear Wave Speed Quantification

Listing B.6: Sample code used to calculate the speed of a shear wave generated by an ARFI force along a lateral line traversing the focal point of the applied force.

```

1 % extract the displacement along a lateral line traversing the
   focal point
2 % throughout the complete simulation time
3 [x, t, lateralCut] = getLateralFocalCutDisplacement(model);

5 % use the mean value of the displacement through time and
   location
6 % as the isoline value to track
7 targetValue = mean(mean(lateralCut));

9 % loop along the x-coordinates of the dataset
10 points = NaN(length(x), 2);
11 % ignore the first 4 data points which lie within the width of
   the

```

```

% initial radiation force
13  for xi = 5 : length(x)
    % find the point in time where the displacement at the given
    % x-coordinate
15  % crosses the target value previously established
    for ti = 2 : length(t)
        if (lateralCut(ti, xi) < targetValue) && (lateralCut(ti -
17  1, xi) >= targetValue)
            % if the cross-over point was found, store it and
            continue with
            % the next x-coordinate
            points(xi, :) = [t(ti), x(xi)];
21  ti = length(t);
            break;
23  end
24  end
25 end

27 % remove NaNs from the dataset
points = points(~any(isnan(points)), 2, :);

29 % differentiate to get shear velocity
30 % (use a center-weighted moving window average filter first
31 % otherwise the data will become unusable)
32 Ct = diff(smooth(points(:, 2))) ./ diff(smooth(points(:, 1)));
33 x = linspace(min(points(:, 2)), max(points(:, 2)), length(Ct));

```

Appendix C

Experimental Protocols

Each of the protocols detailed here were carried out on a Siemens ACUSON S2000TM portable ultrasound machine with a Siemens 9L4 transducer on a CIRS Elasticity QA Phantom model 049 as shown in Fig. C.1.

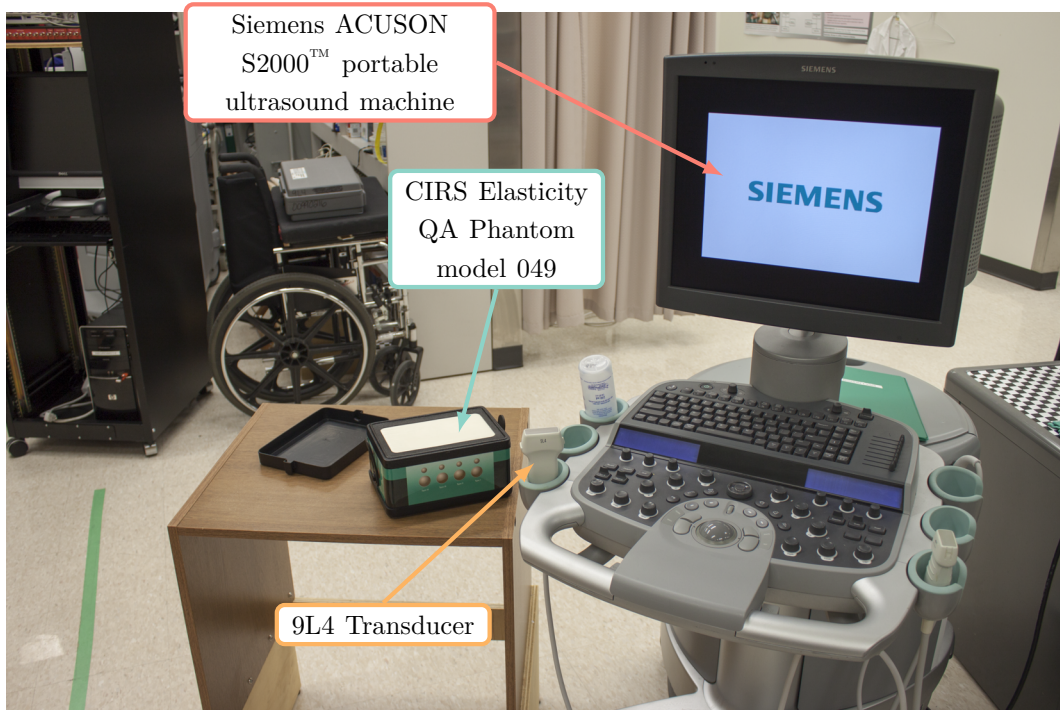


Fig. C.1: Experimental setup showing the ultrasound machine, probe, and phantom model.